Integrated Optimal Dispatch, Restoration and Control for Microgrids

Akshay Kumar Jain

Dissertation submitted to the Faculty of the

Virginia Polytechnic Institute and State University

in partial fulfillment of the requirements for the degree of

Doctor of Philosophy

in

Electrical Engineering

Chen-Ching Liu, Chair

Kevin P. Schneider

Paul K. Ampadu

Steve C. Southward

Vassilis Kekatos

Virgilio A. Centeno

April 19, 2024

Blacksburg, Virginia

Keywords: Microgrid, Controllability, Dynamics Control, Demand Forecasting, Net Metered Loads, Optimal Dispatch, Service Restoration, Stability

Copyright 2024, Akshay Kumar Jain

Integrated Optimal Dispatch, Restoration and Control for Microgrids

Akshay Kumar Jain

(ABSTRACT)

Electric grids across the world are experiencing an ever increasing number of extreme events ranging from extreme weather events to cyberattacks. Such extreme events have the potential to cause widespread power outages and even a blackout. A vast majority of power outages impacting the U.S. electric grid impact the distribution system. There are an estimated five million miles of distribution lines in the US electric grid. A majority of these lines are low-clearance overhead lines making them even more susceptible to damage during extreme events. However, this vital component of the U.S. electric grid remained neglected until recently.

In recent decades, the integration of distributed energy resources (DERs) such as solar photovotaic systems and battery energy storage systems at the grid edge have provided a major opportunity for enhancing the resilience of distribution systems. These DERs can be used to restore power supply when the bulk grid becomes unavailable. However, managing the interactions among different types of DERs has been challenging. Low inertia and significant differences in time constants of operation between conventional generation and inverter based resources (IBRs) are some of these challenges. Widespread deployment of microgrid controller capabilities can be a promising solution to manage these interactions. However, due to interoperability and integration challenges of optimization and dynamics control systems, power conversion systems and communication systems, the adoption of microgrids especially in underserved communities has been slow.

The research presented in this dissertation is a significant step forward in this direction by proposing an approach which integrates optimal dispatch, sequential microgrid restoration

and control algorithms. Potential cyberattack paths are identified by creating a detailed cyber-physical system model for microgrids. A two-tiered intrusion detection system is developed to detect and mitigate cyberattacks within the cyber layer itself. The developed sequential microgrid restoration algorithm coordinates optimal DER dispatch with the operation of legacy devices with no remote control or communication capabilities and net-metered loads with limited communications. By better utilizing the control capabilities of IBRs, reliance on low-latency centralized control algorithms has also been reduced. The developed approach systematically ensures adequate availability of control during dispatch and restoration to maintain microgrid stability. This research can thus pave the way for faster and more cost-effective deployment of microgrids.

Integrated Optimal Dispatch, Restoration and Control for Microgrids

Akshay Kumar Jain

(GENERAL AUDIENCE ABSTRACT)

A U.S. National Academy of Engineering report has described the power grid as the greatest engineering achievement of the 20th century. The power grid is a complex interconnected system consisting of the power transmission system and the distribution system. The power transmission system consists of the power lines seen while driving on the freeways and the large power generating stations consisting of renewable, coal or nuclear power plants. Ensuring the reliable operation of the transmission system has always been a priority.

The distribution system on the other hand consists of pole top transformers seen closer to homes which reduce the voltage to levels safe for electrical appliances. It also consists of the millions of miles of low-clearance overhead distribution lines deployed across the U.S. that provide electricity to every household. This critical part of U.S. electricity infrastructure had remained neglected which is the reason why 90% of power outages impact the distribution system. In recent decades, the integration of renewable energy sources like solar systems and battery storage systems has created an unprecedented opportunity for increasing the resilience of distribution systems against extreme events. These energy sources can provide power supply when the transmission system becomes unavailable. However, ensuring safe and reliable integrated operation of these sources with conventional diesel generators especially while isolated from the transmission system is challenging.

This is where microgrids, which are self-sufficent miniature power grids, can help. Microgrids provide required control, communication and cybsersecurity features necessary for reliable integrated operation of renewable and conventional energy sources. However, the challenges

involved with interoperability of these systems has slowed down the deployment of microgrids especially in underserved communities. This is the research gap addressed in this dissertation. This research provides an approach for integrating the optimization, control, power electronics and cybsersecurity systems. Reliance on expensive low-latency communication systems is reduced by utilizing the emerging capabilities of power electronics devices used for integrating the renewable energy sources with the electric power grid. Voltage control devices already deployed in the distribution systems which do not have remote control or communication capabilities have also been coordinated with energy sources. The research presented in this dissertation is a significant step forward for increasing access to power supply during outages and for reducing the time and cost of deployment of microgrids.

To the guiding light of my faith, the unwavering support of my parents, and the endless love of my wife, whose encouragement fueled my journey through the intricate network of microgrids and power supply reliability, illuminating paths to resilience and sustainability.

Acknowledgments

I would like to express my sincere gratitude to my research advisor Dr. Chen-Ching Liu. Dr. Liu's guidance and support throughout my doctoral education helped me navigate my way through the complex research problems I worked on. Dr. Liu was extremely patient with me and provided invaluable feedback which was essential for the timely and successful completion of this dissertation.

I am also grateful to my Ph.D. committee members, Dr. Kevin P. Schneider, Dr. Paul K. Ampadu, Dr. Steve C. Southward, Dr. Vassilis Kekatos and Dr. Virgilio A. Centeno. I benefited immensely from their mentorship. I thank them for their constructive feedback and for always making time for me out of their busy schedules. I am also grateful to my master's thesis advisor Dr. Robert Broadwater who supported and guided me when I was starting my graduate education at Virginia Tech.

I would like to thank my project team members, Dr. Dushan Boroyevich, Dr. Richard Zhang, Dr. Igor Cvetkovic, and Haris Bin Ashraf from the Center for Power Electronics Studies, and Lung-An Lee, Baza Somda, Nitasha Sahani and Jennifer Appiah-Kubi from the Power and Energy Center. I am grateful to our research group members Chensen Qi, Ruoxi Zhu, Cliff Gyamfi, Akila Herath and Jidapa Chalermkit. Their insightful comments and constructive criticism helped me in further improving my research.

My journey throughout my graduate education could not have been completed without

the support and friendship of fellow graduate students and friends. I would especially like to thank Manish, Shuchismita, Rounak, Sherin, Alok, Nitasha, Sarthak and Tapas whose encouragement and critique were instrumental in helping me sail through my graduate education.

I thank God for my loving family who stood by me through the ups and downs of graduate education. I thank my parents, my brother and my sister-in-law for their unwavering support and my little nephew and niece for bringing a smile on my face during the toughest of times. Last but not the least I would like to thank my wife, Surabhi, for her love and support. Their patience, understanding and their belief in me kept me going and it is their love which helped me reach where I am today.

Finally, I would like to acknowledge the U.S. Department of Energy Office of Electricity, the Pacific Northwest National Laboratory, the Commonwealth Cyber Initiative and the Power and Energy Center of Virginia Tech for their financial support.

Publications and awards from this Dissertation

- **A.K. Jain**, C-C. Liu., A.K. Bharati, K. Schneider, F. Tuffner and D. Ton, "Microgrid Service Restoration Incorporating Unmonitored Automatic Voltage Controllers and Net Metered Loads", *IEEE Transactions on Smart Grid*, 2024.
- **A.K. Jain**, N. Sahani and C-C Liu, "Detection of Falsified Commands on a DER Management System," *IEEE Transactions on Smart Grid*, 2022.
- C.-C. Liu, **A.K. Jain**, D. Boroyevich, I. Cvetkovic, N. Sahani, L.-A. Lee, J. Appiah-Kubi, K.P. Schneider, F.K. Tuffner, and D. Ton, "Microgrid Building Blocks: Concept and Feasibility," *IEEE Open Access Journal of Power and Energy*, vol. 10, pp. 463-476, 2023.
- F.Z. Peng, C-C Liu, Y. Li, **A.K. Jain** and D. Vinnikov, "Envisioning the Future Renewable and Resilient Energy Grids–A Power Grid Revolution Enabled by Renewables, Energy Storage, and Energy Electronics," *IEEE Journal of Emerging and Selected Topics in Industrial Electronics*, 2023.
- **A. K. Jain**, C. -C. Liu, K. P. Schneider, F. K. Tuffner and D. Ton, "Demand Estimation of Net Metered Loads for Microgrid Restoration," *2023 IEEE Power Energy Society Innovative Smart Grid Technologies Conference (ISGT)*, Washington, DC, USA, 2023.
- **Prasad Graduate Fellowship** awarded by Virginia Tech's ECE Department for academic excellence and superior research potential, 2024.
- **Best poster award** at Commonwealth Cyber Initiative's (CCI) Student Researcher Showcase organized by CCI Southwest Virginia, 2022.

- (***to be submitted***) **A.K. Jain**, C-C. Liu., A.K. Bharati, K. Schneider, F. Tuffner and D. Ton, "Ensuring Microgrid Controllability During Dispatch and Restoration", *IEEE Transactions on Power Systems*, 2024.

- (***to be submitted***) **A.K. Jain**, C. Qi, C.-C. Liu, J.P. Pinto, L. Qi and D. Ton, "Quantifying Costs of a Conventional and a Microgrid Building Block Based Microgrid," CIGRE US National Committee 2024 Grid of the Future Symposium.

Contents

List of Figures **xv**

List of Tables **xix**

1 Introduction **1**

1.1 Optimal Dispatch of Microgrids While Ensuring Cyber Security 2

1.2 Optimal Service Restoration of Microgrids 6

1.3 Ensuring Controllability and Stability of Microgrids During Dispatch and Restoration 10

2 Optimal Dispatch of Microgrids While Ensuring Cyber Security **14**

2.1 Cyber-Physical System Model for DERMS 15

2.1.1 Cyber System Model 15

2.1.2 Physical System Model 16

2.1.3 Co-simulation for DERMS CPS Model 21

2.2 Falsification of Control Commands 22

2.2.1 Attack Path 1: Cyber Layer 23

2.2.2 Attack Path 2: DERMS Centralized Controller 23

2.3 Two-Tiered Intrusion Detection System 26

2.3.1 Tier 1: Centralized Detection 27

2.3.2 Tier 2: De-centralized Detection 29

2.4 Case Study 32

2.4.1 DERMS Centralized Controller 33

2.4.2 Cyber-attack Models and Mitigation Results on IEEE 13-bus Feeder . 34

2.4.3 Cyber-attack Models and Mitigation Results on IEEE 123-bus Feeder: 39

3 Optimal Service Restoration of Microgrids 42

3.1 Optimal Control Incorporating Unmonitored Automatic Voltage Controllers 43

3.1.1 Determining Optimal States 45

3.1.2 Line Drop Compensation 47

3.1.3 Linearizing AVR Load Center Voltage Estimation 48

3.1.4 Constraints to Influence AVRs to Move to Optimal Tap Positions . . 49

3.1.5 Automating Constraint Selection 50

3.1.6 Optimal Control of Automatic Capacitor Banks 51

3.2 NM Load Model 51

3.2.1 CLPU Phenomenon and NM loads 52

3.2.2 Microgrid Restoration Stages with NM Loads 53

3.2.3 Disaggregation of NM Time Series 54

3.2.4 Generalized Time Dependent NM Load Demand Model 57

3.3 Sequential Microgrid Restoration Algorithm 58

3.4 Case Study 67

3.4.1 Impact of Voltage Regulation Devices' States on Voltages 68

3.4.2 Quasi Static Time Series Validations using OpenDSS 69

3.4.3 Sequential Microgrid Restoration Results 71

3.4.4 Algorithmic Complexity 73

4 Ensuring Controllability and Stability of Microgrids During Dispatch and Restoration 75

4.1 Stability and Controllability of Switched Linear Systems 77

4.1.1 Stability of Switched Linear Systems 78

4.1.2 Controllability of Switched Linear Systems 81

4.2 Determining Operating Point From Optimal Dispatch 83

4.2.1 Power Flow Equations 84

4.2.2 Estimating Operating Point From Optimal Dispatch 87

4.3 State Space Modeling 90

4.3.1 Case 1: SG with Both IBRs in GFM Mode 91

4.3.2 Case 2: SG with IBR_j Operating in the GFM Mode and IBR_k Operating in GFL Mode . . . 94

4.3.3 Case 3: SG with IBR_j Operating in the GFL Mode and IBR_k Operating in GFM Mode . . . 99

4.3.4 Case 4: SG with Both IBR_j and IBR_k Operating in GFL Mode . . . 100

4.4 Case Study . . . 101

4.4.1 Validation of Proposed GFM and GFL IBR Models . . . 101

4.4.2 Validation of Proposed approach on Detailed Microgrid Model . . . 103

5 Conclusions and Future Work **111**

5.1 Conclusions . . . 111

5.2 Future Work . . . 113

Bibliography **114**

Appendices **129**

Appendix A First Appendix **130**

A.1 Proving Convexity of the OPF Formulation Proposed in Chapter 2 . . . 130

A.2 Unity Correlation Coefficient and Linearity . . . 133

A.3 Additional Constraints Used in Section 3.3 . . . 135

A.4 IEEE Article Reuse Policy . . . 138

List of Figures

1.1 Proposed approach for integration of optimal dispatch, service restoration, dynamics control and cybersecurity algorithms 3

2.1 Cyber-physical model and attack paths 15

2.2 Two-stage cyberattack using DERMS controller 25

2.3 Methodology of the proposed two-tiered IDS 26

2.4 Tier 1: Cyber layer based centralized intrusion detection system 27

2.5 DERMS centralized controller maintains voltages within thresholds and minimizes DPV curtailment 33

2.6 Nodal voltages and voltage regulating equipment states in cyber layer-based falsified control command cyberattack and detection 36

2.7 Detection of replay attacks (RA) by *Timestamp based MAC-IDS* 37

2.8 Nodal voltages and voltage regulating equipment states with the 2-stage falsified control command cyberattack and detection 38

2.9 All load bus voltages after 2-stage cyberattack (top); and AVR taps positions (bottom) 39

2.10 All load bus voltages after 2-stage cyberattack with 2 larger DPV and 100% rooftop DPV (left); two larger DPV and no rooftop DPV (right) 40

2.11 All load bus voltages after 2-stage cyberattack mitigation (top); and differences between MLR estimated setpoints and actual set points (bottom) . . . 41

3.1 Typical microgrid topology with unmonitored automatic voltage controllers, NM loads and remotely controllable DERs and switches. 44

3.2 Line drop compensation in AVRs 47

3.3 [a] NM demand stages during restoration; [b] demand increase due to CLPU; [c] proposed NM load demand model (CLPU + NM demand stages) 49

3.4 Flow chart summarizing the approach for creating the proposed NM demand model. 52

3.5 Flow chart summarizing the proposed MILP based sequential microgrid restoration algorithm. 61

3.6 Extended IEEE 123-node test feeder in OpenDSS used as a microgrid 67

3.7 Histogram of nodal voltages in IEEE 123-node system when AVR taps (a) are considered, (b) not considered, while optimally dispatching DERs 68

3.8 Tap estimation results with limited measurements using MILP formulation proposed in section 3.3 69

3.9 Taps controlled at neutral position (tap=0) throughout the QSTS simulation using the method proposed in section 3.1 70

3.10 [a] Restoration sequence of load sections and their demand during each microgrid restoration interval; [b] Switches energized to restore all load sections of the microgrid 71

3.11 Comparison of actual demand with demand forecasts obtained using the approach proposed in section 3.2, disaggregation approach in [1], and only NM time series data. 72

3.12 AVR tap positions during microgrid restoration with and without the proposed optimal control approach 72

3.13 All nodal voltages during microgrid restoration [a] with, and [b] without the proposed optimal control approach 73

4.1 Reduced IEEE 13 node model with a SG and two IBRs 84

4.2 GFM Control Mode of an IBR 91

4.3 SG model for slow frequency dynamics studies 93

4.4 GFL control mode of an IBR 94

4.5 Flow chart summarizing proposed approach for ensuring microgrid stability and controllability 101

4.6 2-bus system for validation of proposed GFL and GFM models 101

4.7 Simulation to validate proposed GFM and GFL models 103

4.8 Detailed Simulink simulation results show low IBR scenario is stable. 107

4.9 Detailed Simulink simulation results show high IBR scenario is stable. 107

4.10 Detailed Simulink simulation results show transtion from low to high IBR scenario is unstable. 108

4.11 Detailed Simulink simulation results show transtion from low to high IBR scenario can be stabilized using state feedback control signals if it is controllable. 109

4.12 Detailed Simulink simulation results show stable transtion from low to high IBR scenario after switching control mode of IBR_k to GFL. 110

A.1 Same maximum OpenDSS voltages observed using Matlab and PYOMO . . 133

A.2 Comparison of solar generation estimates obtained using proposed disaggregation based approach with actual solar generation. 135

List of Tables

2.1 Impact comparison of the 2-stage cyberattack on different DPV scenarios for 123-bus system 40

3.1 Computational Time Complexity of the Proposed Algorithm 74

4.1 Optimal set points and terminal measurements for 20% simulation 104

4.2 Optimal set points for previous and new dispatches 106

Chapter 1

Introduction

Microgrids are essential building blocks for creating resilient distribution systems against extreme events such as weather events and cyberattacks [2]. A microgrid can be deployed to sustain electricity service when the hosting bulk power grid (to which the microgrid is connected) becomes unavailable. Electric energy in a microgrid is often produced by Distributed Energy Resources (DERs), including renewable energy and energy storage facilities as well as traditional synchronous generators of ratings up to a few MWs. Critical microgrid functions inclue the ability to operate in a stable manner while being isolated from the bulk grid, and the ability to optimally dispatch and restore demand after an outage using locally available distributed energy resources (DERs) [3]. Since communication is often required to acquire measurements from DERs and send control commands from the centralized controller to the DERs, cybersecurity of communication channels must also be ensured. Maintaining stability and controllability of microgrids in the presence of different types of DERs including inverter-based resources (IBRs) is essential as the level of penetration of DERs increases.

Research on microgrids however, tends to be focused on different areas that may be integrated to create a microgrid. There is a lack of integration between optimal dispatch, dynamics

control and cybersecurity algorithms. To bridge this research gap, an approach which tries to ensure optimal and stable operation of microgrids under grid-connected as well as islanded operating conditions is proposed in this dissertation. As shown in Fig. 1.1, in this approach the cybersecurity of all measurement and control command data packets is ensured by passing them through cybersecurity screens. If an outage is detected and the microgrid is not in the islanded mode, an optimal sequential microgrid restoration plan is created. This restoration plan is implemented using an accurate three-phase unbalanced optimal power flow algorithm. The same algorithm is also used for optimally dispatching DERs during grid-connected and islanded modes of operation. This approach also ensures that the stability of the microgrid is maintained whenever a new optimal dispatch is applied by determining the correct control mode, grid forming (GFM) or grid following (GFL), of IBRs. The proposed research not only addresses the integration challenges, but also makes important research contributions in each of these areas. The research presented in this dissertation aims at reducing the time and cost of deployment of microgrids to enable their widespread adoption. In comparison with the state-of-the-art, the novel research contributions of this research are in the areas of cybersecure optimal dispatch, sequential microgrid restoration and stable microgrid operation during planned transitions.

1.1 Optimal Dispatch of Microgrids While Ensuring Cyber Security

Centralized DER management systems (DERMS) have been proposed to effectively mitigate voltage violations and ensure fairness of curtailment among all inverters [4]. A centralized DERMS controller at the distribution substation receives inputs from advanced metering infrastructure (AMI), such as advanced inverters and smart meters, and generates optimal

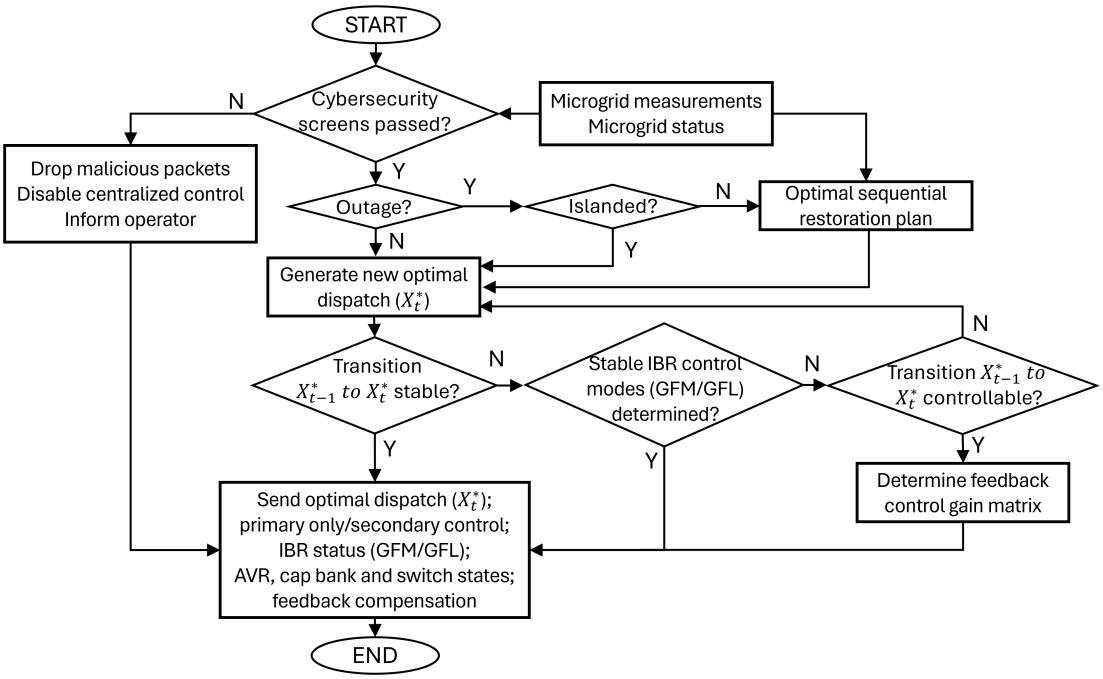

Figure 1.1: Proposed approach for integration of optimal dispatch, service restoration, dynamics control and cybersecurity algorithms

real and reactive power dispatch settings for each inverter based DER [5]. However, their dependence on communication channels makes them vulnerable to cyberattacks.

Teymouri et al. propose cyberattack models on voltage sensors and inverter based DERs to cause increased losses and power curtailment [6]. Johnson et al. report cyberattacks on AIFs [7]. However, these attacks are low severity and localized in nature. Isozaki et al. proposed cyberattacks on a centralized voltage control scheme using falsified measurements sent to AVR controllers from sectionalizing devices [8]. However, these types of attacks may not be realized as most AVRs use localized line drop compensation (LDC) control [9] with no remote-control capabilities. Furthermore, the presence of other voltage regulating equipment such as advanced inverters and capacitor banks have not been considered.

Cyberattacks on centralized distribution automation systems and their detection have been considered recently [10] [11]; however, research on cyberattacks targeting centralized DERMS

is in an early stage. Denial-of-Service (DoS) and false data injection (FDI) attacks on a DERMS controller are proposed in [12] and [13]. However, the DERMS controllers are limited to BESS and do not include power flow constraints potentially leading to infeasible results. Although these papers consider a communication layer, the cyberattack detection and mitigation is typically performed at the physical layer, thus the cyberattack will impact the power system before it can be mitigated.

Machine Learning to detect cyberattacks has been proposed recently [14]. Data-driven methods such as support vector machines and artificial neural networks are compared in terms of their ability to detect cyberattacks [15]. Detection methods based on attack signatures to detect man-in-the-middle (MITM), DoS and Spoofing cyberattacks have been proposed [16], [17]. Along with the detection of DoS or malicious data packets, there is a need to detect FDI attacks that may go undetected at the cyber layer and mitigate them to prevent impact propagation onto the physical layer. There is also limited work which analyzes stealthy MITM attacks such as data packet modification or replay attack in cyber layer.

Thus a comprehensive cyber-physical system (CPS) model for DERMS is required, consisting of a physical layer and a cyber layer. The proposed CPS model is used to determine the cyberattack paths an adversary may use to impact voltage regulating equipment and damage customer devices. Furthermore, a cyber layer-based intrusion detection system (IDS) capable of detecting and mitigating FDI, data packet modification, and replay cyberattacks in the cyber layer itself is needed.

In chapter 2, the cyberattack models are proposed which an adversary can use to falsify control commands on a DERMS system. These attacks involve control command falsification and modifications to the DERMS algorithm which can damage IT equipment, trip inverters, and trigger undesirable operations of AVRs and capacitor banks. Note that software modification is a key component of the cyberattacks against the Ukrainian power grid [18]. A

detailed cyber-physical system (CPS) model for DERMS is presented in this dissertation to evaluate the severity of attack models and determine mitigation strategies. A CPS model is essential as a physical model alone cannot be used to determine the cyberattack paths or assess the feasibility of defense models such as their vulnerability to replay attacks [19]. The presented DERMS CPS model can be scaled by integrating it with co-simulation platforms such as HELICS [20] and simulating federated DER and DERMS controllers.

In chapter 2, centralized intrusion detection techniques within the cyber layer using time stamps and message authentication code (MAC) [21] are proposed. The proposed techniques do not depend on physical properties of power systems. Thus, these techniques can identify a wide array of attacks targeting system voltage, frequency, or other measurements. The efficacy of the proposed technique is contrasted against physical layer-based detection techniques which compare received measurements with their expected values, such as those used in [13]. Physical layer-based detection techniques are limited in scope and can only detect cyberattacks targeting specific measurements. Along with centralized intrusion detection techniques, inverter-based decentralized intrusion detection techniques using multivariate linear regression [22] are also proposed in this chapter. A de-centralized approach is needed to mitigate those cyberattacks where the DERMS controller's software has been modified to make malicious command data packets appear to be legitimate. Thus, the contributions of this chapter are twofold:

- A scalable cyber-physical system model is proposed to quantify the severity of falsified control command cyberattacks targeting DERMS controllers. This model includes a detailed three-phase unbalanced optimal power flow formulation.

- Cyber layer based centralized, and inverter based decentralized intrusion detection techniques are also proposed. These techniques can detect and mitigate the cyberat-

tacks before they impact the physical power systems layer.

1.2 Optimal Service Restoration of Microgrids

Current microgrid restoration and dispatch algorithms do not accurately incorporate the impact of key microgrid components such as automatic voltage regulators (AVRs) and capacitor banks [23],[24]. Non dispatchable behind-the-meter (BTM) resources such as net metered (NM) loads which have a load and a photovoltaic (PV) system are also not adequately studied [25]. Uncontrolled operation of voltage regulation devices combined with a demand generation imbalance due to inaccurate demand forecasts of NM loads can lead to frequency instability in islanded microgrids [26].

Microgrids are typically integrated with radial distribution feeders [27] and can have AVRs and capacitor banks. These devices can be automatic as they have a controller which measures local parameters such as their terminal voltage to determine the appropriate tap position or state [28]. For cost-effectiveness these devices are typically unmonitored as their states can neither be communicated nor controlled through the utility control center [29]. DERs can cause significant increases in state changes of AVRs [30],[31] and capacitor banks [32] which impacts the microgrid's voltage profile. Voltage collapse in distribution systems has been observed in [33] due to differences in time scales of operation of inverter based resources (IBRs) and AVRs. Lack of coordination between the various voltage controllers and IBRs in a microgrid can result in large voltage oscillations [26]. It is thus essential to coordinate centrally dispatchable DERs with unmonitored automatic voltage controllers to maintain voltage stability.

The discrete behavior of voltage regulation devices leads to non-linearities and these devices are often not considered in microgrid service restoration and dispatch algorithms [24]. Even

when these devices are included in microgrid restoration and dispatch algorithms, their taps are either assumed to be stationary during restoration [34] or are considered as decision variables [35]. This assumes remote control capabilities are present in these devices. This, however, is not true and most AVRs and capacitor banks deployed in rural and semi-urban feeders rely on automatic controllers [28],[36]. Upgrading their controllers with intelligent electronic devices can be costly [37]. The high cost can slow the deployment of microgrids, especially in rural and disadvantaged communities. It is thus essential to accurately incorporate the behavior of automatic voltage controllers within microgrid dispatch and restoration optimization algorithms.

Frequency instability during sequential microgrid restoration can arise due to demand-generation imbalance [38]. Thus, frequency stability metrics and primary frequency control were incorporated in a multi-period microgrid dispatch model in [39]. A more complete model considering the impact of different IBR's frequency support control schemes such as droop and virtual synchronous machine is provided in [40]. However, this nonlinear formulation is difficult to solve and, therefore, a linearized and discretized frequency response model is proposed in [41]. However, as the considered time horizon increases, the computational complexity of this model increases significantly necessitating the use of generalized Benders decomposition (BD) algorithm and multi-cut accelerating techniques to improve the performance. To reduce the computational burden, data based approaches using machine learning have been proposed [42], however availability of training data for contingencies in microgrids is very limited.

Due to these challenges of integrating frequency response constraints within optimization based dispatch and restoration algorithms, simulation based methods have been proposed [38], [43]. In these two-level methods, transient simulations are used to obtain the maximum frequency deviation due to the obtained optimal restoration solution. By iterating between

the transient simulations and the optimal solution, the maximum allowable load step for the next restoration interval is determined. These methods can improve frequency response of the microgrid provided detailed microgrid dynamic models are known, including DER parameters such as cutoff frequencies of IBR filters. This would be especially difficult as existing distribution systems with already installed DERs are converted to microgrids. The other major issue is that the load demand is assumed to be known during each restoration interval. The maximum allowable load step to limit frequency deviations is based on these load demands. It will be shown in this study that the demand of NM loads during microgrid restoration is significantly different from their pre-outage demand. Thus, the two-level simulation-assisted restoration algorithms can be further improved by integrating the proposed NM load demand model.

The presence of more than one million NM loads in California alone [44] suggests that high penetration of NM loads can be expected in distribution systems and microgrids. The BTM PV system of these NM loads is not dispatchable as this would require an extensive communication network and control capabilities [45]. For NM loads only the net demand (actual demand - generation) may be available through advanced metering infrastructure (AMI) [46]. However, even with AMI, the demand of NM loads during microgrid service restoration cannot be forecasted in accordance with the IEEE 1547-2018 standard [47].

NM loads typically exhibit the Cold Load Pickup (CLPU) phenomenon during restoration. CLPU refers to the increase in load demand observed after an outage due to the loss of diversity of thermostatically controlled loads (TCLs) [48]. Since NM loads consist of a PV system and a typical residential or commercial load, most NM loads can be expected to have TCL loads which will exhibit CLPU phenomenon after an outage. CLPU of NM loads will significantly increase the load demand during microgrid restoration. For instance, if an outage occurs during the daytime, a net injection from NM loads may be expected due to

excess solar generation. However, due to CLPU the NM load may end up consuming power. Demand-generation imbalance may arise if CLPU of NM loads is not considered, resulting in frequency instability. The behavior of TCL loads is typically characterized using the delayed exponential model (DEM) [49]. More recently it has been shown that the DEM model is not accurate for shorter outage durations [50]. However, a generalized model incorporating both CLPU and NM load behavior during restoration has not been reported in the literature.

In chapter 3, it is shown that modeling both CLPU and NM load behavior during restoration requires the disaggregation of NM time series of NM loads into actual demand and generation time series. Disaggregation has been studied recently for demand response applications but not for microgrid restoration [51]. It has been used to estimate the rating of PV systems, which however is known to utilities through interconnection applications [52]. In [1] solar generation and actual demand for each NM load are forecasted separately, by representing them as linear functions of representative feature vectors. The feature vector for solar generation is the average profile of several randomly located NM loads deployed with separate solar generation measurement meters. The actual demand feature vector is the average of the demand profiles of the loads without solar generation. However, no justifications are provided for using linear functions. Accuracy is not ensured, as randomly placed solar generation measurement meters are used. Also, since load demands can vary widely amongst NM loads, separate load forecasts are prone to forecasting errors. The contributions of this chapter which address these issues are:

- A novel optimal DER dispatch method is proposed which creates such voltages and line flows at the point of common coupling (PCC) of voltage regulation devices, commanding their unmonitored automatic voltage controllers to move to their respective optimal states.

- A generalized time dependent demand model is proposed for NM loads which incorporates both CLPU and their behavior during microgrid restoration. The model uses the correlation in NM time series of NM loads to obtain the disaggregated actual demand and generation time series.

- A mixed integer linear programming (MILP) based approach is proposed to accurately control the time dependent behavior of voltage regulation devices and NM loads during each restoration time interval by linearizing the logic propositions. The proposed approach can be integrated with existing MILP based microgrid restoration algorithms [53].

1.3 Ensuring Controllability and Stability of Microgrids During Dispatch and Restoration

The DERs must be dispatched optimally during microgrid restoration as well as during islanded operation after restoration. A major challenge however is that when a new optimal dispatch is applied to the primary controllers of the DERs in the microgrid, either during sequential restoration or during post-restoration islanded state, the microgrid experiences transients. The integration of inverter-based resources (IBRs), such as photovoltaic (PV) or battery energy storage systems (BESS), can further exacerbate this problem. IBRs such as BESS can reach rated power in less than one second [54]. Thus unlike synchronous generators (SGs) which have slower ramp rates and thus limit the maximum changes in generation between successive dispatches, IBRs do not have such constraints. IBRs can be made to operate slower but then they will lead to sub-optimal operation. An approach is thus needed to ensure that the microgrid will remain stable and controllable after transitioning

to the next optimal dispatch in the presence of IBRs and SGs.

The stability and controllability of the microgrid can be studied by modeling it as a state space model [55]. Creating an accurate state space model while considering the power flow equations and interactions among DERs is a challenging task. For creating a state space model, the non-linear power system must be linearized around an operating point. This linearized state space model can accurately describe the microgrid behavior for small disturbances around the operating point. However, when a new optimal dispatch is applied it moves the microgrid to a new operating point which may not be close to the operating point of the previous dispatch. Thus, a new state space model must be designed for the new operating point to determine stability of the new dispatch.

There exist several challenges. It is possible that the model is unstable with the new optimal dispatch. If it is controllable then state feedback control can be designed to stabilize it. However, this would require measurement of states, observer design for unmeasurable states and then sending the feedback compensation to the control inputs. The communication latency involved in this process can also impact system stability. If the system is uncontrollable then a new sub-optimal dispatch can be generated by limiting IBR generation to small changes from their previous dispatch. This new sub-optimal dispatch may be infeasible and even if it can maintain demand-generation balance, the state space model for this dispatch is not guaranteed to be stable.

IBRs can typically operate in grid following (GFL) and grid forming (GFM) modes [56]. Significant research has been conducted on creating primary IBR controllers capable of seamlessly transitioning between these modes [57], [58]. Thus, another unexplored option to maintain microgrid stability without having to change the optimal dispatch would be to switch the control mode of one or more IBRs in the microgrid which changes the state space model.

Another challenge is that the switched system can be unstable as the microgrid transitions from the state space model from the previous dispatch to that of the new dispatch. It has been shown that even if individual linearized models are stable, the switched system can have divergent trajectories [59],[60]. Thus the stability of such switched systems not only depends on the individual models but also on the switching signals. A closely related example of switched systems is power electronics converters where a stabilizing switching signal, such as the pulse width modulation (PWM) signal, is designed to switch between several state space models to keep the converter stable and controllable [61].

However, switching in microgrids can take place in different ways and the development of a stabilizing switching signal that can handle various configurations is a difficult problem. This is because the microgrid switches to a new control mode only when a new dispatch becomes available which happens after few seconds to minutes. Thus switching is much slower than the time scale of power electronics converters where switching can happen within microseconds. Then, the microgrid does not keep switching between the same set of state space models because the optimal dispatch can be different every time. In switched linear systems theory such systems are said to have arbitrary switching [62]. An approach is thus needed to analyze the stability of such switched systems under different switching actions. If these systems are found to be unstable, the controllability of these systems must also be analyzed so that a control input can be designed to stabilize the microgrid while transitioning to the new optimal dispatch. Chapter 4 presents a novel approach designed to address these research challenges. The main contributions of this chapter are:

- An approach to determining the correct control mode of IBRs while stability and controllability of the microgrid is ensured.

- Since the controller has to determine the stability and controllability of the switched

microgrid system in real time, a method is created to generate accurate state space models which capture the dynamics of interest while reducing the number of states.

- An approach to determine the operating point from the optimal dispatch is created.
- These state space models also ensure that the state vector does not change when IBR mode is changed from GFM to GFL or vice versa. This allows application of switched linear systems stability concepts.
- A computationally efficient approach is used for evaluating the controllability of the switched microgrid system.

Chapter 2

Optimal Dispatch of Microgrids While Ensuring Cyber Security

As described in the introduction section 1.1, optimal dispatch algorithms are essential for reliable operation of microgrids. However, the use of communication channels makes them susceptible to cyberattacks. It is thus essential to determine the potential attack paths and create an intrusion detection algorithm which can mitigate these attacks in the cyber layer itself and protect the physical microgrid from any severe impacts. The remaining of this chapter is organized as follows: Section 2.1 describes the proposed DERMS cyber-physical system. Falsified control command cyberattack paths are described in section 2,2. Proposed defense models to detect and mitigate these cyberattacks are presented in section 2.3. Case studies on IEEE test feeders are presented in section 2.4.

© 2022 IEEE. Reprinted, with permission, from A. K. Jain, N. Sahani and C. -C. Liu, "Detection of Falsified Commands on a DER Management System," in IEEE Transactions on Smart Grid, vol. 13, no. 2, pp. 1322-1334, March 2022.

2.1 Cyber-Physical System Model for DERMS

The objective of this chapter is to show how an adversary can make modifications to the control command data packets or the DERMS algorithm to cause damages. In this section, a CPS model for DERMS is presented, which is essential to determine the cyberattack paths and detection techniques. As shown in Fig. 2.1, the CPS model has a cyber layer and a physical layer. The physical layer includes optimal power flow (OPF) based DERMS controller for DPV and BESS which interacts with the 3-phase unbalanced power flow model of a distribution feeder. Data between the feeder model and the DERMS controller is exchanged through a cyber layer, based on a queuing model [19].

2.1.1 Cyber System Model

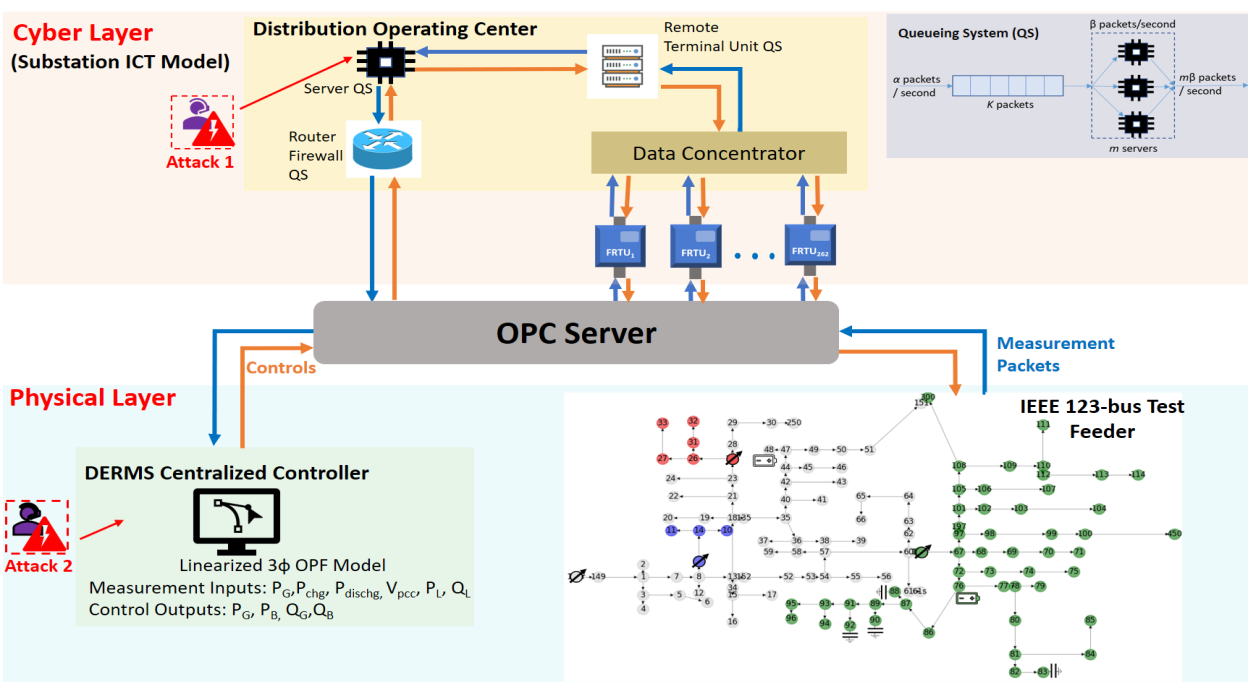

Figure 2.1: Cyber-physical model and attack paths

The cyber layer represents the information and communications technology (ICT) or the

Supervisory Control And Data Acquisition (SCADA) at the substations. The cyber layer consists of the ICT path through which the physical layer and the DERMS controller communicate. Each communication capable inverter will communicate via the Object linking and embedding for Process Control (OPC) standards conforming Feeder Remote Terminal Units (FRTUs). FRTUs are pole-top field devices which send measurement packets to the cyber layer through the OPC server. These devices are mimicked in the cyber layer as shown in Fig. 2.1, where data packets are mapped to their corresponding FRTUs. In the cyber layer, data packets go from each FRTU through the $D/D/m/K$ queuing model as the fundamental communication mechanism. Each device consists of m servers with the capability to process β packets per second [19]. The data packets arrival time and service time are deterministic (D) in nature. The queue has a capacity to hold K packets and packets arrive at the queue at a rate of α packets per second as shown in Fig. 2.1. If more than $m\beta$ packets arrive they must wait in the queue for W seconds. If packets arrive after the queue is full, they will be dropped. A packet is processed in G seconds and reaches the destination in $W + G$ seconds.

The data packets received from the multiple FRTUs move to the cyber layer distribution operating center's remote terminal unit (RTU) via a data concentrator. The RTU then sends the packets through a first-in-first-out (FIFO) queue to the servers. The measurement data packets are then sent to the controller through a firewall to check for discrepancies. The controller after deciding on the required control action sends the control command packet back to the physical system for it to be implemented via the cyber layer queueing system.

2.1.2 Physical System Model

The physical layer consists of the feeder model and the DERMS controller. In Fig. 2.1, IEEE 123-bus feeder is presented as an example for the feeder model in the physical layer. The

distribution feeder has been modeled using an open-source distribution system simulation platform OpenDSS through OpenDSSDirect.py [63]. This 3-phase unbalanced non-linear power flow-based model has detailed models for loads, DPV systems, BESS, AVRs with LDCs, capacitor banks and their localized controllers, and other power delivery and conversion equipment.

In this chapter, scalars are represented by lower case letters x and vectors are represented using boldface lower case letters $\boldsymbol{x}$. Sets are represented by uppercase letters X and matrices are represented using boldface uppercase letters $\boldsymbol{X}$. The parameters and variables are:

Parameters: $\boldsymbol{s}_G$: Vector of kVA ratings of all n_G DPV inverters; $\boldsymbol{s}_B$: Vector of kVA ratings of all n_B BESS inverters. $\boldsymbol{q}_{Gmax}(\boldsymbol{q}_{Gmin})$: Vector of maximum (minimum) reactive power ratings of all n_G DPV inverters. $\boldsymbol{q}_{Bmax}(\boldsymbol{q}_{Bmin})$: Vector of maximum (minimum) reactive power ratings of all n_B BESS inverters. $\boldsymbol{p}^t_{Gmax}(\boldsymbol{p}^t_{Gmin})$: Vector of maximum (minimum) generation limits of DPV inverters at any $t = \{1, ..., t_{sim}\}$, where t_{sim} is the total simulated time points. $\boldsymbol{p}^t_{Gmax}$ is based on solar irradiance at time t and $\boldsymbol{p}^t_{Gmin} = \boldsymbol{0}$. $\boldsymbol{p}^{chg,t}_B(\boldsymbol{p}^{dischg,t}_B)$: Vector of maximum charging (discharging) rates for BESS based on state of charge and minimum reserve constraints. $\boldsymbol{q}^t_C$: Vector of reactive power injections from capacitor banks, if present, 0 otherwise. $\boldsymbol{p}^t_L(\boldsymbol{q}^t_L)$: vector of real (reactive) power demands. $\boldsymbol{a}^t$: Vector of AVR tap positions at any $t = \{1, ..., t_{sim}\}$. Each element of $\boldsymbol{a}$ is $1 \pm 0.00625*$tap position of nearest upstream AVR, if present, 1 otherwise. Without loss of generality, all AVR's and substation LTC are assumed to have ± 16 taps to provide $\pm 10\%$ voltage regulation; a^t_s: substation LTC tap position at any time t and is $1 \pm 0.00625*$substation LTC tap position, if present, 1 otherwise. v_s: fixed source voltage in per unit (p.u.). $\boldsymbol{v}_h(\boldsymbol{v}_l)$: Vector of user-defined upper (lower) voltage thresholds in per unit (p.u.).

Decision Variables: $\boldsymbol{p}^t_G = [p^t_{G,1}, ..., p^t_{G,n_G}]^T$: Vector of real power dispatch set points for all n_G DPV inverters. $\boldsymbol{q}^t_G = [q^t_{G,1}, ..., q^t_{G,n_G}]^T$: Vector of reactive power dispatch set points for all

n_G DPV inverters. $\boldsymbol{p}_B^t = [p_{B,1}^t, ..., p_{B,n_B}^t]^T$: Vector of charging or discharging rates for all n_B BESS inverters. Sign of the variable determines whether the BESS will charge or discharge at any time t. $\boldsymbol{q}_B^t = [q_{B,1}^t, ..., q_{B,n_B}^t]^T$: Vector of reactive power dispatch set points for all n_B BESS inverters. $\boldsymbol{v}^t = [v_{1,a}^t, ..., v_{N,c}^t]^T$: Vector of all nodal voltages.

A three-phase unbalanced, linearized OPF for the DERMS controller is developed for this study. The DERMS controller has been modeled in MATLAB using Yalmip. The power flow used in this controller is based on the *Simplified DistFlow* model proposed in [64]. This model is a linearized version of the non-linear *branch flow* equations [65]. These equations can be expressed in matrix form using (1) for a distribution system consisting of $N+1$ buses [66]. Buses are denoted by the set $\mathcal{B} \cup \{0\}$, $\mathcal{B} := \{1, ..., N\}$ and distribution lines by the set $\mathcal{L} := \{(m, n) \subset (\mathcal{B} \cup \{0\})X(\mathcal{B} \cup \{0\})$. The 0th bus is the secondary bus of the substation transformer with or without a OLTC.

$$\boldsymbol{v} = \boldsymbol{K}\boldsymbol{p} + \boldsymbol{M}\boldsymbol{q} + v_s\mathbf{1} \tag{2.1}$$

The K and M matrices in (2.1) are created using average impedance values of the three phases to create a simplified single-phase expression. However, distribution systems are unbalanced, hence (2.1) is extended to include all phases on each bus in this chapter. Thus, all vectors will be of the form $\boldsymbol{p} = [p_{1,a}, p_{1,b}, ..., p_{N,c}]^T$; $\boldsymbol{q} = [q_{1,a}, q_{1,b}, ..., q_{N,c}]^T$ and $\boldsymbol{v} = [v_{1,a}, v_{1,b}, ..., v_{N,c}]^T$.

Each term a_{ij} in $\boldsymbol{K}^{3N\times 3N}$ and $\boldsymbol{M}^{3N\times 3N}$ matrices is a coefficient which represents the change in voltage of node i from the source voltage v_s due to a real or reactive power injection at any node $j = \{1, ..., 3N\}$. These coefficients are determined using the scalable perturb and observe method [67]. In this method, a generator is placed successively on each node. A small real power $\Delta p_i \sim 0.05 s_{G,i},\ i = 1, ..., n_G$ is then injected from this generator while keeping all other nodal injections constant. The differences in voltage vector $\boldsymbol{v}^0$ before the

Δp_i injection, and the voltage vector $\boldsymbol{v}^n$ after the injection, are used to create each column of the $\boldsymbol{K}$ matrix. Each element of the K matrix will be of the form $(v_j^n - v_j^0)/\Delta p_i,\ i, j \in \mathcal{B}$. The process is repeated with ΔQ injections to generate the $\boldsymbol{M}$ matrix. This method is performed once at peak loading conditions.

The designed DERMS controller determines the optimal real $\boldsymbol{p}_G^t$, $\boldsymbol{p}_B^t$ and reactive $\boldsymbol{q}_G^t$, $\boldsymbol{q}_B^t$ power set points for all the inverters. It minimizes the curtailment of DPV systems while keeping the BESS systems charged (2.4). Since the objective function aims to keep the BESS charged, any excess DPV generation can be used to charge the BESS instead of curtailing it which further minimizes DPV curtailment. The augmented three phase unbalanced linearized power flow constraint (2.5) based on (2.1) gives a relation between the nodal voltages $\boldsymbol{v}^t$ and the net real $(\boldsymbol{p}_G^t + \boldsymbol{p}_B^t - \boldsymbol{p}_L^t)$ and reactive $(\boldsymbol{q}_G^t + \boldsymbol{q}_B^t - \boldsymbol{q}_L^t + \boldsymbol{q}_C^t)$ power injections. Nodal voltages $\boldsymbol{v}^t$ are maintained within Range A of the ANSI C84.1-2016 standard [68] or any user defined thresholds (v_l, v_h) using (13). Any storage unit $m, m = 1, ..., n_B$ is characterized by its kW rating $k_{B,m}$, maximum energy storage rating $e_{B,m}^{max}$ kWh, minimum energy reserve $e_{B,m}^{res}$ kWh and its current state of charge $e_{B,m}^t$ kWh. Thus, the maximum rate at which BESS may be charged $p_{B,m}^{chg,t}$ or discharged $p_{B,m}^{dischg,t}$ during a τ-minute dispatch interval t is given, respectively by (2.2) and (2.3), limited by $k_{B,m}$.

$$p_{B,m}^{chg,t} = \frac{e_{B,m}^{max} - e_{B,m}^t}{\frac{\tau}{60}} kW \tag{2.2}$$

$$p_{B,m}^{dischg,t} = \frac{e_{B,m}^t - e_{B,m}^{res}}{\frac{\tau}{60}} kW \tag{2.3}$$

Thus, the optimization problem being solved by the DERMS controller at each dispatch interval is given by (2.4)-(2.15).

Objective:

$$max(\sum_{i=1}^{n_G} p_{G,i}^t + \sum_{m=1}^{n_B} p_{B,m}^t) \Leftrightarrow$$
$$-min(-\sum_{i=1}^{n_G} p_{G,i}^t - \sum_{m=1}^{n_B} p_{B,m}^t) \tag{2.4}$$

Constraints:

$$\boldsymbol{v}^t = \boldsymbol{K}(\boldsymbol{p}_G^t + \boldsymbol{p}_B^t - \boldsymbol{p}_L^t) +$$
$$\boldsymbol{M}(\boldsymbol{q}_G^t + \boldsymbol{q}_B^t - \boldsymbol{q}_L^t + \boldsymbol{q}_C^t) + a_s^t v_s \mathbf{1} \tag{2.5}$$

$$\boldsymbol{p}_{Gmin}^t \leq \boldsymbol{p}_G^t \leq \boldsymbol{p}_{Gmax}^t \tag{2.6}$$

$$\boldsymbol{p}_B^t \leq \boldsymbol{p}_B^{chg,t} \tag{2.7}$$

$$\boldsymbol{p}_B^t \leq \boldsymbol{p}_B^{dischg,t} \tag{2.8}$$

$$p_{B,m}^{chg,t} = \begin{cases} k_{B,m}, & \text{if } \frac{e_{B,m}^{max} - e_{B,m}^t}{\frac{\tau}{60}} \geq k_{B,m} \\ \frac{e_{B,m}^{max} - e_{B,m}^t}{\frac{\tau}{60}}, & \text{if } 0 \leq \frac{e_{B,m}^{max} - e_{B,m}^t}{\frac{\tau}{60}} \leq k_{B,m} \\ 0, & \text{otherwise} \end{cases} \tag{2.9}$$

$$p_{B,m}^{dischg,t} = \begin{cases} k_{B,m}, & \text{if } \frac{e_{B,m}^t - e_{B,m}^{res}}{\frac{\tau}{60}} \geq k_{B,m} \\ \frac{e_{B,m}^t - e_{B,m}^{res}}{\frac{\tau}{60}}, & \text{if } 0 \leq \frac{e_{B,m}^t - e_{B,m}^{res}}{\frac{\tau}{60}} \leq k_{B,m} \\ 0, & \text{otherwise} \end{cases} \tag{2.10}$$

$$\boldsymbol{q}_{Gmin} \leq \boldsymbol{q}_G^t \leq \boldsymbol{q}_{Gmax} \tag{2.11}$$

$$\boldsymbol{q}_{Bmin} \leq \boldsymbol{q}_B^t \leq \boldsymbol{q}_{Bmax} \tag{2.12}$$

$$\boldsymbol{v}_l \leq diag(\boldsymbol{a}^t)\boldsymbol{v}^t \leq \boldsymbol{v}_h \tag{2.13}$$

$$(p^t_{G,i})^2 + (q^t_{G,i})^2 \leq s^2_{G,i} \tag{2.14}$$

$$(p^t_{B,m})^2 + (q^t_{B,m})^2 \leq s^2_{B,m} \tag{2.15}$$

$i = \{1, ..., n_G\};\ m = \{1, ..., n_B\};\ t = \{1, ..., t_{sim}\}$

In this formulation, functions (2.4)-(2.8), (2.11)-(2.13) and (2.16) are convex affine functions while (2.14), (2.15) are convex quadratic constraints with positive definite Hessian. As proved in Appendix A.1, this OPF formulation is convex which ensures that any local minima obtained will also be the global minima. This OPF formulation works for the grid-connected mode. It can also be used for steady state resiliency mode operation by including a power balance constraint (2.16).

$$\sum_{i=1}^{n_G} p^t_{G,i} + \sum_{i=1}^{n_B} p^t_{B,m} - \sum_{l=1}^{n_L} p^t_{L,l} = 0 \tag{2.16}$$

2.1.3 Co-simulation for DERMS CPS Model

The DERMS CPS model is simulated and time-synchronized through co-simulation between cyber system and physical system. Time-synchronization between these two systems is a key factor as DERMS controller action depends on effective communication with field measurements within an acceptable latency range. To enable efficient data exchange, the co-simulation environment is modeled through open-source OPC communication [19]. It is a client-server architecture for real-time communication where data is read/written into the data tags at the OPC server. These tags can be accessed by the connected clients including the Cyber layer (Simulink), feeder model (OpenDSS), and DERMS controller (MATLAB).

A randomized Gaussian noise with zero mean $\mu = 0$ and $\sigma = 5\%$ is added to each element

of these input vectors [69]. This error simulates the impact of metering errors, data packet drops and differences in dispatch intervals and simulation resolution. Metering errors result in AMI measurements to be different from the actual values of the state variables. Similarly, if a data packet is dropped, the corresponding variable will not be updated in the OPF formulation and its previous value would have to be used, which would be different from the actual value. Finally, due to differences in dispatch intervals (every minute) and simulation resolution (every 15-seconds) the state variables would have changed from the measurements reaching the DERMS controller. To account for these differences between measured values and actual state variable values, all measurements have been modeled as random variables with a Gaussian noise with zero mean $\mu = 0$ and $\sigma = 5\%$ [69]. Thus, any measurement vector such as the real load demand vector $\boldsymbol{p}_L^t$ will be represented as a random variable $\hat{\boldsymbol{p}}_L^t = \mathcal{N}(\boldsymbol{p}_L^t, \sigma^2)$, where $\mathcal{N}$ represents Gaussian distribution with zero mean and prespecified variance.

To avoid a loss of data packets, limited information is sent through the cyber layer for data exchange between the feeder model and the DERMS controller. The communication capable inverters send $\boldsymbol{p}_{Gmax}^t$, $\boldsymbol{p}_B^{chg,t}$, $\boldsymbol{p}_B^{dischg,t}$ and their PCC voltages $\boldsymbol{v}^t$ to DERMS and receive $\boldsymbol{p}_G^t$, $\boldsymbol{p}_B^t$, $\boldsymbol{q}_G^t$, $\boldsymbol{q}_B^t$ dispatch set points from it. The load AMI meters can only send their P and Q demands. AVRs and capacitor banks send their current tap positions and operational states, respectively, but cannot execute or receive any control commands from the DERMS controller as they have localized controllers.

2.2 Falsification of Control Commands

The DERMS controller and components of the ICT layer may be in remote substations. Malware can be installed, or spear phishing attacks may be used to gain access to their

communication paths [21]. An adversary can use the DERMS controller to cause voltage violations in an attack by falsifying the dispatch control commands. From Fig. 1, it is seen that the attacker can modify the optimal dispatch set points in the cyber layer which is a high probability but low severity attack. A relatively lower probability but higher severity cyberattack would involve modifications to the DERMS controller's algorithm after gaining unauthorized access. Both attack paths and attack models are presented here.

2.2.1 Attack Path 1: Cyber Layer

In the first attack path, Attack 1 as shown in Fig. 2.1, the attacker modifies the optimal dispatch set points in such a manner as to cause overvoltage violations. Being only present in the cyber layer, the adversary does not have access to the DERMS control logic in this attack model. The way to successfully cause overvoltage is by curtailing real power $\boldsymbol{p}_G^t = \mathbf{0}$, $\boldsymbol{p}_B^t = \mathbf{0}$, and maximizing reactive power injection $\boldsymbol{q}_G^t = \boldsymbol{q}_{Gmax}^t$, $\boldsymbol{q}_B^t = \boldsymbol{q}_{Bmax}^t$, from all the inverters. This effectively makes the inverters to act as distributed capacitor banks.

Voltages can be further increased if the attack is carried out at low load and high irradiance conditions. In contrast, if the attack is carried out at high load conditions, increase in Q injections would be absorbed locally, preventing severe overvoltage from occurring.

2.2.2 Attack Path 2: DERMS Centralized Controller

The severity of the first attack path may be limited. This is because at low load and high irradiance conditions, the AVRs would have moved to low tap positions and capacitor banks would have turned OFF to mitigate overvoltage. In this second attack path, Attack 2 as shown in Fig. 2.1, the attacker modifies the DERMS controller's software itself. This can be done either through a spear phishing attack or by physically accessing it. DERMS's software

cannot be hard coded in read only mode either, as it requires frequent updates with changes in the feeder's DPV and BESS penetration.

To maximize damage, the attacker could move the AVRs to higher tap positions and switch ON the capacitor banks (stage 1). Then the inverters would inject an optimal amount of real and reactive power to maximize voltages on the feeder (stage 2). However, AVRs and capacitor banks are not under remote control and thus inverter outputs need to be dispatched in such a manner that it indirectly triggers the AVRs and capacitor banks to operate.

Capacitor banks are usually voltage controlled and are switched ON when the voltage falls below a certain threshold. Thus, if the capacitor banks' point of common coupling (PCC) voltages are reduced, they will be switched ON.

The AVRs have a line drop compensator (LDC) circuit which determines its tap position. The LDC estimates the voltage at its load center (v_{LC}) based on its local voltage (v_{LDC}) and current (i_{LDC}) measurements given by (2.17) [9].

$$v_{LC} = v_{LDC} - (r_{LDC} + jx_{LDC})i_{LDC}\ V \tag{2.17}$$

If V_{LC} is below a certain threshold, AVR would raise taps to mitigate low voltages. This can be achieved by reducing the AVR's PCC voltage (v_{LDC}) and increasing the current (i_{LDC}). This reduction in PCC voltage and increase in AVR current can be achieved by making the inverters curtail real power and absorb reactive power. The inverters will effectively start acting as inductive loads and lower the feeder voltages. This will move AVRs to higher tap positions and switch ON capacitor banks as well.

The reactive power to be injected by each inverter can be obtained by modifying the DERMS objective function and voltage thresholds. For stage 1, the objective function would be

modified to minimize voltages given by (2.18), while the voltage thresholds would be lowered as given by (2.19).

$$min(\sum_{i=1}^{3N} v_i^t) \tag{2.18}$$

$$\boldsymbol{v}_{l1} \leq diag(\boldsymbol{a}^t)\boldsymbol{v}^t \leq \boldsymbol{v}_{h1} \tag{2.19}$$

Here, $\boldsymbol{v}_{l1}$ is the lower voltage threshold for stage 1. These limits must be set such that the inverters do not trip in this first stage of the attack. As per IEEE1547, the undervoltage tripping threshold can be ~$0.85p.u.$; while $\boldsymbol{v}_{h1}$ can be kept around 1 p.u. to ensure OPF converges.

Once these devices are in a state to increase voltages, the immediate next step for stage 2 would be to cause overvoltage by increasing P and Q injections. This is done by modifying the objective and voltage thresholds to

$$max(\sum_{i=1}^{3N} v_i^t) \;\Leftrightarrow\; -min(-\sum_{i=1}^{3N} v_i^t) \tag{2.20}$$

$$\boldsymbol{v}_{l2} \leq diag(\boldsymbol{a}^t)\boldsymbol{v}^t \leq \boldsymbol{v}_{h2} \tag{2.21}$$

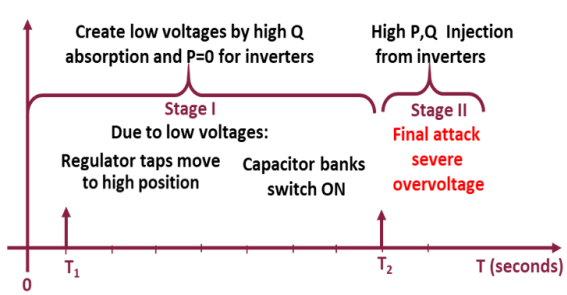

Figure 2.2: Two-stage cyberattack using DERMS controller

Here $\boldsymbol{v}_{l2}$ can be around $1p.u.$ which ensures feasibility, while $\boldsymbol{v}_{h2}$ can be any higher number

say $1.50p.u.$ to cause as high voltages as possible. This two-step attack is summarized in Fig. 2.2. Thus, irrespective of how complex the DERMS logic may be, by modifying the objective function and voltage thresholds severe cyberattacks influencing all feeder components may be executed.

2.3 Two-Tiered Intrusion Detection System

The cyberattack paths identified in section III involve falsification of data packets or modification of DERMS software to generate falsified control commands. To detect and mitigate these cyberattacks, a two-tiered intrusion detection system (IDS) is presented here. The first centralized tier detects and mitigates cyberattacks involving falsified control commands, manipulated measurement data packets and replay attacks. Inverter based decentralized tier provides backup protection against those cyberattacks where the malicious data packets appear legitimate. Both tiers work together to detect and mitigate different types of cyberattacks as shown in Fig. 2.3. This two-tiered IDS detects the attacks in the cyber layer itself and prevents the physical layer from being impacted.

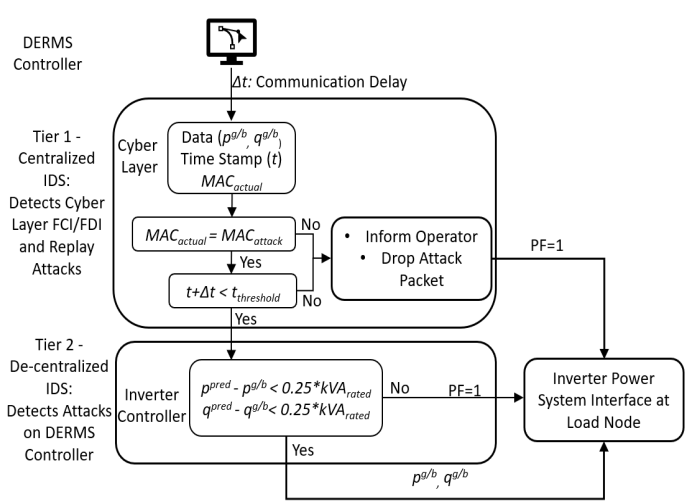

Figure 2.3: Methodology of the proposed two-tiered IDS

2.3.1 Tier 1: Centralized Detection

In the first attack model described in section 2.2, the optimal dispatch set points are modified in the cyber layer. Cyber layer-based ID techniques used for the attack model are presented here. A major advantage of the proposed approach is that it is not dependent on the physics of power systems and can thus identify malicious data packets both on the receiving and transmitting ends irrespective of what physical quantity they represent.

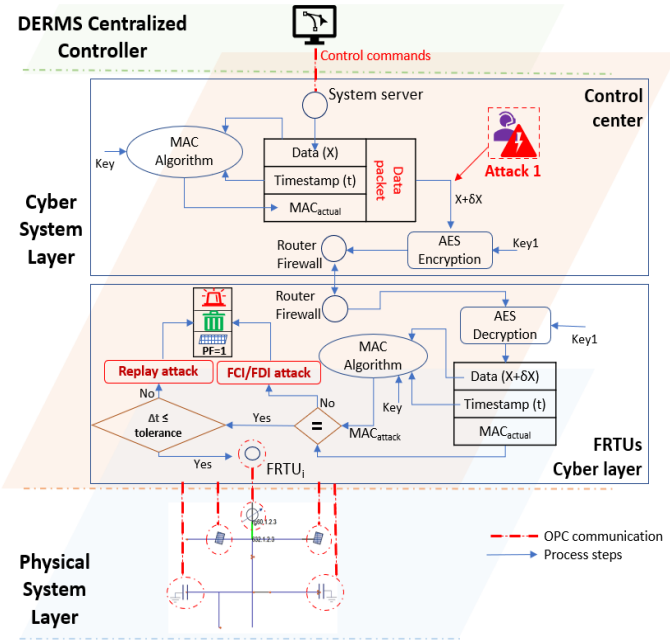

Figure 2.4: Tier 1: Cyber layer based centralized intrusion detection system

In the proposed system, a combination of timestamp and message authentication code (MAC) algorithm has been used for attack detection along with data encryption for added security, as shown in Fig. 2.4. A symmetric key-based encryption algorithm, Advanced Encryption Standard (AES) is used here due to its mathematical efficiency and effective cryptography [70]. The MAC system consists of a key generation algorithm which selects a key at random and a signing algorithm which efficiently returns a code or tag unique to the key and the data. Furthermore, the same key is used in the MAC algorithm at the receiving

side to verify the authenticity of the data [21]. This cyber layer-based IDS is termed *Timestamp based MAC-IDS* that specifically detects false control/data injection (FCI/FDI), and replay cyberattacks.

In reference to Fig. 2.4, the DERMS controller generates optimal dispatch set points (control commands), which are communicated to the system server in the control center cyber layer through OPC communication. The control command, i.e. Data (X) and its timestamp along with a key (Key) are used in the MAC algorithm to generate the control command authentication code $\text{MAC}_{\text{actual}}$. The data, timestamp and $\text{MAC}_{\text{actual}}$ are encrypted as a data packet using a 256-bit symmetric key ($Key1$) in AES Encryption algorithm. The encrypted command packet is sent through the queuing system from the router of the control center to that of the FRTUs.

In the FRTUs cyber layer, after each packet is received at their destination FRTU via the queueing system, the encrypted packet is decrypted using the same key, $Key1$. The decrypted data and timestamp received goes though MAC algorithm along with the Key to generate a code, i.e., $\text{MAC}_{\text{attack}}$.

The decrypted $\text{MAC}_{\text{actual}}$ is compared with $\text{MAC}_{\text{attack}}$. If the two values are different, then the command packet is flagged to have undergone a FCI attack. If the MAC values are equal, it indicates that there has been no data tampering. However, to check for replay attack, the difference between timestamp values when data packet is sent and is received (Δt) is checked against a tolerance value. The tolerance limit is based on the maximum designed delay of the communication layer. The occurrence of a replay attack is considered when (Δt) is above the tolerance. When (Δt) is within tolerance limits, the data packet is considered safe and forwarded to the physical layer. However, if either a replay or FCI attack is detected, a three-step response is initiated. The operator is notified through an alarm, the malicious control command packets are dropped and consequently the inverters

switch to localized unity power factor ($PF = 1$) mode.

Both FCI and replay attacks are detected using the proposed *Timestamp based MAC-IDS*. In case of a FCI attack where the command is modified before it is encrypted, $\delta X \neq 0$, $\text{MAC}_{\text{actual}}$ and $\text{MAC}_{\text{attack}}$ will not match, since MAC is based on data and timestamp combination. Similarly, in a replay attack the adversary might capture a previous time point's data packet and maliciously repeat it at another time to deceive detection schemes. In this case, the MAC values will be the same; however, Δt will be significantly higher than the tolerance value as the timestamp of the repeated data packet will correspond with a previous dispatch interval. *Timestamp based MAC-IDS* screens AMI measurement data packets in a similar manner when they are sent from the physical layer to the DERMS controller.

2.3.2 Tier 2: De-centralized Detection

In the second cyberattack model, the DERMS controller is attacked as shown in Fig. 2.1. Since the DERMS controller's software has been modified as described in section III.B, malicious command data packets appear legitimate and centralized defense mechanisms will not work. As such the inverters need to be able to detect the malicious control commands and prevent them from being implemented. The expected PCC nodal voltage at any node i after applying the optimal dispatch set points is determined with sufficient accuracy using (2.5). However, this would require programming the entire i^{th} row of $\boldsymbol{K}$ and $\boldsymbol{M}$ sensitivity matrices in each inverter, as these matrices are dense and are not diagonally dominant. Furthermore, each element of the $\boldsymbol{p}$ and $\boldsymbol{q}$ vectors along with a_s and v_s will need to be communicated centrally.

The cyberattack thus needs to be identified using locally available measurements. While algorithms such as non-linear autoregressive neural network (NARX) [13] may be applied

at the centralized level, inverters do not have sufficient computational power to process non-linear expressions. Thus, multivariate linear regression (MLR) [22] is used to create linearized expressions (2.22), (2.23) to determine expected control command values based on local load and maximum power point value (based on irradiance) for DPV inverters.

$$p_{G,i}^{pred,t} = \alpha_{G,i}^{0,p} + \alpha_{G,i}^{1,p} * p_{L,i}^{t} + \alpha_{G,i}^{2,p} * q_{L,i}^{t} + \alpha_{G,i}^{3,p} * p_{Gmax,i}^{t} \tag{2.22}$$

$$q_{G,i}^{pred,t} = \alpha_{G,i}^{0,q} + \alpha_{G,i}^{1,q} * p_{L,i}^{t} + \alpha_{G,i}^{2,q} * q_{L,i}^{t} + \alpha_{G,i}^{3,q} * p_{Gmax,i}^{t} \tag{2.23}$$

Similar linearized expressions (2.24), (2.25) are also created for BESS inverters to determine expected control command values based on local load and maximum charging and discharging rate values.

$$\begin{aligned} p_{B,m}^{pred,t} = \alpha_{B,m}^{0,p} + \alpha_{B,m}^{1,p} * p_{L,m}^{t} + \alpha_{B,m}^{2,p} * q_{L,m}^{t} + \\ \alpha_{B,m}^{3,p} * p_{B,m}^{chg,t} + \alpha_{B,m}^{4,p} * p_{B,m}^{dischg,t} \end{aligned} \tag{2.24}$$

$$\begin{aligned} q_{B,m}^{pred,t} = \alpha_{B,m}^{0,q} + \alpha_{B,m}^{1,q} * p_{L,m}^{t} + \alpha_{B,m}^{2,q} * q_{L,m}^{t} + \\ \alpha_{B,m}^{3,q} * p_{B,m}^{chg,t} + \alpha_{B,m}^{4,q} * p_{B,m}^{dischg,t} \end{aligned} \tag{2.25}$$

Here $\alpha_i, i = 0, .., 4$, terms represent the coefficients for each localized measurement and are the decision variables. Taking (2.22) as an example, the expression for $p_{G,i}^{pred}$ at any time $t = 1, .., T^{tr}$ may be represented as, $p_{G,i}^{pred,t} = (\boldsymbol{x}^t)'\boldsymbol{\alpha} \approx p_{G,i}^{act,t}$, where $\boldsymbol{x} = [1, p_{L,i}^{t}, q_{L,i}^{t}, p_{Gmax,i}^{t}]'$, $\boldsymbol{\alpha} = [\alpha_{G,i}^{0,p}, \alpha_{G,i}^{1,p}, \alpha_{G,i}^{2,p}, \alpha_{G,i}^{3,p}]'$. $p_{G,i}^{act,t}$ is the actual real power set point received by inverter i from the DERMS controller at any time t from the training dataset consisting of T^{tr} measurements. 5% of the simulated data points were used as training data. $\boldsymbol{\alpha}$ may be obtained using the

least squares cost function given by,

$$h(\boldsymbol{\alpha}) = \frac{1}{T^{tr}} \sum_{t=1}^{T^{tr}} ((\boldsymbol{x}^t)^{'} \boldsymbol{\alpha} - p_{G,i}^{act,t})^2 \tag{2.26}$$

The unconstrained optimization problem to find $\boldsymbol{\alpha}^*$, which minimizes the sum of squared errors for all T^{tr} training samples, is

$$\underset{\boldsymbol{\alpha}}{\text{minimize}} \frac{1}{T^{tr}} \sum_{t=1}^{T^{tr}} ((\boldsymbol{x}^t)^{'} \boldsymbol{\alpha} - p_{G,i}^{act,t})^2 \tag{2.27}$$

The tth term of this cost function is,

$$h^t(\boldsymbol{\alpha}) = ((\boldsymbol{x}^t)^{'} \boldsymbol{\alpha} - p_{G,i}^{act,t})^2 \tag{2.28}$$

Expanding,

$$h^t(\boldsymbol{\alpha}) = (p_{G,i}^{act,t})^2 - 2(\boldsymbol{x}^t)' \boldsymbol{\alpha} p_{G,i}^{act,t} + (\boldsymbol{x}^t)^{'} \boldsymbol{\alpha} (\boldsymbol{x}^t)^{'} \boldsymbol{\alpha} \tag{2.29}$$

As $(\boldsymbol{x}^t)^{'} \boldsymbol{\alpha} = \boldsymbol{\alpha}^{'} \boldsymbol{x}^t$,

$$h^t(\boldsymbol{\alpha}) = (p_{G,i}^{act,t})^2 - 2(\boldsymbol{x}^t)' \boldsymbol{\alpha} p_{G,i}^{act,t} + \boldsymbol{\alpha}^{'} \boldsymbol{x}^t (\boldsymbol{x}^t)^{'} \boldsymbol{\alpha} \tag{2.30}$$

Therefore for all T^{tr} training samples, the cost function $h(\boldsymbol{\alpha})$ is given by,

$$= \frac{1}{T^{tr}} (\sum_{t=1}^{T^{tr}} (p_{G,i}^{act,t})^2 - 2 \sum_{t=1}^{T^{tr}} p_{G,i}^{act,t} (\boldsymbol{x}^t)^{'} \boldsymbol{\alpha} + \sum_{t=1}^{T^{tr}} \boldsymbol{\alpha}^{'} \boldsymbol{x}^t (\boldsymbol{x}^t)' \boldsymbol{\alpha}) \tag{2.31}$$

This function is of the form of a generalized quadratic function,

$$\boldsymbol{\alpha}^{'} \boldsymbol{Q} \boldsymbol{\alpha} + \boldsymbol{k}^T \boldsymbol{\alpha} + c \tag{2.32}$$

where,

$c = \frac{1}{T^{tr}} \sum_{t=1}^{T^{tr}} (p_{G,i}^{act,t})^2$,

$\boldsymbol{k} = -\frac{2}{T^{tr}} \sum_{t=1}^{T^{tr}} p_{G,i}^{act,t} (\boldsymbol{x}^t)$, and

$\boldsymbol{Q} = \frac{1}{T^{tr}} \sum_{t=1}^{T^{tr}} \boldsymbol{x}^t (\boldsymbol{x}^t)'$

Being a sum of outer product matrices, eigenvalues of $\boldsymbol{Q}$ are non-negative and hence $\boldsymbol{Q}$ is positive semi-definite [71]. Thus, the cost function is a convex quadratic function and $\boldsymbol{\alpha}^*$ may be obtained in a single step using the Newton's method. Steepest gradient descent method may also be used as it is globally convergent for convex quadratic functions and avoids matrix inversion.

These MLR expressions are determined once and then programmed in the inverters. The inverters then determine the expected control command values $p_{G,i}^{pred,t}$, $q_{G,i}^{pred,t}$, $p_{B,m}^{pred,t}$ and $q_{B,m}^{pred,t}$ at each time point using (2.22)-(2.25) and compare them against the actual optimal dispatch control commands received. If differences between these values are larger than a specified tolerance, the inverters move to PF=1 mode.

2.4 Case Study

The proposed DERMS controller, cyberattack models and their mitigation strategies have been validated by the IEEE 13-bus (32 nodes) and IEEE 123-bus (262 nodes) test feeders. A total of 17 DPV systems with the same kVA rating as the loads are added on each node of the 13-bus feeder. 3 BESS totaling 1MW/2MWh are added on one of the buses. The 13-bus feeder is used to validate the proposed methodology while scalability is validated using the larger 123-bus test feeder. 96 DPV systems and 6 BESS (total 0.5MW/1MWh) are deployed in the 123-bus test feeder. These DPV and BESS inverters can inject or absorb reactive power equal to their rated kVA. Each DPV system and load has unique 15-second resolution

profiles taken from real world measurements.

IEEE 123-bus feeder has 262 nodes. Each node hosts a DPV and BESS system at 100% DER penetration level. Each node will thus send 5 data packets namely the maximum BESS charging and discharging rates, irradiance value, and real and reactive power load demands. They will in turn receive optimal real and reactive power dispatch settings from the DERMS controller. Maximum data packets to be sent or received in each 15-second interval are 1310 for the 123-bus feeder and thus a queue size of 1500 data packets is chosen. These data packets are processed in 5-seconds each way which leaves about 50 seconds for the various applications such as OPF and centralized IDS. Thus, the server processing rate considering 1 server (m=1) is 265 packets/second. The OPF only takes ~5.5 seconds for the IEEE 123-bus feeder which suggests that proposed OPF formulation and CPS model can manage a large number of DERs.

2.4.1 DERMS Centralized Controller

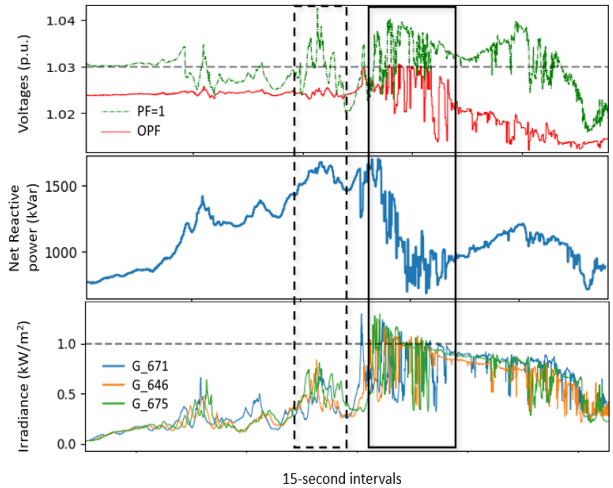

Figure 2.5: DERMS centralized controller maintains voltages within thresholds and minimizes DPV curtailment

Figure 2.5 shows the maximum of all nodal voltages observed in the OpenDSS model in the

top panel when PF=1 mode with no reactive power support is used (dashdot line). It also shows the maximum voltages when the DERMS controller (solid line) is used with random Gaussian errors ($\mu = 0, \sigma = 5\%$) in all the measurements at all time points to simulate real-world conditions. All subsequent results have these errors. The optimal dispatch settings are generated at 1-minute interval while the quasi-static time-series simulation progresses at 15-second resolution [72]. The middle panel shows the net reactive power support provided by all DPV and BESS inverters based on the optimal DERMS dispatch, while the bottom panel shows the irradiance profiles used for the 13- bus feeder. The voltage thresholds for the DERMS controller are kept at $(0.97, 1.03)$ p.u. The top panel in Fig. 2.5 clearly shows that the proposed DERMS controller can maintain voltages within the $\pm 3\%$ thresholds even with significant measurement errors.

When irradiance is low and inverters are not capacity constrained, sufficient reactive power support is provided and voltages are below the $\pm 3\%$ threshold as shown in the dotted box in Fig. 2.5. When the irradiance is high and inverters are capacity constrained, the net reactive power support is reduced while the maximum voltages reach the $+3\%$ threshold as shown in the solid line box. This shows that the proposed OPF formulation minimizes DPV curtailment by providing as much reactive power support as is necessary to maintain voltages within thresholds while meeting inverter capacity constraints. The DPV energy curtailment is less than 0.1% even on a peak summer day for both IEEE 13 and 123 bus test feeders.

2.4.2 Cyber-attack Models and Mitigation Results on IEEE 13-bus Feeder

The two cyberattack models presented in section 2.2 are executed when the DPV generation to load ratio is high. Both are severe short duration attacks and in Fig. 2.6 to Fig. 2.8,

the attacks start at dispatch interval 1 and continue for 3-minutes. Since these are short duration attacks, ANSI C84.1 threshold are not applicable as they consider longer 10-minute moving average voltages. The critical thresholds are inverter tripping thresholds based on IEEE 1547-2018 and IT device AC voltage boundary based on Information Technology Industry Council's (ITIC) curve [73],[74]. IEEE 1547-2018 suggests that inverters should trip if voltages go beyond $(\sim 0.85, 1.10) p.u.$ for about 15 seconds, while ITIC curve suggests IT equipment can be damaged if voltages go beyond $(0.9, 1.10) p.u.$ for more than 15-seconds.

Cyber Layer Attack (Attack 1) and Centralized Detection Results

In the first cyberattack model presented in section 2.2, the inverter set points are modified in the cyber layer after they are generated by the DERMS controller. All inverter based DPVs and BESSs curtail real power and inject reactive power equal to their kVA rating for all 3 minutes of the attack. Thus, a combination of low load and high capacitive injection leads to overvoltage (lines with triangles) beyond the applicable IEEE1547 and ITIC bounds for 43% of the nodes as can be seen in Fig. 2.6. However, violation severity and attack impact is limited as a capacitor bank (Cap1) is OFF (state: 0; dotted lines) and the substation OLTC (dashed line) is at low position (tap: 0) due to the high DPV to load ratio. Furthermore, after an internal delay the substation OLTC reduces taps to -11 and the other capacitor bank (Cap2) also turns OFF. This brings most nodal voltages within ANSI Range A limits, even though all the inverters continue to inject capacitive power equal to their kVA rating.

Figure 2.6 also shows the impact of the *Timestamp based MAC-IDS* ((CL): lines with Y symbols) proposed in section 2.3. It detects the falsified control commands in the cyber layer using the differences in MAC codes and drops the falsified data packets. This causes the inverters to move to PF=1 mode and none of the nodes experience voltages beyond the thresholds (Fig 2.6. (CL)). MAC codes are different since MAC_{actual} is generated using

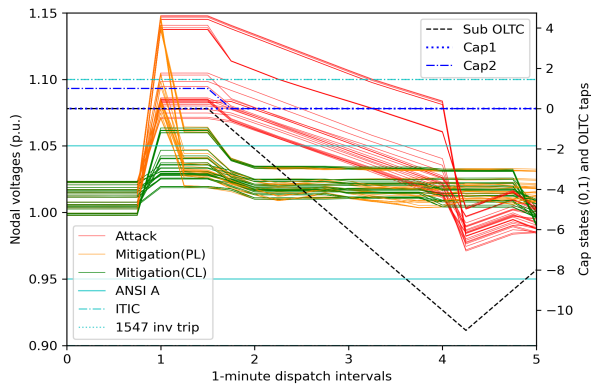

Figure 2.6: Nodal voltages and voltage regulating equipment states in cyber layer-based falsified control command cyberattack and detection

legitimate dispatch setpoints while MAC_{attack} is based on the falsified control commands introduced in the cyber layer.

The *Timestamp based MAC-IDS* can identify replay attacks as well, using the large difference Δt between the time stamp of the replayed data packets and the time when they reach the substation control center. The large Δt values, as shown in Fig. 2.7, for replayed data packets arise from the 15-second difference between successive data measurement intervals. The results presented in Fig. 2.7 are obtained by simulating different communication layer congestion levels, ranging from 10% -100% DER penetration. The ICT layer is designed to have a worst-case delay (Δt) of 5 seconds at 100% DER penetration [19]. Thus, the malicious repeated data packets have (Δt) between 10-20 seconds, while legitimate data packets have a maximum delay of 5 seconds. This large difference in (Δt) values is captured by *Timestamp based MAC-IDS* to detect replay attacks.

On the other hand, physical layer-based IDS such as that proposed in [13], is not able to detect the attack before it impacts the physical layer, as shown in Fig. 2.6 ((PL): solid lines). Nodal voltages exceed thresholds at least once before being detected. This is because the NARX based PL-IDS [13] predicts the expected measurement value and compares it against

the received measurement. If the difference is outside a specified tolerance, the measurement is classified as a FDI attack. As the control set points are modified in the cyber layer, voltage measurements will be outside tolerance only after the attack impacts the physical layer at least once. Moreover, this approach will fail to detect the cyberattack if the adversary also executes a replay attack using pre-attack voltage measurement data packets.

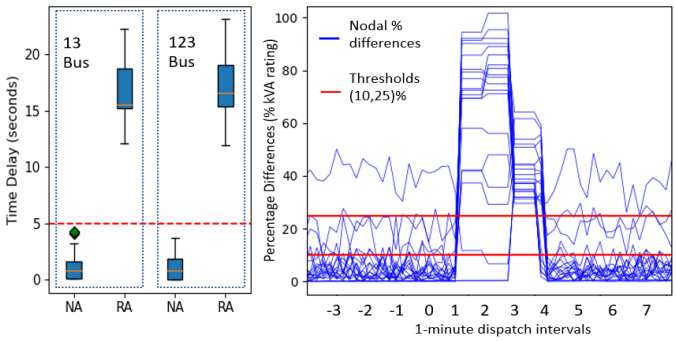

Figure 2.7: Detection of replay attacks (RA) by *Timestamp based MAC-IDS*

DERMS Controller Cyberattack (Attack 2) and Decentralized Detection Results

In the second attack model, the DERMS controller is attacked and its algorithm is modified to conduct a damaging two-stage attack as summarized in Fig. 2.2. The first stage starts at dispatch interval 1 and continues for 2-minutes till interval 3. As can be seen in Fig. 2.8 (lines with triangles), the first stage causes some nodal voltages to drop below $0.9p.u.$ thereby damaging IT equipment. However, none of the inverters trip as voltages do not fall below $0.85p.u.$ This causes the OLTC to move from tap position 0 to +6 and capacitor banks to switch ON to mitigate undervoltage. Then at dispatch interval 3, the DERMS voltage thresholds are changed to $(1.0, 1.5)p.u.$ and objective function is changed to maximize voltages. The effect of low load, high tap position and capacitor banks in the ON state combined with the capacitive injections from inverters causes all nodal voltages to exceed $1.10p.u.$ and reach as high as $1.20p.u.$. These voltages are much higher than in attack 1,

as the voltage regulating devices are indirectly influenced to move to higher tap positions even at low load conditions. Such high voltages would damage all IT equipment and trip the inverters.

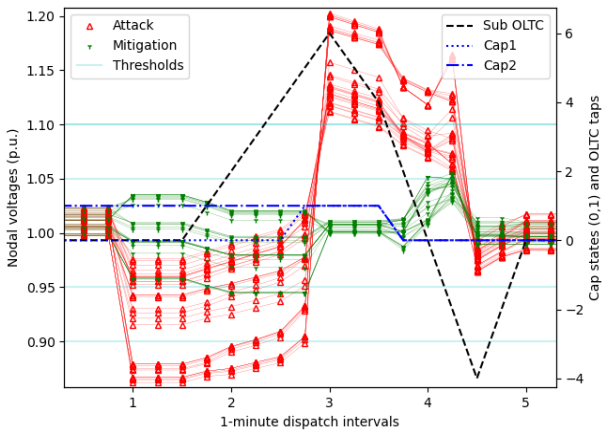

Figure 2.8: Nodal voltages and voltage regulating equipment states with the 2-stage falsified control command cyberattack and detection

This cyberattack is detected using the decentralized MLR based detection scheme proposed in section 2.3. Figure 2.7 (right) shows the differences between the estimated (22),(24) and received optimal real power set points for all the inverters. The differences are expressed as a percentage of the inverter's kVA ratings. A sensitivity analysis showed that due to the limited local information used for estimating these set points, the false positives are as high as 10% of all simulated time points when just 5% differences are allowed. These dropped to 0.04% with a larger 25% threshold. 10% differences are allowed between actual and estimated optimal set point values in this study. Most inverters can detect the cyberattack in the first stage itself as can be seen in Fig. 2.7. This prevents damaging voltages on all the nodes as shown in Fig. 2.8 (lines with Y symbols).

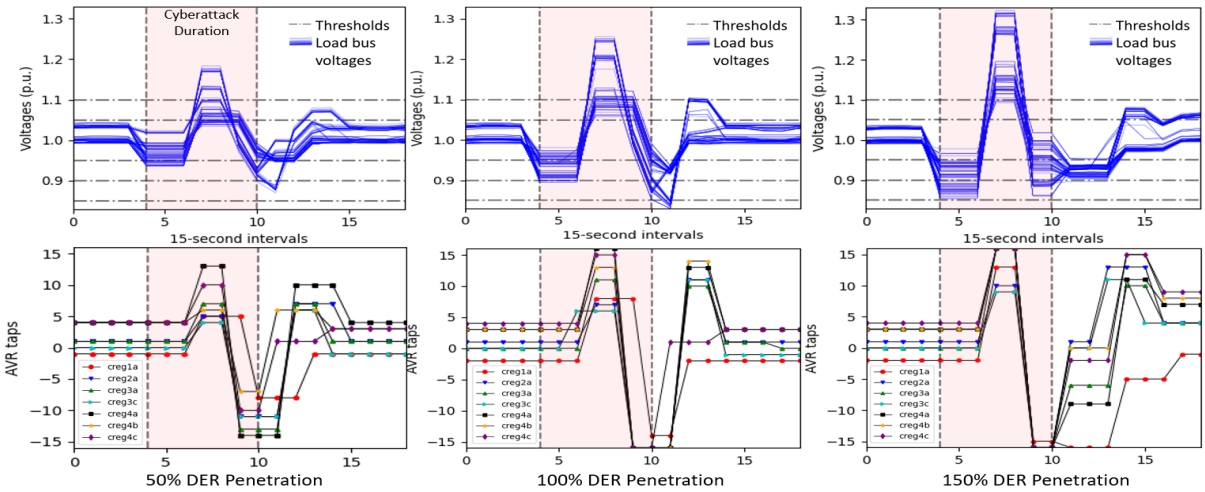

Figure 2.9: All load bus voltages after 2-stage cyberattack (top); and AVR taps positions (bottom)

2.4.3 Cyber-attack Models and Mitigation Results on IEEE 123-bus Feeder:

The scalability of the proposed methodology is evaluated using the IEEE 123-bus (262 nodes) test feeder as shown in Fig. 2.1. This feeder has a substation LTC and 6 AVRs, the LTC has a 3-phase controller (creg1a) and the 6 AVRs have 1-phase controllers (creg2a, creg3a, creg3c, creg4a, creg4b, creg4c). This feeder also has 4 uncontrolled capacitor banks. Three DER penetration levels are evaluated to assess the impact of cyberattacks and efficacy of proposed detection techniques. 50% DER penetration level has 3 BESS and 50 DPV systems, 100% level has 6 BESS and 96 DPV systems and the inverter capacity is increased by 50% in the 150% DER penetration level. Each OPF takes on average 5.5 seconds which is much smaller than the 1-minute dispatch interval and highlights the scalability of the proposed OPF formulation.

The 2-stage cyberattack was found to be more severe in this section and was carried out on the three DER penetration levels. The cyberattack was started at interval 4 and ended at

Table 2.1: Impact comparison of the 2-stage cyberattack on different DPV scenarios for 123-bus system

Scenarios	**Maximum Voltage Observed**	**Percent nodes >1.10 p.u.**
50 rooftop DPV, 0 large DPV, 3 BESS	1.184 p.u.	83/262 (32%)
96 rooftop DPV, 0 large DPV, 6 BESS	1.257 p.u.	161/262 (61%)
96 rooftop DPV, 0 large DPV, 6 BESS (Inverter kVA increased by 50%)	1.324 p.u.	254/262 (97%)
0 rooftop DPV, 2 large DPV, 6 BESS	1.256 p.u.	36/262 (14%)
94 rooftop DPV, 2 large DPV, 6 BESS	1.336 p.u.	182/262 (69%)

interval 10 in Figures 2.9 to 2.11. As can be seen in Fig. 2.9, the first stage reduces the voltages, causing the AVRs to move to higher tap positions. In the second stage damaging severe overvoltage occurs in all 3 DER penetration levels reaching as high as 1.32 p.u. as summarized in Table 2.1. The severity of overvoltage increases with the DER penetration level as more reactive power can be absorbed and injected. Even after the attack ends undervoltages are observed. This happens because the capacitive injections are removed after the attack ends but the AVRs have moved to lowest tap positions to mitigate overvoltages.

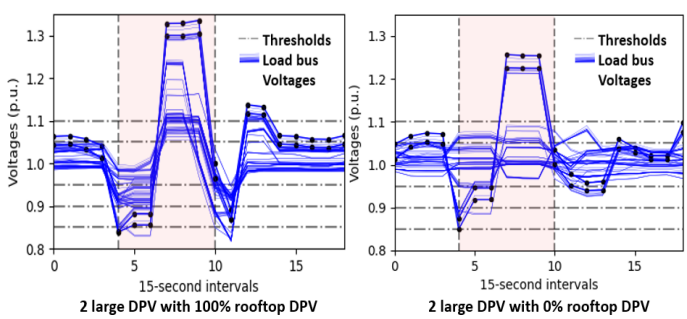

Figure 2.10: All load bus voltages after 2-stage cyberattack with 2 larger DPV and 100% rooftop DPV (left); two larger DPV and no rooftop DPV (right)

To further assess the cyberattack impacts, two large DPV systems of 400 kVA each are added at two randomly chosen buses (buses 85 and 103). Figure 2.10 shows all bus voltages (waveforms for buses 85 and 103 highlighted with circles) when the 2-stage cyberattack is

carried out with 94 distributed rooftop DPV along with these two large DPV systems and with just the two large DPV systems and no rooftop DPV. This figure shows that the buses which are deployed with the large DPV systems experience more severe voltages whereas in the absence of rooftop DPV fewer nodes are impacted as summarized in Table 2.1. This suggests that the proposed OPF formulation is robust enough to dispatch different numbers and sizes of DERs and the 2-stage cyberattack can impact all these DERs.

The proposed centralized detection can detect the cyber layer attacks using differences in MAC code and the replay attacks using difference in time stamps, as shown in Fig 2.7. The 2-stage cyberattacks shown in Fig. 2.9 are detected using the MLR based decentralized technique in section 2.3. The bottom plots in Fig. 2.11 show the differences between the reactive power dispatch setpoints received from the DERMS controller and those estimated using expressions (2.23) and (2.25). It can be seen that the proposed decentralized technique can detect the attack which causes the inverters to move to PF=1 mode and the cyberattack does not impact the physical layer in all three DER penetration levels.

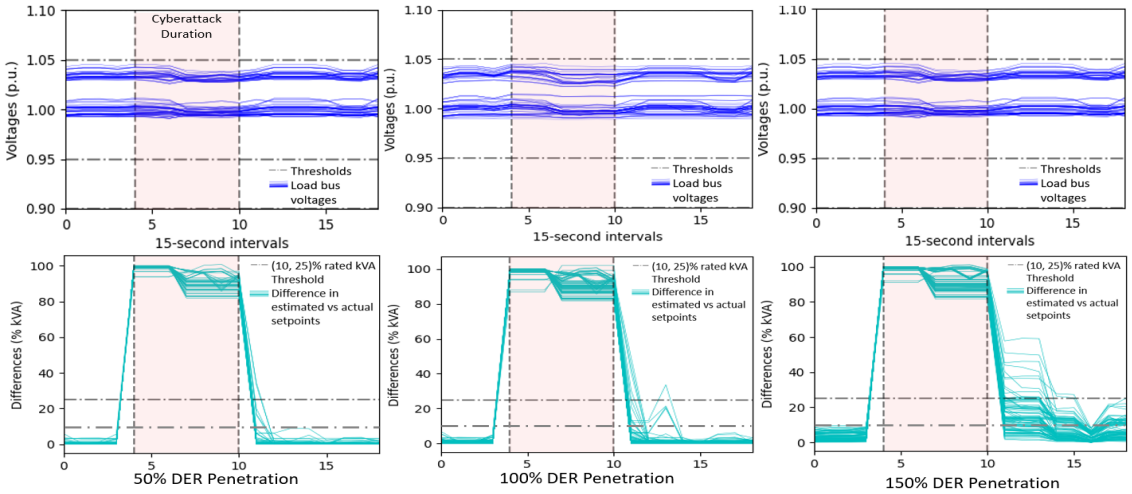

Figure 2.11: All load bus voltages after 2-stage cyberattack mitigation (top); and differences between MLR estimated setpoints and actual set points (bottom)

.

Chapter 3

Optimal Service Restoration of Microgrids

The ability to restore power supply after an outage is one of the most important microgrid functions. Restoring the entire microgrid in a single time step can cause unacceptably large transients. Thus a sequential microgrid restoration plan is required which can coordinate with all other devices in the microgrid. This plan is then implemented using the optimal dispatch algorithm presented in chapter 2. The remaining of this chapter is organized as follows: Section 3.1 describes the proposed optimal DER dispatch method for controlling unmonitored automatic voltage regulation devices. Section 3.2 presents the proposed generalized NM load demand model. The proposed MILP based sequential microgrid restoration approach incorporating automatic voltage regulation devices and NM loads is presented in section 3.3. A case study on an unbalanced model of the IEEE 123-node test feeder in

© 2024 IEEE. Reprinted, with permission, from A.K. Jain, C-C. Liu., A.K. Bharati, K. Schneider, F. Tuffner and D. Ton, "Microgrid Service Restoration Incorporating Unmonitored Automatic Voltage Controllers and Net Metered Loads", IEEE Transactions on Smart Grid, 2024.

OpenDSS [75] presented in section 3.4 demonstrates the effectiveness of the proposed approach.

3.1 Optimal Control Incorporating Unmonitored Automatic Voltage Controllers

Voltage regulation devices such as AVRs and capacitor banks may have automatic controllers. Based on the measured value of a local control parameter (typically voltage), the controller determines the control action. The control action for AVRs is a change in the tap position. The control action for capacitor banks is turning them ON or OFF based on the value of the control parameter. These devices are automatic and hence their states are not available to the centralized controller via AMI, nor can these be controlled remotely, as illustrated in Fig. 3.1. AMI is a bi-directional communication system that enables measurements and control commands to be sent between smart meters deployed in the distribution system and the utility control center. In this figure, the devices with communications can send and receive information from the centralized controller. For instance, the NM loads can send their net energy consumption in kWh periodically to the controller, which is then used to calculate the average kW net demand (p_i^n). In section 3.2, the NM demand forecasts during microgrid restoration will be generated using only these pre-outage NM time series. The devices with both communications and remote-control capabilities such as large DERs and remotely operable switches can send measurements and receive and implement control commands from the centralized controller.

The main contribution here is the development of an integrated approach for optimal control of these devices. Linearized constraints are developed which relate the AVR's local con-

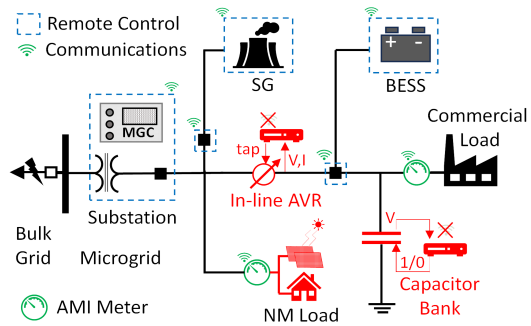

Figure 3.1: Typical microgrid topology with unmonitored automatic voltage controllers, NM loads and remotely controllable DERs and switches.

troller's operation principle with the determined optimal tap positions and DER dispatches. Constraint selection is then automated based on the sign of the optimal tap position. Optimal control of capacitor banks is achieved using a similar approach. Additional constraints required for integrating the proposed optimal control approach with MILP based sequential microgrid restoration algorithms are presented in section IV. All these constraints are integrated and solved simultaneously.

The variables and parameters are: $\mathcal{G}(\mathcal{B},\mathcal{E})$: Directed graph of the 3-phase microgrid; set of all nodes $\mathcal{B}$ and edges $\mathcal{E}$. θ: represents the phases $\theta \in \{a,b,c\}$. $P_{ij}^{\theta}(Q_{ij}^{\theta})$: Per phase real (reactive) power flow of edge $ij \in \mathcal{E}$. V_i^{θ}: Per phase nodal voltage of node $i \in \mathcal{B}$. $P_{i,k}^{L,\theta}(Q_{i,k}^{L,\theta})$: Per phase real (reactive) demand at node $i \in \mathcal{B}$ at time step k. $P_{i,k}^{G,\theta}(Q_{i,k}^{G,\theta})$: Per phase real (reactive) generation at node $i \in \mathcal{B}$ at time step k. $\mathcal{C},\mathcal{C}_c$: Set of 3-phase capacitor bank nodes, set of controllable capacitor bank nodes. $\bar{Q}_i^{C,\theta}$: Per phase kVA rating of capacitor bank $i \in \mathcal{C}$. Bar over symbols represents a parameter. $Q_{c,i}^{\theta}$: Per phase capacitive injection at node $i \in \mathcal{B}$. $\delta_{c,i}^{\theta}, q_{c,i}^{\theta}$: State and kVA rating estimates of capacitors. V_i^{on}, V_i^{of}: ON and OFF thresholds of capacitors $i \in \mathcal{C}_c$. $\mathcal{E}_R$: Set of 3-phase edges with AVRs. $r_{kj}^{\theta,v}, x_{kj}^{\theta,v}$: Line drop compensator (LDC) impedance settings in volts. c_{kj}^{p}, c_{kj}^{s}: Primary and secondary turns ratio of LDC's current transformer. p_{kj}: Turns ratio of the LDC's potential transformer. $V_{kj}^{r,\theta}$: LDC's estimated load center voltage. $V_{kj}^{\theta,l}, D_{kj}^{\theta,l}$: LDC's desired load center voltage setting

and allowable deadband. a^{θ}_{kj}: AVR tap position $kj \in \mathcal{E}_R$. p^n_i, p^d_i, p^g_i: Net and actual demand and solar generation of net-metered (NM) loads. $D^{p_i}_l, D^0_l$: Cold load pickup (CLPU) curve demands. $\hat{P}^{d,K}_i, \hat{P}^{g,K}_i$: Forecasted restoration demand and generation. $\hat{P}^{S_k}_i$: NM restoration stage demand forecasts. $\bar{M}^L_l$: NM demand forecast curves. $\mathcal{K}$: Set of restoration time steps $\mathcal{K} := \{1, .., K\}$. $\bar{r}^{\theta}_{ij}(\bar{x}^{\theta}_{ij})$: Per phase resistance (reactance) of edge $ij \in \mathcal{E}$. $\mathcal{E}_0$: Set of remotely operable switches. $\mathcal{S}$: Set of all load sections. $\delta^E_{ij} \in \{0, 1\}$: Energization status of edge $ij \in \mathcal{E}$. $\delta^N_i \in \{0, 1\}$: Energization status of node $i \in \mathcal{B}$. $\delta^S_s \in \{0, 1\}$: Energization status of load section $s \in \mathcal{S}$.

3.1.1 Determining Optimal States

The optimal states of AVRs and capacitor banks can be obtained in the same manner irrespective of whether these devices have remote control capabilities. For an AVR connected between nodes k and $j, k \rightarrow j$, the voltages on these nodes may be expressed as $V^{\theta}_j = a^{\theta}_{kj} V^{\theta}_k$, where a^{θ}_{kj} is the tap position of the AVR on phase $\theta \in \{a, b, c\}$. Here the loss term $(\bar{r}^{\theta}_{kj} P^{\theta}_{kj} + \bar{x}^{\theta}_{kj} Q^{\theta}_{kj})$ present in the linearized *DistFlow* power flow model [76] is ignored. a^{θ}_{kj} can only take discrete values in the range $[0.9, 1.1]$. These taps provide ± 0.1 p.u. voltage regulation with a 0.00625 p.u. step. These 33 tap positions can be expressed using a 6-bit code [77], which significantly reduces the number of binary variables needed from 33 to 6 for every single phase AVR. For instance, the code 100000 represents tap +16, code 000000 represents tap -16 and code 010000 represents tap 0 or the neutral position. Thus, the linearized voltage constraint for an AVR connected between nodes k and j is given by (3.1).

$$V^{\theta}_j = V^{\theta}_k (0.9 + 0.00625 \sum_{n=0}^{5} \delta^{\theta}_{kj,n} (2)^n), \delta^{\theta}_{kj,n} \in \{0, 1\}, kj \in \mathcal{E}_R \tag{3.1}$$

The products of binary variables $\delta^{\theta}_{kj,n}, n \in \{0, .., 5\}$ and the continuous voltage variable V^{θ}_k

are linearized (3.2) using McCormick linearization [78]. The required upper and lower limits of the continuous variable are set as the voltage limits $(\bar{V}^l, \bar{V}^u)$. The same linearization approach is used henceforth to linearize products of binary and continuous variables.

$$\bar{V}^l \delta^{\theta}_{kj,n} \leq x^{\theta}_{kj,n} \leq \bar{V}^u \delta^{\theta}_{kj,n}, \text{ where } x^{\theta}_{kj,n} = \delta^{\theta}_{kj,n} V^{\theta}_k$$
$$V^{\theta}_k - (1 - \delta^{\theta}_{kj,n})\bar{V}^u \leq x^{\theta}_{kj,n} \leq V^{\theta}_k - (1 - \delta^{\theta}_{kj,n})\bar{V}^l \quad (3.2)$$

Maximum allowable tap positions are restricted to 33 using (3.3). For gang-operated AVRs, taps on all three phases are constrained to be equal by adding $\delta^{a}_{kj,n} = \delta^{b}_{kj,n} = \delta^{c}_{kj,n}$.

$$\sum_{n=0}^{5} \delta^{\theta}_{kj,n} (2)^n \leq 32, \; kj \in \mathcal{E}_R \quad (3.3)$$

The state of a controllable capacitor bank $\delta^{\theta}_{c,i}, i \in \mathcal{C}_c$ is included in the reactive power flow expression of the *DistFlow* model as shown in (3.4).

$$\sum_{h:h\to i} Q^{\theta}_{hi} = \sum_{j:i\to j} Q^{\theta}_{ij} + Q^{L,\theta}_i + Q^{G,\theta}_i + \delta^{\theta}_{c,i} \bar{Q}^{C,\theta}_i, \; \forall i \in \mathcal{C}_c \quad (3.4)$$

Upon solving the MILP dispatch or restoration algorithm after including constraints (3.1)-(3.4), the optimal AVR tap positions $\hat{a}^{\theta}_{kj} = 0.9 + 0.00625 \sum_{n=0}^{5} \delta^{\theta}_{kj,n} (2)^n, \; kj \in \mathcal{E}_R$ and optimal capacitor banks states $\hat{\delta}^{\theta}_{c,i}, i \in \mathcal{C}_c$ are obtained. If AVRs and capacitor banks have remote control capabilities, then these optimal states can be directly communicated to them. This, however, is not true for most rural and semi-urban distribution feeders and microgrids. The optimal control approach proposed in this chapter generates optimal DER dispatches which indirectly influence the automatic controllers of the AVRs and capacitor banks to move to these optimal states.

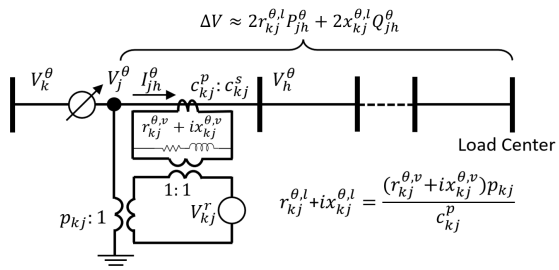

Figure 3.2: Line drop compensation in AVRs

3.1.2 Line Drop Compensation

AVRs use a line drop compensator (LDC) circuit to estimate the voltage at their load center [28]. The parameters c_{kj}^{p}, c_{kj}^{s}, p_{kj}, $r_{kj}^{\theta,v}$ and , $x_{kj}^{\theta,v}$ of the LDC of any AVR connected between nodes k and $j, kj \in \mathcal{E}_R$ are known. Using these pre-determined settings, the LDC estimates the voltage at its load center by measuring its terminal voltage and current using (3.5) as shown in Fig. 3.2.

$$V_{kj}^{r,\theta} = V_j^{\theta}/p_{kj} - I_{jh}^{\theta}c_{kj}^{s} \times (r_{kj}^{\theta,v} + ix_{kj}^{\theta,v})/c_{kj}^{p} \quad (3.5)$$

LDC sends commands to change taps if $V_{kj}^{r,\theta}$ falls outside $V_{kj}^{\theta,l} \pm D_{kj}^{\theta,l}/2$. If $V_{kj}^{r,\theta} < (V_{kj}^{\theta,l} - D_{kj}^{\theta,l}/2)$, then taps are increased by rounding a_{kj}^{θ} to the nearest integer (3.6).

$$a_{kj}^{\theta} = (V_{kj}^{\theta,l} - D_{kj}^{\theta,l}/2 - V_{kj}^{r,\theta})/0.00625 \quad (3.6)$$

Similarly, if $V_{kj}^{r,\theta} > (V_{kj}^{\theta,l} + D_{kj}^{\theta,l}/2)$, then LDC commands the AVR taps to be decreased and a_{kj}^{θ} is given by (3.7).

$$a_{kj}^{\theta} = (V_{kj}^{r,\theta} - V_{kj}^{\theta,l} - D_{kj}^{\theta,l}/2)/0.00625 \quad (3.7)$$

This operation principle of LDC's has been used here to influence them to command their AVRs to move to the optimal tap positions.

3.1.3 Linearizing AVR Load Center Voltage Estimation

To be able to indirectly influence the LDC, it is important to add (3.5) as a constraint. Upon conversion to per unit quantities, the LDC estimates the voltage drop to the load center as $I^{\theta}_{jh} \times (r^{\theta,v}_{kj} + ix^{\theta,v}_{kj})$. However, current is not a variable in linearized power flow models such as the *DistFlow* model. Including current by using $I^{\theta}_{jh} = \frac{(P^{\theta}_{jh}+iQ^{\theta}_{jh})^*}{(V^{\theta}_{j})^*}$ and using the complex impedance will introduce non-linearities. Power flow models which include current as a variable [79] have also been used in restoration algorithms but lead to a non-linear and non-convex formulation which must then be simplified [80]. The *DistFlow* model is commonly used in restoration algorithms [43] as this model is sufficiently accurate for grid optimization tasks [81] and is easy to scale [82].

A closer examination of the voltage drop expression of the linearized *DistFlow* model between any two nodes j and h shows that it approximates the voltage drop across the line using (3.8).

$$\Delta V^{\theta}_{jh} = I^{\theta}_{jh} \times (r^{\theta}_{jh} + ix^{\theta}_{jh}) \approx P^{\theta}_{jh} r^{\theta}_{jh} + Q^{\theta}_{jh} x^{\theta}_{jh} \tag{3.8}$$

The same can be used to approximate the voltage drop till the AVR's load center after converting to per unit quantities using (3.9).

$$I^{\theta}_{jh} \times (r^{\theta,v}_{kj} + ix^{\theta,v}_{kj}) \approx P^{\theta}_{jh} r^{\theta,l}_{kj} + Q^{\theta}_{jh} x^{\theta,l}_{kj} \tag{3.9}$$

Here $r^{\theta,l}_{kj} + ix^{\theta,l}_{kj} = (r^{\theta,v}_{kj} + ix^{\theta,v}_{kj}) \times p_{kj}/c^{p}_{kj}$ represents the LDC's estimated line impedance till the load center. Thus, the voltage at the load center can be estimated to be (3.10).

$$V^{r,\theta}_{kj} = V^{\theta}_{j} - P^{\theta}_{jh} r^{\theta,l}_{kj} - Q^{\theta}_{jh} x^{\theta,l}_{kj} = \mathcal{T}_1 \tag{3.10}$$

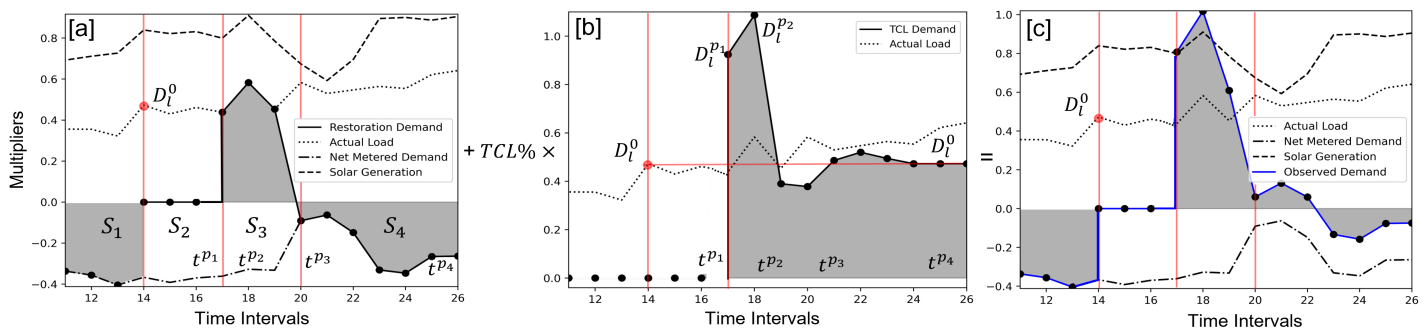

Figure 3.3: [a] NM demand stages during restoration; [b] demand increase due to CLPU; [c] proposed NM load demand model (CLPU + NM demand stages)

3.1.4 Constraints to Influence AVRs to Move to Optimal Tap Positions

While LDC determines tap position based on estimated load center voltage, the objective here is the opposite. The optimal tap position is available and the LDC must be made to estimate the corresponding load center voltage. This is achieved using the constraints developed here which generate DER dispatches that influence the terminal voltage and line flow of AVRs. These terminal quantities are such that the LDC will command its AVR to move to the optimal tap position. Thus, when $\hat{a}^{\theta}_{kj}$ is evaluated to be higher than the neutral tap position by the MILP dispatch or restoration algorithm, the voltage at the load center should be $V^{r,\theta}_{kj} = V^{\theta,l}_{kj} - D^{\theta,l}_{kj}/2 - \hat{a}^{\theta}_{kj} \times 0.00625$ using (6), in order to make the LDC to command the AVR to move to $\hat{a}^{\theta}_{kj}$. Here $V^{r,\theta}_{kj}$ is replaced with $\mathcal{T}_1$ and $\hat{a}^{\theta}_{kj} \times 0.00625$ is replaced with $\mathcal{T}_2 = ((0.9 + 0.00625 \sum_{n=0}^{5} \delta^{\theta}_{kj,n}(2)^n) - 1)$. Thus, the equality constraint to be added to move an AVR to higher tap positions is given by (3.11).

$$\mathcal{T}_1 = V^{\theta,l}_{kj} - D^{\theta,l}_{kj}/2 - \mathcal{T}_2 \tag{3.11}$$

Similarly when $\hat{a}^{\theta}_{kj}$ is evaluated to be lower than the neutral tap tap position, the voltage at

the load center should be $V_{kj}^{r,\theta} = V_{kj}^{\theta,l} + D_{kj}^{\theta,l}/2 + \hat{a}_{kj}^{\theta} \times 0.00625$. Thus, the equality constraint to be added to move an AVR to lower tap positions is given by (3.12).

$$\mathcal{T}_1 = V_{kj}^{\theta,l} + D_{kj}^{\theta,l}/2 - \mathcal{T}_2 \tag{3.12}$$

3.1.5 Automating Constraint Selection

Based on whether AVR taps have to be increased (3.11) or decreased (3.12), a different constraint needs to be applied. Since tap positions $\hat{a}_{kj}^{\theta}$ are decision variables, an approach is needed to automatically select the correct constraint. It is achieved here by making use of the 6-bit binary code used for determining the optimal tap positions in (1). The code 010000 represents the neutral tap position. Thus, the fifth binary variable $\delta_{kj,4}^{\theta}, kj \in \mathcal{E}_R$ must be 1 for all positive tap positions. The only exception is the $+16^{\text{th}}$ tap position for which $\delta_{kj,4}^{\theta} = 0$ but $\delta_{kj,5}^{\theta} = 1$. Thus, to select the correct constraint automatically, (3.11) and (3.12) are replaced with (3.13)-(3.15), where M is a large number. Extremely large M values can lead to numerical instability and $M = 1$ was found to be sufficient for these constraints. This is because these constraints are in $p.u.$ and are trying to determine the tap position which minimizes the difference from the estimated load center voltage given by $\mathcal{T}_1$. Thus, the value of the expression should be significantly less than one.

$$-M(1 - \delta_{kj,4}^{\theta}) \leq \mathcal{T}_1 - V_{kj}^{\theta,l} + D_{kj}^{\theta,l}/2 + \mathcal{T}_2 \leq M(1 - \delta_{kj,4}^{\theta}) \tag{3.13}$$

$$-M(1 - \delta_{kj,5}^{\theta}) \leq \mathcal{T}_1 - V_{kj}^{\theta,l} + D_{kj}^{\theta,l}/2 + \mathcal{T}_2 \leq M(1 - \delta_{kj,5}^{\theta}) \tag{3.14}$$

$$-M \sum_{n=4}^{5} \delta_{kj,n}^{\theta} \leq \mathcal{T}_1 - V_{kj}^{\theta,l} - D_{kj}^{\theta,l}/2 + \mathcal{T}_2 \leq M \sum_{n=4}^{5} \delta_{kj,n}^{\theta} \tag{3.15}$$

3.1.6 Optimal Control of Automatic Capacitor Banks

Capacitor banks switch ON when their PCC voltage falls below a threshold ($V_i^{\theta} < V_i^{\theta,on}, i \in \mathcal{C}_c$) and turn OFF when their PCC voltage exceeds a threshold ($V_i^{\theta} > V_i^{\theta,of}, i \in \mathcal{C}_c$). Based on the optimally evaluated state of the capacitor bank $\hat{\delta}_{c,i}^{\theta}, i \in \mathcal{C}_c$, constraints (3.16) and (3.17) ensure turn ON or OFF of the capacitor bank.

$$-M(1-\delta_{c,i}^{\theta}) \leq V_i^{\theta} - V_i^{\theta,on} \leq M(1-\delta_{c,i}^{\theta}) \tag{3.16}$$

$$-M\delta_{c,i}^{\theta} \leq V_i^{\theta} - V_i^{\theta,of} \leq M\delta_{c,i}^{\theta} \tag{3.17}$$

3.2 NM Load Model

Demand generation imbalance due to inaccurate demand forecasts can impact the stability of a microgrid during service restoration. It is shown here that NM load demand can vary significantly during restoration from their historical profiles. For any NM load, the net demand ($p_{i,t}^{n}$) at any time t is available via AMI and is related to the actual demand ($p_{i,t}^{d}$) and solar generation ($p_{i,t}^{g}$) by (3.18).

$$p_{i,t}^{n} = p_{i,t}^{d} - p_{i,t}^{g} \tag{3.18}$$

It will be shown here that the disaggregation of this NM time series into actual demand and generation time series is essential for including CLPU phenomenon and demand stages during microgrid restoration. The main contribution is the development of a generalized time dependent NM load demand model, which completely describes the behavior of NM loads during microgrid restoration in accordance with the IEEE 1547 standard and incorporates

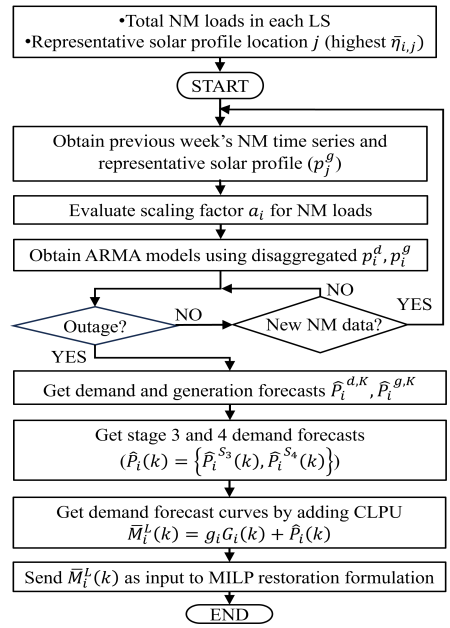

Figure 3.4: Flow chart summarizing the approach for creating the proposed NM demand model.

the CLPU phenomenon.

3.2.1 CLPU Phenomenon and NM loads

In the CLPU model here [50], as shown in Fig. 3.3[b], the TCL demand is $D_l^{p_1}$ when it is restored at time point t^{p_1}. The demand then increases linearly to peak demand $D_l^{p_2}$ at t^{p_2}, as more TCLs turn ON. $D_l^{p_1} < D_l^{p_2}$ as diversity is not completely lost due to the short outage duration. The demand then decreases gradually to the pre-outage demand level D_l^0 and stays there after t^{p_4} as TCL diversity is restored. The behavior between time points t^{p_2} and t^{p_4} can be modeled using a polynomial function $h(y)$. Using the DEM model as the basis, the complete CLPU curve is modeled using (3.19)-(3.21), for any time $k \in \mathcal{K}$ with a Δt time step between restoration intervals [50].

$$G_l(k) = [D_l^{p_1} + \frac{D_l^{p_2} - D_l^{p_1}}{t^{p_2} - t^{p_1}}(k-1)\Delta t](1 - x(R_{l,k}^1))$$

$$+h(R^1_{l,k})x(R^1_{l,k})(1-x(R^2_{l,k}))+x(R^2_{l,k})D^0_l \tag{3.19}$$

where $x(j), R^1_{l,k}$ and $R^2_{l,k}$ are defined as,

$$x(j)=\begin{cases}1 & ,\text{if } j>0\\ 0 & ,\text{if } j\leq 0\end{cases} \tag{3.20}$$

$$R^1_{l,k}=(k-1)\Delta t-(t^{p_2}-t^{p_1}),\ R^2_{l,k}=(k-1)\Delta t-(t^{p_4}-t^{p_1}) \tag{3.21}$$

Equation (3.19) shows that this CLPU model is a function of the pre-outage demand D^0_l. The challenge however with NM loads is that only the net demand is available, whereas D^0_l is a function of the actual demand. This requires disaggregation of NM demand time series into actual demand and solar generation time series.

3.2.2 Microgrid Restoration Stages with NM Loads

The demand observed for an NM load during the restoration process, as shown in Fig. 3.3[a], can be divided into four stages. Prior to the outage, in stage S_1, the net demand is available. In stage S_2, the load is de-energized. S_2 continues until the NM load is energized by the restoration algorithm. In stage S_3, when the NM load is restored, the actual demand is observed instead of net demand. This is because the PV systems stay offline due to their default *'enter service delay'* as per IEEE 1547-2018 [47]. As per IEEE 1547, by default any type of DER after being de-energized is allowed to enter service only when microgrid voltages and frequency are within allowable thresholds during normal or post-restoration conditions [47]. The default delay is 5 minutes and can be up to 16 minutes. Finally, in stage S_4, PV systems come back online after their 'enter service delay' and the NM demand is observed.

Stage S_3 is critical, as sudden energization of loads create transients. Inaccurate dispatch of DERs based on net demand forecasts can lead to frequency instability [26] and restoration failure. This further necessitates disaggregation of NM time series.

NM load demand will thus vary significantly during each time interval after restoration until diversity is restored. Instead of the expected net demand, the actual demand will be observed initially as PV systems are offline. This demand will be further increased due to the CLPU phenomenon. Eventually as PV systems will come back online, the summation of net demand and demand changes due to CLPU will be observed. The approach for obtaining this combined demand curve is described next and has been summarized in the flow chart shown in Fig. 3.4.

3.2.3 Disaggregation of NM Time Series

Loads in a microgrid cannot be restored individually as all loads are not connected via remotely operable switches. As shown in Fig. 3.6, all the NM loads downstream of a switch, referred to as a load section (LS), are energized together [49],[83]. Given NM time series of all the loads in a LS, and the forecast for either their solar generation or actual demand, the other can be obtained by taking the difference. The problem then is to estimate both solar generation and actual demand of each NM load in a LS given only their NM time series.

In this chapter, a systematic approach is proposed for placing a solar generation measurement meter based on correlation in historical NM time series data, for disaggregating the solar generation and actual demand of each NM load. The correlation coefficient $\eta_{i,j}$ between any i^{th} and j^{th} NM loads can be found by taking the ratio of the covariance $c_{i,j}$ with the standard deviations s_i and s_j of their historical NM time series of length N. $\tilde{p}_i^n, \tilde{p}_j^n$ are the arithmetic

means of the historical NM time series of loads i and j respectively.

$$\eta_{i,j} = \frac{c_{i,j}}{s_i s_j}, \text{ where } c_{i,j} = \frac{\sum_{k=1}^{N}(p_{i,k}^n - \tilde{p}_i^n)(p_{j,k}^n - \tilde{p}_j^n)}{N-1} \tag{3.22}$$

Assuming perfect correlation between the NM time series of these customers, i.e., $\eta_{i,j} = 1$, these two random variables can be shown to be linearly related with each other $p_i^n = a_i p_j^n, a_i \in \mathbb{R}$ as proved in Appendix A. Then using (3.18),

$$p_i^n = a_i p_j^n \implies p_i^d - p_i^g = a_i p_j^d - a_i p_j^g \tag{3.23}$$

However, $\eta_{i,j} < 1$, primarily due to the different demand patterns of NM loads in a LS. As described in Appendix A, the solar generation profiles are more correlated in geographically small load sections due to similar cloud patterns. Thus, most of the correlation observed in NM time series would be due to the correlation in solar generation profiles. A solar generation meter can be placed at the NM load showing the highest average correlation in historical NM time series data with all other loads in the LS. The solar profile of this j^{th} NM load p_j^g can serve as the representative solar profile for all the NM loads in the LS. A scaling factor a_i is obtained for each NM load in the LS to account for different kVA ratings and seasonal factors such as soiling of PV panels. a_i is obtained using the historical NM time series of length N, by taking the partial derivative of the sum of squared errors with respect to a_i (3.24). Since most of the correlation in NM time series is expected to be because of solar generation, the a_i parameters obtained using only the NM time series data should be accurate for estimating solar generation profile of each customer using p_j^g. Results to validate the effectiveness of this approach in estimating solar generation profiles are shown

in Appendix A.2.

$$\frac{\partial \sum_{k=1}^{N}(p_{i,k}^{n} - a_i p_{j,k}^{n})^2}{\partial a_i} = 0 \Rightarrow a_i = \frac{\sum_{k=1}^{N} p_{j,k}^{n} p_{i,k}^{n}}{\sum_{k=1}^{N}(p_{j,k}^{n})^2} \quad (3.24)$$

Using the scaling factor a_i, the disaggregated solar generation of each NM load is $p_i^g = a_i p_j^g$ and the disaggregated actual demand is $p_i^d = p_i^n + a_i p_j^g$. The disaggregated solar generation and actual demand profiles of the previous week can be used to obtain the order and parameters of the auto regressive moving average (ARMA) model [84] for generating demand forecasts.

During an outage, the obtained ARMA model and a_i can be used to obtain the demand during all four restoration stages $\hat{P}_i(k), k \in \mathcal{K}$ for any i^{th} NM load in the LS. In the pre-outage stage S_1 as shown in Fig. 3.3[a], the NM time series P_i^{n,S_1} and the representative solar generation time series P_j^{g,S_1} of length K^{S_1} are available. These are used to obtain the disaggregated solar generation profile $P_i^{g,S_1} = a_i P_j^{g,S_1}$ and the actual demand profile $P_i^{d,S_1} = P_i^{n,S_1} + a_i P_j^{g,S_1}$. The ARMA model can then be used to obtain solar generation $\hat{P}_i^{g,K}$ and actual demand forecasts $\hat{P}_i^{d,K}$ for K future restoration time steps.

Using these forecasts, the forecasted demand in stage S_2 is $\hat{P}_i^{S_2}(k) = 0, k \in \{1, .., K^{S_2}\}$ where K^{S_2} is the time interval when the LS is energized by the restoration algorithm. The forecasted demand in stage S_3 is the actual demand forecast as PVs are offline (3.25).

$$\hat{P}_i^{S_3}(k) = \hat{P}_i^{d,K}(k), k \in \{K^{S_2} + 1, .., K^{S_3}\} \quad (3.25)$$

The duration of stage S_3, $K^{S_3} - K^{S_2}$ is equal to the *'enter service delay'* as per IEEE 1547-2018. Finally, the forecasted demand in stage S_4 will be the net demand as PV systems are

back online (3.26).

$$\hat{P}_i^{S_4}(k) = \hat{P}_i^{d,K}(k) - \hat{P}_i^{g,K}(k), k \in \{K^{S_3}+1,..,K\} \tag{3.26}$$

The forecasted demand during the K restoration steps is given by (3.27).

$$\hat{P}_i(k) = \{\hat{P}_i^{S_3}(k), \hat{P}_i^{S_4}(k)\}, k \in \mathcal{K} \tag{3.27}$$

3.2.4 Generalized Time Dependent NM Load Demand Model

Using the disaggregated pre-outage actual demand time series P_l^{d,S_1}, the pre-outage demand D_l^0 required for determining the CLPU curve $G_l(k), k \in \mathcal{K}$ for any l^{th} NM load can be obtained as $D_l^0 = P_l^{d,S_1}(K^{S_1})$. The generalized time dependent NM load demand model for the lth NM load can now be obtained by summing the forecasted demand during the K restoration steps $\hat{P}_l(k)$ and the CLPU curve $G_l(k)$ scaled by TCL percentage g_l, $\bar{M}_l^L(k) = g_l G_l(k) + \hat{P}_l(k)$ as shown in (3.28), (3.29).

$$\bar{M}_l^L(k) = g_l \times \Bigg([D_l^{p_1} + \frac{D_l^{p_2} - D_l^{p_1}}{t^{p_2} - t^{p_1}}(k-1)\Delta t](1 - x(R_{l,k}^1))$$

$$+h(R_{l,k}^1)x(R_{l,k}^1)(1 - x(R_{l,k}^2)) + x(R_{l,k}^2)P_l^{d,S_1}(K^{S_1})\Bigg) +$$

$$\Bigg(\hat{P}_l^{d,K}(k)(1 - x(R_{l,k}^3)) + (\hat{P}_l^{d,K}(k) - \hat{P}_l^{g,K}(k))x(R_{l,k}^3)\Bigg) \tag{3.28}$$

where $x(j)$, $R^1_{l,k}$ and $R^2_{l,k}$ are given by (3.20) and (3.21) and $R^3_{l,k}$ is given by (3.29).

$$R^3_{l,k} = k\Delta t - (t^{p_3} - t^{p_1}) \tag{3.29}$$

It should be noted that this model is valid irrespective of whether t^{p_3} is larger or smaller than t^{p_2}. These demand curves $\bar{M}^L_l(k)$ as shown in Fig. 3.3[c], are obtained for all NM loads before running the microgrid restoration algorithm. Constraints to automatically select the correct demand from the curve based on when a NM load gets energized are presented in section IV.

3.3 Sequential Microgrid Restoration Algorithm

The algorithm presented here incorporates the proposed voltage regulating device constraints and NM load demand curves within sequential MILP based optimal microgrid restoration algorithms [85] and [49]. By adding constraints (3.1)-(3.4) and (3.13)-(3.17) to an MILP based dispatch or restoration algorithm, the optimal taps $\hat{a}^{\theta}_{kj}$ and capacitor bank states $\hat{\delta}^{\theta}_{c,i}, i \in \mathcal{C}_c$, required to optimize the objective function are determined. Simultaneously, optimal DER dispatches are obtained which cause such voltages and power flows at the PCC of each AVR, such that its LDC estimates a load center voltage which will necessitate moving taps to $\hat{a}^{\theta}_{kj}$. Optimal DER dispatches will also create desired PCC voltages for capacitor banks to make them switch to the optimal state. While this proposed approach is sufficient for optimally controlling automatic AVRs and capacitor banks for optimal dispatch applications, additional points need to be considered while integrating it with MILP based optimal sequential microgrid restoration algorithms.

A. Pre-outage State Estimation of Voltage Regulation Devices:

The time step when a voltage regulation device will be restored is determined by the algorithm. At this first energization interval their pre-outage states need to be considered while dispatching the DERs. This is because their taps are operated using a motor and will thus stay locked in their pre-outage state during an outage. Moreover, due to the default time delays of their automatic controllers, these devices cannot be optimally controlled from the first energization interval itself. An MILP based approach is proposed here to utilize the limited line flow and voltage measurements from residential AMI meters to estimate pre-outage states of these devices.

Objective function: The objective function minimizes the differences between the limited pre-outage measurements and their corresponding variables (3.30). The least absolute value estimator which is accurate for state estimation has been used [83].

$$min \sum_{\theta \in \{a,b,c\}} (\sum_{ij \in \mathcal{E}_M} |\bar{P}_{ij}^{\theta} - P_{ij}^{\theta}| + \sum_{ij \in \mathcal{E}_M} |\bar{Q}_{ij}^{\theta} - Q_{ij}^{\theta}| +$$

$$\sum_{i \in \mathcal{B}_M} |\bar{V}_i^{\theta} - V_i^{\theta}|), \ \mathcal{E}_M \subseteq \mathcal{E}, \ \mathcal{B}_M \subseteq \mathcal{B} \tag{3.30}$$

The non-linear absolute value function needs to be linearized. The voltage term in (3.30) for instance is linearized by adding (3.31), where $v_i = |\bar{V}_i^{\theta} - V_i^{\theta}|$.

$$\bar{V}_i^{\theta} - V_i^{\theta} \leq v_i, \text{ and } -(\bar{V}_i^{\theta} - V_i^{\theta}) \leq v_i \tag{3.31}$$

Constraints on voltage regulation devices: Capacitor banks and AVRs are included using (3.1)-(3.4). However both the capacitor bank's state $\delta_{c,i}$ and capacity $q_{c,i}^{\theta}$, in case the capacitor bank has steps, are included as variables in (3.4).

Power flow constraints: The real and reactive line flows for the edges and nodal voltages

for the nodes without voltage regulation devices are incorporated in the linearized *DistFlow* model [76]. These constraints (3.32) also help in defining the microgrid topology.

$$\sum_{h:h\to i} P_{hi}^{\theta} = \sum_{j:i\to j} P_{ij}^{\theta} + \bar{P}_i^{L,\theta} + \bar{P}_i^{G,\theta}, \forall i \in \mathcal{B}$$

$$\sum_{h:h\to i} Q_{hi}^{\theta} = \sum_{j:i\to j} Q_{ij}^{\theta} + \bar{Q}_i^{L,\theta} + \bar{Q}_i^{G,\theta},\ \forall i \in \mathcal{B}\backslash\mathcal{C}$$

$$\sum_{h:h\to i} Q_{hi}^{\theta} = \sum_{j:i\to j} Q_{ij}^{\theta} + \bar{Q}_i^{L,\theta} + \bar{Q}_i^{G,\theta} + \bar{Q}_i^{C,\theta},\ \forall i \in \mathcal{C}\backslash\mathcal{C}_c$$

$$V_i^{\theta} = V_j^{\theta} + \bar{r}_{ij}^{\theta} P_{ij}^{\theta} + \bar{x}_{ij}^{\theta} Q_{ij}^{\theta},\ \forall ij \in \mathcal{E}\backslash\mathcal{E}_R \tag{3.32}$$

Upon solving the MILP formulation, the estimated pre-outage tap positions of each AVR $\bar{a}_{ij}^{\theta} = 0.9 + 0.00625\sum_{n=0}^{5}\delta_{ij,n}^{\theta}(2)^n,\ ij \in \mathcal{E}_R$, and the estimated pre-outage states and kVAR values of each controllable capacitor bank $\bar{\delta}_{c,i}^{\theta}, \bar{q}_{c,i}^{\theta}, i \in \mathcal{C}_c$ are obtained. This step is completed prior to running the restoration algorithm and the bars on these estimates indicate that these will be used as parameters in the sequential microgrid restoration algorithm. Once the pre-outage state estimates and demand curves (3.28) are available for all NM loads, the restoration algorithm can be solved. The proposed MILP based formulation has been summarized in the flow chart shown in Fig. 3.5.

B. Objective Function for Restoration Algorithm:

The objective function (3.33) aims to maximize the total energy restored over the K restoration time steps. Critical loads can be assigned a weight ($\bar{c}_i^{L,\theta}$) to ensure these are restored

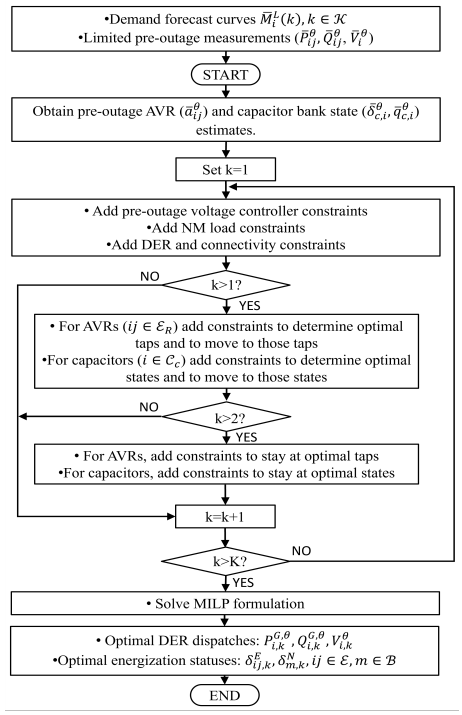

Figure 3.5: Flow chart summarizing the proposed MILP based sequential microgrid restoration algorithm.

earlier. As described in appendix A.3, the loads within a load section are restored together. Thus, if there are more critical loads in a load section its weighting factor will be higher and will be restored earlier. All loads have the same priority in the case study to highlight the impact of NM demand curves and automatic voltage controllers.

$$max(\sum_{k=1}^{K}\sum_{i=1}^{N}\sum_{\theta\in\{a,b,c\}} \bar{c}_i^{L,\theta} \times P_{i,k}^{L,\theta} \times \Delta\bar{t}) \tag{3.33}$$

C. AVR and Capacitor Bank Constraints:

After a voltage regulation device has been restored at $t = t_r \in \mathcal{K}$, while considering its estimated pre-outage state for dispatching DERs, it must then be optimally controlled from $t = t_r + 1$ onwards using the approach presented in section 3.1. An approach is needed to

ensure that estimated pre-outage states are used only in the first energization interval and states are controlled at their optimal positions from the second interval onwards. Finally, from the third interval onwards undesirable changes from the optimal tap positions and states of capacitor banks should be prevented. These logic propositions need to be integrated within the sequential microgrid service restoration algorithm because the restoration time interval itself is a decision variable. This is achieved here by building upon the big-M method. The pre-outage state for AVRs ($\bar{a}^{\theta}_{ij}, ij \in \mathcal{E}_R$) is inlcuded using constraint (3.34) for all $k \in \mathcal{K}$. The term ($\sum_{p=1}^{k} \delta^{E}_{ij,p} - 1$) is zero only at the first energization interval.

$$-M(\sum_{p=1}^{k} \delta^{E}_{ij,p} - 1) \leq V^{\theta}_{j,k} - \bar{a}^{\theta}_{ij} V^{\theta}_{i,k} \leq M(\sum_{p=1}^{k} \delta^{E}_{ij,p} - 1) \quad (3.34)$$

Pre-outage states of capacitor banks ($\bar{\delta}^{\theta}_{c,i}, \bar{q}^{\theta}_{c,i}, i \in \mathcal{C}_c$) are included using (3.35), where $\mathcal{T}_3 = (\sum_{p=1}^{k} \delta^{N}_{i,p} - 1), \forall k \in \mathcal{K}$.

$$\sum_{h:h\to i} Q^{\theta}_{hi,k} - (\sum_{j:i\to j} Q^{\theta}_{ij,k} + Q^{L,\theta}_{i,k} + Q^{G,\theta}_{i,k} + \bar{\delta}^{\theta}_{c,i}\bar{q}^{\theta}_{c,i}) \leq M\mathcal{T}_3$$

$$\sum_{h:h\to i} Q^{\theta}_{hi,k} - (\sum_{j:i\to j} Q^{\theta}_{ij,k} + Q^{L,\theta}_{i,k} + Q^{G,\theta}_{i,k} + \bar{\delta}^{\theta}_{c,i}\bar{q}^{\theta}_{c,i}) \geq -M\mathcal{T}_3 \quad (3.35)$$

The nodes connected to the AVRs and capacitor banks are not disconnected after being energized. This is ensured by using (3.36) and (3.37). In fact these constraints ensure that all edges and nodes stay energized after being restored.

$$\delta^{E}_{ij,k} - \delta^{E}_{ij,k-1} \geq 0, \ k > 1, \ \forall (ij) \in \mathcal{E} \quad (3.36)$$

$$\delta^{N}_{i,k} - \delta^{N}_{i,k-1} \geq 0, \ k > 1, \ \forall i \in \mathcal{B} \quad (3.37)$$

From the second interval onwards, the optimal tap positions of AVRs ($\forall ij \in \mathcal{E}_R, k > 1$) are evaluated using (3.38)-(3.39). For 3-phase AVRs, taps on all three phases are constrained to be equal by adding $\delta^a_{ij,n,k} = \delta^b_{ij,n,k} = \delta^c_{ij,n,k}$. The AVR PCC voltages and line flows are controlled using constraints (3.40)-(3.42) to move taps to their optimal positions. The term $\mathcal{T}_4 = (2\delta^E_{ij,k-1} - 1 - \sum_{p=1}^{k} \delta^E_{ij,p} + \sum_{p=1}^{k-1} \delta^E_{ij,p})$ ensures that constraints (3.38)-(3.42) are satisfied at equality only from the second AVR energization interval onwards. Here $\mathcal{T}_5 = (1 - \delta^\theta_{ij,4,k})$, $\mathcal{T}_6 = (1 - \delta^\theta_{ij,5,k})$ and $\mathcal{T}_7 = (\sum_{n=4}^{5} \delta^\theta_{ij,n,k})$ as described in section 3.1.

$$-M\mathcal{T}_4 \leq V^\theta_{j,k} - V^\theta_{i,k}(0.9 + 0.00625 \sum_{n=0}^{5} \delta^\theta_{ij,n,k}(2)^n) \leq M\mathcal{T}_4 \tag{3.38}$$

$$-M\mathcal{T}_4 \leq \sum_{n=0}^{5} \delta^\theta_{ij,n,k}(2)^n \leq 32 + M\mathcal{T}_4 \tag{3.39}$$

$$-M(\mathcal{T}_4 + \mathcal{T}_5) \leq \mathcal{T}_1 - V^{\theta,l}_{ij} + D^{\theta,l}_{ij}/2 + \mathcal{T}_2 \leq M(\mathcal{T}_4 + \mathcal{T}_5) \tag{3.40}$$

$$-M(\mathcal{T}_4 + \mathcal{T}_6) \leq \mathcal{T}_1 - V^{\theta,l}_{ij} + D^{\theta,l}_{ij}/2 + \mathcal{T}_2 \leq M(\mathcal{T}_4 + \mathcal{T}_6) \tag{3.41}$$

$$-M(\mathcal{T}_4 + \mathcal{T}_7) \leq \mathcal{T}_1 - V^{\theta,l}_{ij} - D^{\theta,l}_{ij}/2 + \mathcal{T}_2 \leq M(\mathcal{T}_4 + \mathcal{T}_7) \tag{3.42}$$

Once the AVRs have been moved to their optimal tap positions, these are maintained in those positions for the remaining restoration intervals ($\forall ij \in \mathcal{E}_R, k > 2$) to prevent undesirable tap changes using constraint (3.43), where $\mathcal{T}_8 = (3\delta^E_{ij,k-2} - 1 - \sum_{p=1}^{k} \delta^E_{ij,p} + \sum_{p=1}^{k-2} \delta^E_{ij,p})$.

$$-M\mathcal{T}_8 \leq \delta_{ij,n,k} - \delta_{ij,n,k-1} \leq M\mathcal{T}_8, \ \forall n \in \{0, .., 5\} \tag{3.43}$$

For all capacitor banks the optimal state (ON or OFF) is determined using (3.44), where $\mathcal{T}_9 = (\sum_{p=1}^{k} \delta^N_{i,p} - 2)$. As described in section 3.1, the capacitor bank is controlled to reach

the optimal state using (3.45), (3.46).

$$-M\mathcal{T}_9 \leq \sum_{h:h\to i} Q^{\theta}_{hi,k} - (\sum_{j:i\to j} Q^{\theta}_{ij,k} + Q^{L,\theta}_{i,k} + Q^{G,\theta}_{i,k} + \delta^{c,\theta}_{i,k}\bar{Q}^{C,\theta}_{i}) \leq M\mathcal{T}_9,\ \forall i \in \mathcal{C}_c, k > 1 \quad (3.44)$$

$$-M(\mathcal{T}_9 + 1 - \delta^{c,\theta}_{i,k}) \leq V^{\theta}_{i,k} - V^{\theta,on}_{i} \leq M(\mathcal{T}_9 + 1 - \delta^{c,\theta}_{i,k}) \quad (3.45)$$

$$-M(\mathcal{T}_9 + \delta^{c,\theta}_{i,k}) \leq V^{\theta}_{i,k} - V^{\theta,of}_{i} \leq M(\mathcal{T}_9 + \delta^{c,\theta}_{i,k}) \quad (3.46)$$

It should be noted that unlike AVRs where constraints (3.38)-(3.42) must be applied continuously to maintain taps in their optimal positions, for capacitor banks constraints (3.44)-(3.46) only have to be applied at their second restoration interval. Thereafter capacitor banks' nodal voltages are maintained within their dead bands using (3.47), where $\mathcal{T}_{10} = (3\delta^{N}_{i,k-2} - 1 - \sum_{p=1}^{k}\delta^{N}_{i,p} + \sum_{p=1}^{k-2}\delta^{N}_{i,p})$. This is because capacitor banks tend to have larger dead bands and maintaining their PCC voltage continuously beyond their ON or OFF thresholds can lead to infeasibility.

$$-M\mathcal{T}_{10} + \bar{V}^{\theta,on}_{i} \leq V^{\theta}_{i,k} \leq \bar{V}^{\theta,of}_{i} + M\mathcal{T}_{10},\ \forall i \in \mathcal{C}_c, k > 2 \quad (3.47)$$

D. NM Load Constraints:

The combined NM and CLPU curves ($\bar{M}^{L,\theta}_{i}$) are generated for each ith NM load using (28) as described in section 3.2, before running the microgrid restoration algorithm. These curves thus act as parameters for the restoration algorithm. However, the point on the demand curve to be selected at each restoration step is determined by the restoration algorithm based on when the NM load is energized. This is achieved using (3.48) which has been adapted from [49] to work with non-monotonically decreasing demand curves as well. Here $\bar{P}^{L,\theta}_{i}, \bar{Q}^{L,\theta}_{i}$

are the rated real and reactive power demands of the NM load.

$$P_{i,k}^{L,\theta} = \bar{P}_i^{L,\theta}(\delta_{i,k}^N \bar{M}_{i,1}^{L,\theta} - \sum_{p=1}^{k} \Delta M_i^{L,\theta}(p)\delta_{i,k-p+1}^N)$$

$$Q_{i,k}^{L,\theta} = \bar{Q}_i^{L,\theta}(\delta_{i,k}^N \bar{M}_{i,1}^{L,\theta} - \sum_{p=1}^{k} \Delta M_i^{L,\theta}(p)\delta_{i,k-p+1}^N)$$

$$\text{where, } \Delta M_i^{L,\theta}(p) = \begin{cases} 0 & \text{, if } p = 1 \\ \bar{M}_{i,p-1}^{L,\theta} - \bar{M}_{i,p}^{L,\theta} & \text{, if } p > 1 \end{cases} \tag{3.48}$$

Linearized power flow constraints such as (3.32) are added for non-voltage regulation device nodes. Additionally, demand generation balance, maximum and minimum generation limits, voltage, and line loading limits are added as constraints. Connectivity and sequencing constraints [85] to ensure the creation of a feasible radial microgrid topology while utilizing the normally open tie-switches are also included. These constraints have been shown in appendix A.3.

E. Algorithmic Complexity:

The proposed sequential microgrid restoration algorithm is formulated as a MILP. MILP is a NP-hard problem and is solved using the branch-and-bound algorithm which divides the problem into several linear programming (LP) sub problems by forming a search tree [86]. The complexity of MILP problems can be enhanced by tightening and compactness [87]. The use of connectivity and sequencing constraints where multiple loads are grouped in load sections as shown in Appendix A.3 and the developed AVR and capacitor bank constraints

help in tightening the problem by reducing the distance between the LP relaxations and the feasible integer solutions. However, adding too many constraints can increase the problem size since the size of each LP increases which increases the search space.

Reducing the problem size by reducing the number of constraints and the number of binary variables can reduce the computational burden, speeding up the search process [88]. Multiple contributions have been made here to reduce the problem size such as by the development of terms $\mathcal{T}_4$ and $\mathcal{T}_8$. For instance, in the absence of $\mathcal{T}_4$, (3.38) will have to be split into two constraints (3.49) and (3.50). Here (3.49) ensures that this constraint is satisfied at equality only from the second energization interval onwards. (3.50) is needed to ensure that this constraint is not applied while $\delta^E_{ij,k} = 0$. Thus, constraints (3.38)-(3.47) are reduced by half for each phase of each AVR at every restoration interval using the proposed approach.

$$-M(\delta^E_{ij,k} - \delta^E_{ij,k-1}) \leq V^\theta_{j,k} - V^\theta_{i,k}(0.9 + 0.00625\sum_{n=0}^{5}\delta^\theta_{ij,n,k}2^n) \leq M(\delta^E_{ij,k} - \delta^E_{ij,k-1}),\ \forall ij \in \mathcal{E}_R, k > 1 \quad (3.49)$$

$$-M(\sum_{p=1}^{k}\delta^E_{ij,p} - 2) \leq V^\theta_{j,k} - V^\theta_{i,k}(0.9 + 0.00625\sum_{n=0}^{5}\delta^\theta_{ij,n,k}2^n) \leq M(\sum_{p=1}^{k}\delta^E_{ij,p} - 2),\ \forall ij \in \mathcal{E}_R, k > 1 \quad (3.50)$$

The number of binary variables is reduced significantly using the 6-bit binary code approach instead of using 33 binary variables for each phase of each AVR at every restoration interval. Using 33 binary variables, constraints (3.38)-(3.43) will change to (3.51)-(3.55). Here $\boldsymbol{t} = [0.9, 0.90625, ..., 1, ..., 1.09375, 1.1]^{33}$ represents the 33 tap position multiplers and a corresponding vector of 33 binary variables $\boldsymbol{a} = [\delta^\theta_{ij,1,k}, \delta^\theta_{ij,2,k}, ..., \delta^\theta_{ij,33,k}]^{33}$. The correspond-

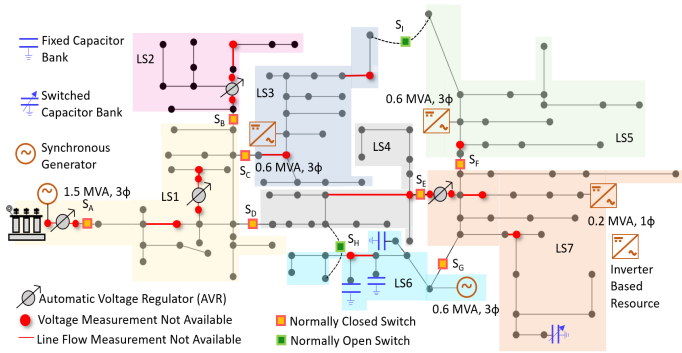

Figure 3.6: Extended IEEE 123-node test feeder in OpenDSS used as a microgrid

ing terms will also have to be updated as follows $\mathcal{T}_2' = (\boldsymbol{a}^T\boldsymbol{t} - 1)$, $\mathcal{T}_5' = \sum_{n=1}^{16} \delta_{ij,n,k}^{\theta}$ and $\mathcal{T}_6' = (1 - \sum_{n=1}^{16} \delta_{ij,n,k}^{\theta})$. (3.52) ensures only one of the 33 taps is selected at a time. Results on complexity enhancement using the proposed algorithm are presented in section V.

$$-M\mathcal{T}_4 \leq V_{j,k}^{\theta} - V_{i,k}^{\theta}\boldsymbol{a}^T\boldsymbol{t} \leq M\mathcal{T}_4 \tag{3.51}$$

$$-M\mathcal{T}_4 \leq \sum_{n=1}^{33} \delta_{ij,n,k}^{\theta} - 1 \leq M\mathcal{T}_4 \tag{3.52}$$

$$-M(\mathcal{T}_4 + \mathcal{T}_5') \leq \mathcal{T}_1 - V_{ij}^{\theta,l} + D_{ij}^{\theta,l}/2 + \mathcal{T}_2' \leq M(\mathcal{T}_4 + \mathcal{T}_5') \tag{3.53}$$

$$-M(\mathcal{T}_4 + \mathcal{T}_6') \leq \mathcal{T}_1 - V_{ij}^{\theta,l} - D_{ij}^{\theta,l}/2 + \mathcal{T}_2' \leq M(\mathcal{T}_4 + \mathcal{T}_6') \tag{3.54}$$

$$-M\mathcal{T}_8 \leq \delta_{ij,n,k} - \delta_{ij,n,k-1} \leq M\mathcal{T}_8,\ \forall n \in \{1,..,33\} \tag{3.55}$$

3.4 Case Study

The proposed method has been validated using the IEEE 123-node distribution system model as a microgrid in OpenDSS. This 3-phase unbalanced non-linear power flow model has detailed models for loads, generators, AVRs with LDCs, capacitor banks and their localized controllers, and other power delivery and conversion equipment. The $\bar{r}_{ij}^{\theta} + j\bar{x}_{ij}^{\theta}$

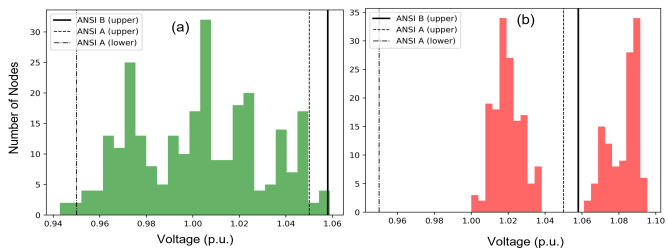

Figure 3.7: Histogram of nodal voltages in IEEE 123-node system when AVR taps (a) are considered, (b) not considered, while optimally dispatching DERs

parameters are determined once at the peak loading condition using $\bar{r}_{ij}^{\theta} = real(\frac{V_i^{\theta} - V_j^{\theta}}{I_{ij}^{\theta}})$ and $\bar{x}_{ij}^{\theta} = imag(\frac{V_i^{\theta} - V_j^{\theta}}{I_{ij}^{\theta}})$. The linearized power flow algorithm requires traversing the nodes of the directed graph in order which is done using breadth first search. The feeder has a 3-phase AVR on bus 150, a 1-phase AVR on bus 9, two 1-phase AVRs on bus 25 and three 1-phase AVRs on bus 160 as shown in Fig. 3.6. The AVRs have unmonitored automatic LDCs with no remote-control capabilities and have unique $\bar{r}_{kj}^{\theta,v}$, $\bar{x}_{kj}^{\theta,v}$, $\bar{V}_{kj}^{\theta,l}$ and $\bar{D}_{kj}^{\theta,l}$ settings. A voltage-based controller is added to one of the four capacitor banks for testing the method. The presence of 2 normally open tie switches and 7 normally closed switches creates 7 load sections in the microgrid. All the 91 loads have a small rooftop PV system making them NM loads and 5 large dispatchable DERs have been added randomly in the load sections.

3.4.1 Impact of Voltage Regulation Devices' States on Voltages

To demonstrate the importance of considering device states during microgrid restoration, an outage is created in the 123-node OpenDSS model during high loading conditions. The AVRs are locked in higher tap positions and the capacitor banks are ON. Two optimal power flow (OPF) problems are solved. In the first OPF, states are estimated using the MILP formulation proposed in section 3.1 and are used while dispatching DERs. In the second OPF, DERs are dispatched assuming all devices are in the neutral position as is typically done. Both OPFs converge, however, on applying their optimal DER dispatch in

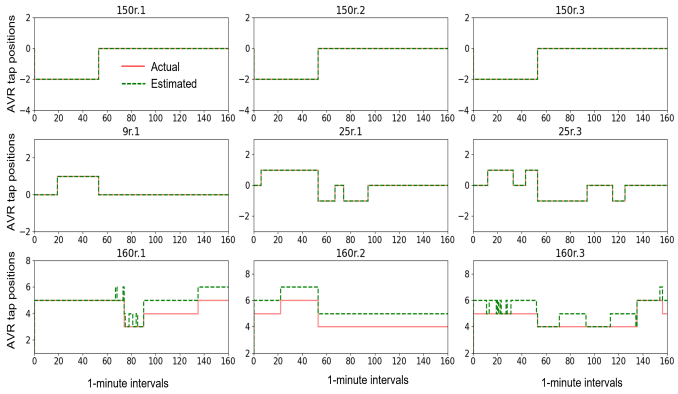

Figure 3.8: Tap estimation results with limited measurements using MILP formulation proposed in section 3.3

the OpenDSS model, only the first OPF is able to maintain voltages within the desired ANSI A Range as shown in Fig. 3.7(a). Much higher voltages are observed when device states are not considered as can be seen in Fig. 3.7(b). Such high voltages can trip inverters leading to microgrid service restoration failure.

3.4.2 Quasi Static Time Series Validations using OpenDSS

Quasi Static Time Series (QSTS) simulations [89] are performed at 1-minute resolution for several hours in the OpenDSS model with unique load and PV irradiance profiles. Intermittency in solar generation results in bidirectional power flows and voltage changes causing the AVRs to change tap positions. The controllable capacitor bank stays in the OFF position. These QSTS simulations are used to validate the effectiveness of the method proposed in section 3.1.

In the first QSTS simulation, limited line flow and voltage measurements are used to estimate device states using the MILP formulation proposed in section 3.3. The randomly chosen lines and buses shown in red in Fig. 3.6 do not have AMI meters. Fig. 3.8 shows a comparison of the actual tap positions observed in OpenDSS and the estimated tap positions. The proposed

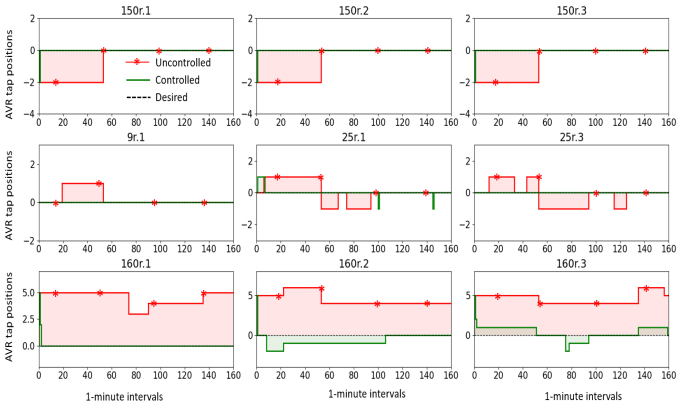

Figure 3.9: Taps controlled at neutral position (tap=0) throughout the QSTS simulation using the method proposed in section 3.1

MILP formulation can accurately estimate tap positions throughout the QSTS simulation, with a maximum deviation of only 1 tap position out of the 33 possible tap positions.

The QSTS simulations are performed again, and in this second run, DERs are dispatched optimally while controlling the AVRs to be at the neutral position (tap=0) using the optimal control approach proposed in section 3.1. Fig. 3.9 shows a comparison of the uncontrolled tap positions, the controlled tap positions, and the desired tap position. The proposed method can control the tap positions of all the unmonitored AVRs with automatic LDC's at the desired neutral tap position. Minor deviations observed are due to the use of linearized power flow versus the non-linear power flow used in OpenDSS. The controllable capacitor bank also stays in the OFF position throughout the QSTS simulation. Solving each OPF to estimate device states takes 0.7 seconds on average and it takes 0.33 seconds to solve each OPF for controlling device states. OPF is formulated in the Python package PYOMO and the GLPK solver is used.

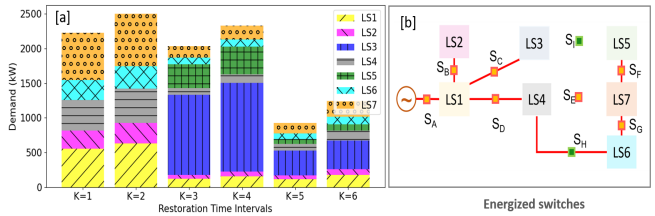

Figure 3.10: [a] Restoration sequence of load sections and their demand during each microgrid restoration interval; [b] Switches energized to restore all load sections of the microgrid

3.4.3 Sequential Microgrid Restoration Results

Sequential microgrid restoration is completed in $K = 6$ time intervals using the proposed method. AVRs are locked at their respective pre-outage tap positions of time interval 1 as shown in Fig. 3.8. All loads are NM loads with a 40% TCL percentage [50]. Pecan Street database [90] is used to obtain solar generation and demand profiles for the NM loads. Using the method proposed in section 3.3, demand forecasts $\bar{M}_i^L(k)$ which include the CLPU demand, are obtained for each NM load for the 6 restoration intervals.

The switches energized to restore all 7 load sections and the sequence in which they are energized can be seen in Fig. 3.10. This figure shows that the demand of each load section follows the expected pattern shown in Fig. 3.3[c]. For instance, LS3 is energized at interval 3 and shows high demand due to the combined effect of PVs being offline and CLPU. The demand then increases to peak demand in interval 4 as TCL diversity is lost. Then from interval 5 onwards the PV systems are back online after their *'enter service delay'* and demand reduces. Fig. 3.10[b] shows that normally open tie switches are used to meet all the constraints while maintaining a radial topology.

Figure 3.11 presents a comparison of the forecasted versus actual demands observed during the 6 restoration intervals. The *actual demand* is obtained by summing the demand, solar generation and the CLPU demand. The forecasted demand using the proposed disaggregation method (*Proposed Disagg*) in section 3.2 required only one solar generation meter

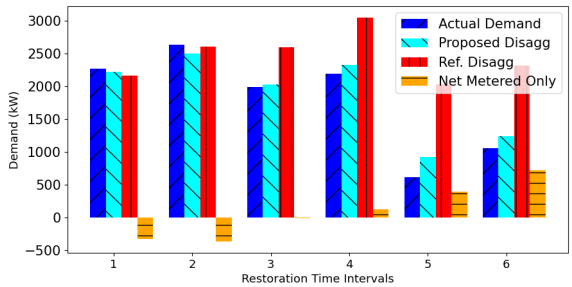

Figure 3.11: Comparison of actual demand with demand forecasts obtained using the approach proposed in section 3.2, disaggregation approach in [1], and only NM time series data.

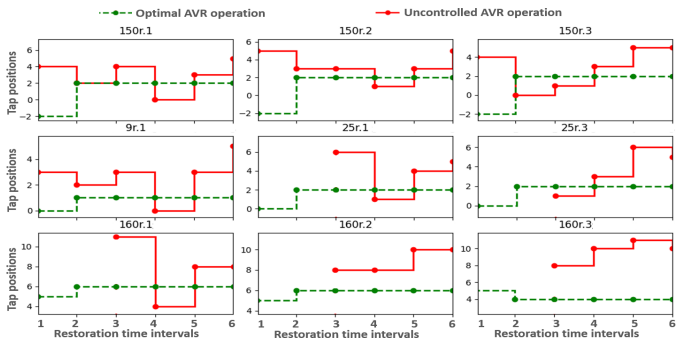

Figure 3.12: AVR tap positions during microgrid restoration with and without the proposed optimal control approach

per load section. This meter is deployed at the NM load exhibiting the highest average correlation in historical NM time series data with all other NM loads in the load section. The *Proposed Disagg* demand is compared with the disaggregation approach (*Ref. Disagg*) proposed in [1]. 3 randomly deployed solar generation meters per load section are used for the *Ref. Disagg* approach. The demand forecasts using only the historical NM time series (*NM Only*), while ignoring the *'enter service delay'* and CLPU phenomenon are also presented. The *Proposed Disagg* approach generates the most accurate NM demand forecasts in all 6 restoration time intervals. The accuracy of forecasts obtained using the *Ref. Disagg* approach decreases significantly as time horizon increases. Using only the NM time series-based forecasts causes large demand generation imbalance, leading to frequency instability and restoration failure.

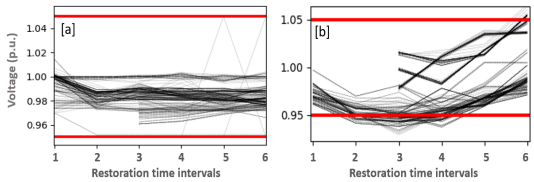

Figure 3.13: All nodal voltages during microgrid restoration [a] with, and [b] without the proposed optimal control approach

Figures 3.12 and 3.13 show the AVR tap positions and all nodal voltages during the 6 restoration intervals, with and without the application of the optimal control approach proposed in this chapter. These figures show that when AVR operation is not coordinated with DER dispatch, frequent large tap changes are seen leading to both over and under voltages and possibly restoration failure. Using the proposed optimal control approach, AVRs are energized while considering their estimated pre-outage states. At their second energization interval, the optimal tap position is evaluated and such AVR PCC voltage and line flows are created which makes their automatic LDC to command the taps to move to their optimal tap position. From the third energization interval onwards, the taps are maintained at these optimal tap positions, while maintaining all nodal voltages within the ANSI limits throughout the successful sequential microgrid restoration.

3.4.4 Algorithmic Complexity

As described in section 3.3, multiple contributions have been made to tighten and reduce the search space of the proposed MILP based sequential microgrid restoration algorithm. To highlight the impact of these contributions on algorithmic complexity, a sensitivity study is performed. In this study, the total number of restoration time intervals are increased from $K = 3$ to $K = 8$. The computation time reduction using the proposed approach is highlighted by comparing two scenarios, one where the proposed approach is used versus

one where it not used. The simulations are performed on a quad-core 11th Gen Intel-i5 2.4 GHz personal computer. As shown in Table 3.1, significant reductions in computational time complexity are observed with the proposed approach which can shorten the microgrid outage times.

Table 3.1: Computational Time Complexity of the Proposed Algorithm

Total restoration intervals (K)	3	4	5	6	7	8
Computational time without proposed approach (seconds)	26.4	11.6	26.9	60.5	50.4	254.8
Computational time of proposed approach (seconds)	4.2	6.6	11.7	37.3	32.1	46.4
Percentage reduction of computational time	84.1	43.2	56.3	38.4	36.2	81.8

Chapter 4

Ensuring Controllability and Stability of Microgrids During Dispatch and Restoration

The power grid is experiencing a significant increase in penetration of IBRs. Traditionally the power grid consisted of thousands of conventional synchronous generators being controlled by their primary controllers such as the governor and the exciter, and secondary controllers such as the automatic generation control. However with the integration of these IBRs the inertia of the power grid is reducing and the new capabilities provided by IBRs must be leveraged to ensure stability and controllability of the power grid. It is thus essential to accurately model the dynamics of conventional generators and IBRs and their grid interactions. However, an accurate model of each such generation source and its primary controllers requires dozens of states. Since there are thousands of such generation sources

(***to be submitted***) A.K. Jain, C-C. Liu., A.K. Bharati, K. Schneider, F. Tuffner and D. Ton, "Ensuring Microgrid Controllability During Dispatch and Restoration," IEEE Transactions on Power Systems, 2024.

and their primary controllers integrated in the electric grid, accurate reduced order models are required to enable real time control.

As described in the introduction, when new optimal dispatch settings are applied to the primary controllers of the DERs, the microgrid experiences transients which can cause instability. To ensure stability, the correct control mode (GFM or GFL) of the IBRs must be determined and IBRs should be switched to these control modes to ensure stability and controllability of the microgrid. The behavior of the microgrid as it switches from the previous optimal dispatch to the new optimal dispatch can be analyzed by modeling it as a switched linear system. Switched linear systems are a special class of hybrid dynamical systems that have mainly continuous dynamics with some discrete events such as switching [91].

In a microgrid all parameters such as voltages and currents are continuous but experience a sudden change when it switches to the new optimal dispatch. Thus, a state space model can be created to model the behavior of the microgrid with the previous optimal dispatch and another state space model can be created to model the behavior of the microgrid with the new optimal dispatch. However, if the state space model with the new optimal dispatch is found to be unstable, one or more IBRs can be switched to another control mode (GFM to GFL or vice versa) to create additional options which may be stable. Throughout this chapter, the switched system would refer to the microgrid along with the various DERs integrated in the microgrid. The system or the microgrid does not change, only a DER can change its control mode or its configuration. When a DER changes its configuration, a new state space model can be created to represent the microgrid. The K such state space models, hereafter referred to as the 'subsystems', formed through the change in configuration of DERs in a microgrid with arbitrary switching can be written as,

$$\dot{x}(t) = A_i x(t) + B_i u(t),\ i \in \{1, ..., K\} \tag{4.1}$$

The remaining of this chapter is organized as follows: section 4.1 presents how the the stability and controllability of switched linear systems can be analyzed. Section 4.2 presents an approach to determine the operating points from the optimal dispatch. The approach is demonstrated using the modified IEEE 13-node test feeder as an example and can be extended to any larger model as well. Section 4.3 presents an approach to determine the state space models as DERs change their configuration from GFM to GFL or vice versa. The proposed computationally efficient approach in sections 4.1 to 4.3 reduces the number of states in the models and is not only applicable to microgrids of any size but can be used to model the bulk grid as well. A case study is then presented in section 4.4 to validate the effectiveness of the proposed methodology in maintaining the stability and controllability of the microgrid.

4.1 Stability and Controllability of Switched Linear Systems

The stability of linear systems can be determined using their eigenvalues. If the real part of all eigenvalues is in the left-half of the complex plane, then the linear system is stable. While the same concept can be used to analyze the stability of the K microgrid subsystems, it cannot be used to analyze the stability of the switched systems. This is because switched systems are non-linear due to the presence of discrete switching between the different subsystems. Thus, the Lyapunov function approach must be used to analyze the stability of switched linear systems.

4.1.1 Stability of Switched Linear Systems

Given a system $\dot{y} = g(y)$, if there exists a positive definite continuously differential function $F(y)$ such that $F(0) = 0$ and $F(y) > 0,\ \forall\ y \neq 0$ whose derivative along solutions of $\dot{y} = g(y)$ satisfies $\dot{F}(y) \leq 0$, then the system is stable as per the Lyapunov stability criterion [92]. Extending this definition to the various individual subsystems where each subsystem can be defined as $\dot{x} = Ax, A \in \mathbb{R}^{n\times n}$. Considering a positive definite quadratic Lyapunov funtion, $F(x) = x^T Lx$. Since this function is positive definite it must satisfy, $F(0) = 0,$ and $F(x) > 0,\ \forall\ x \neq 0$ which also implies that L is a symmetric positive definite matrix.

Now in order to check if the system $\dot{x} = Ax, A \in \mathbb{R}^{n\times n}$ is stable according to the Lyapunov definition, we must check whether $\dot{F}(x) < 0$ along solutions of this system.

$$\dot{F}(x) = \dot{x}^T Lx + x^T L\dot{x} \tag{4.2}$$

The solutions of the system are $\dot{x}^T = (Ax)^T$ and $\dot{x} = (Ax)$. Upon substituting,

$$\dot{F}(x) = (Ax)^T Lx + x^T L(Ax) \implies x^T(A^T L + LA)x < 0 \tag{4.3}$$

Thus in order for $\dot{F}(x) < 0, \forall x$, $(A^T L + LA)$ must be negative definite. Assuming a positive definite L exists which satisfies this condition, and for any eigenvalue λ_k of A which has a non-zero eigenvector u_k, whose conjugate transpose is u_k^H then,

$$u_k^H(A^T L + LA)u_k < 0 \implies u_k^H A^T Lu_k + u_k^H LAu_k < 0 \tag{4.4}$$

Here $Au_k = \lambda_k u_k$, this implies that $(Au_k)^T = \lambda_k u_k^T$. Taking its conjugate we get $u_k^H A^T =$

$\lambda_k^* u_k^H$. Substituting this we get,

$$\lambda_k^* u_k^H L u_k + u_k^H L \lambda_k u_k = (\lambda_k^* + \lambda_k) u_k^H L u_k < 0 \tag{4.5}$$

Since, $u_k^H L u_k > 0$ as L is positive definite, then $Re(\lambda_k) < 0$. This implies that using the Lyapunov stability definition, in order for the system $\dot{x} = Ax, A \in \mathbb{R}^{n \times n}$ to be stable, there must exist a positive definite L matrix such that $(A^T L + LA) < 0$ [92].

In order to test the stability of a linear system we can use both eigenvalues as well as the definition shown above. The Lyapunov equation $(A^T L + LA) < 0$ is a linear matrix inequality (LMI) and can be solved using interior point methods [62]. However, these methods may not work as number of modes increase and numerical methods can be used to solve them.

This concept of using a quadratic Lyapunov function has been extended to linear switched systems as well. As described previously, the switched microgrid system has no restrictions on switching, thus stability definitions under arbitrary switching must be used. In order to analyze stability under arbitrary switching, all K subsystems in which the microgrid can switch to by changing the control mode of IBRs must be exponentially stable. Thus only the stable microgrid subsystems will be considered for switching. If any subsystem formed by changing the control mode of one or more IBRs is found to be unstable, it will not be considered as a part of the K subsystems. For these exponentially stable K subsystems, if a common quadratic Lyapunov function (CQLF) can be found then any arbitrary switching to any one of these subsystems would be stable. This condition can be equivalently expressed using the LMI presented above [93]. If a positive definite L matrix exists which satisfies,

$$(A_i^T L + LA_i) < 0, \forall\, i \in \{1, ..., K\} \tag{4.6}$$

then quadratic stability, which also implies asymptotic stability of the switched microgrid

systems is guaranteed.

However, this approach can be conservative. An example provided in [92] highlights this. In this example a switched system $\dot{x} = A_i x, i \in \{1, 2\}$, where $A_1 = \begin{bmatrix} -1 & -1 \\ 1 & -1 \end{bmatrix}$ and $A_2 = \begin{bmatrix} -1 & -10 \\ 0.1 & -1 \end{bmatrix}$ is considered. It can be seen that both systems are stable with eigenvalues at $(-1 \pm j)$. The system has also been shown to have global uniform exponential stability even under worst-case switching. However, a CQLF cannot be found for this system when $L = \begin{bmatrix} 1 & a \\ a & b \end{bmatrix}$. Upon using the $A_1^T L + LA_1 < 0$ and $A_2^T L + LA_2 < 0$ LMIs, it is observed that two non-intersecting ellipses are formed.

A less conservative approach should thus be used. Since each subsystem must be stable under arbitrary switching, a positive definite L matrix can be found for each subsystem given by the LMI's $A_i^T L_i + L_i A_i < 0, \forall i \in \{1, ..., K\}$. These individual matrices are then connected together using a switching function which must satisfy the minimum dwell time (T_d) requirement, which is the minimum time the microgrid must stay in any given subsystem [94]. The additional LMIs which are added in this multiple quadratic Lyapunov function approach are,

$$e^{A_i^T T_d} L_n e^{A_i T_d} - L_i < 0, \forall\, i \neq n \in \{1, ..., K\} \tag{4.7}$$

However, the existence of CQLF or MQLF is only a sufficient but not a necessary condition. Thus the approach adopted here is to consider only stable microgrid subsystems. Instead of trying to find a CQLF or MQLF for all of these subsystems together, the proposed approach starts by creating two subsystems. These two subsystems correspond to the microgrid with the previous dispatch and the new dispatch and all IBRs in the same control modes in both subsystems. If a CQLF or MQLF can be found then no changes are required. If CQLF or

MQLF cannot be found then a new subsystem is formed by changing the control mode of the lowest rated switchable IBR from its current mode to GFM or GFL. CQLF and MQLF are then determined for the previous dispatch subsystem and this new subsystem with the new dispatch and changed IBR control mode. The approach is repeated, first by changing control mode of the next higher rated IBR and then by changing control modes of more than one IBR.

In practice, in a microgrid there will only be a couple of large enough switchable IBRs and thus only a limited number of subsystems will exist. Thus the existence or absence of a switched stable subsystem without having to change the new optimal dispatch can be easily determined. The approach proposed here tries to minimize the number of IBRs which have to change control modes. However, it is possible that even after changing the control modes of all the IBRs in the microgrid, a stable switched subsystem cannot be found. In such a scenario, the controllability of the pair of switched subsystems can be determined. If any pair of subsystems is found to be controllable, then a feedback control can be designed to stabilize the system during the planned transition to the new optimal dispatch.

4.1.2 Controllability of Switched Linear Systems

Any linear time invariant (LTI) system of the form $\dot{x}(t) = Ax(t) + Bu(t)$, is said to be controllable if a control input signal $u(t)$ can be designed which can steer the system from any initial state $x(0) = x_0$ to any final state $x(t_f) = x_f$ in a finite amount of time. The controllablility of a LTI system can be determined by evaluating the controllability matrix $C_{lti} = [B\ AB\ A^2B\ ...\ A^{n-1}B]$. If C_{lti} is found to be full row rank, then the LTI system is said to be controllable.

Controllability for switched linear systems is defined in a very similar manner. A switched

linear system of the form $\dot{x}(t) = A_i x(t) + B_i u(t),\ i \in \{1, ..., K\}$ is said to be controllable if a switching sequence and control input $u(t)$ can be designed that can transfer the system from any initial state $x(0) = x_0$ to the stable state $x(t_f) = 0$ within finite time. It can be seen that in this definition both a switching signal and a control input can be used to control the switched system. For instance in the DC-DC converter described in [61], the input signal which is the DC input voltage from the renewable energy source cannot be controlled. Thus, PWM control mechanism is used to design a stabilizing switching sequence. In a microgrid the switching is arbitrary, however the control input can be controlled, such as by using feedback control. A LMI based approach for designing a feedback control law to stabilize switched linear systems is proposed in [95].

A controllability matrix C_s similar to C_{lti} can be defined for switched linear systems as well [96]. This matrix can be written as,

$$C_s = [B_1, B_2, ..., B_K, A_1B_1, A_2B_1, ..., A_KB_1, ..., A_1B_K, A_2B_K, ..., A_KB_K, A_1^2B_1, ..., A_K^{n-1}B_K] \tag{4.8}$$

However, writing this matrix requires determination of a large number of terms [97]. To reduce this computational burden an alternative approach is presented in [98]. A linear space U can be defined as follows:

$$\langle A|U\rangle = \sum_{i=1}^{n} A^{i-1}U \tag{4.9}$$

A cyclic invariant subspace can be generated by U through the cycle of matrix A as shown below,

$$U_1 = \sum_{i=1}^{K}\langle A_i|B_i\rangle;\ U_2 = \sum_{i=1}^{K}\langle A_i|U_1\rangle, ..., U_n = \sum_{i=1}^{K}\langle A_i|U_{n-1}\rangle \tag{4.10}$$

The system is said to be controllable if $rank(U_n) = n$ or $dim(U_n) = n$ [61]. Another

important result because of which all subspaces are not required is that $U_1 \subset U_2 \subset ... \subset U_n$. Thus if $rank(U_1) = n$, then $rank(U_n) = n$ and we do not need to evaluate the entire subspace sequence.

As can be seen that in order to implement these definitions, state space models are required to represent the different subsystems. There is also a need to reduce the number of states so as to reduce the computational demand to enable real-time implementation of the proposed approach. The next sections describe how these state space models are developed.

4.2 Determining Operating Point From Optimal Dispatch

To reduce the complexity of each subsystem, the microgrid model must be reduced to only the DER nodes. Techniques to eliminate these interior non-DER nodes such as by using Kron reduction have been proposed before [99]. A grid probing based approach is used here to reduce the microgrid network. Once the reduced network parameters are obtained, since the optimal power flow does not provide voltage angles, an approach is needed to estimate the angles based on the received real power set points. The IEEE 13 node feeder as shown in Fig. 4.1, is used as a microgrid to illustrate the proposed approach. However this approach can be extended to any other feeder as well. This microgrid has a SG on node 633, and two IBRs capable of switching between GFM and GFL modes are connected on nodes 675 and 680.

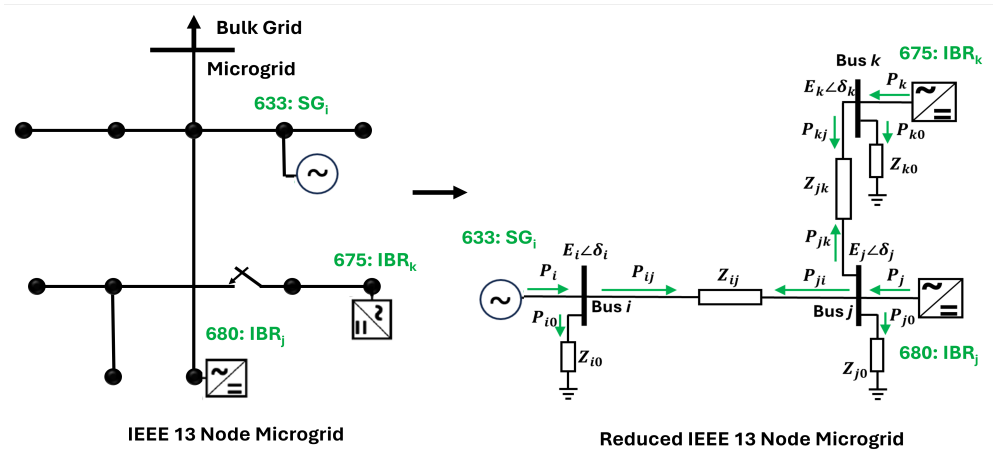

Figure 4.1: Reduced IEEE 13 node model with a SG and two IBRs

4.2.1 Power Flow Equations

The DERs in the reduced network shown in Fig. 4.1 have terminal voltages $(E_i\angle\delta_i)$, $(E_j\angle\delta_j)$ and $(E_k\angle\delta_k)$ respectively. Their respective real power injections are P_i, P_j and P_k. These three buses host constant impedance loads with impedances Z_{i0}, Z_{j0} and Z_{k0}. Buses i and j are connected by a line with impedance Z_{ij}, while the buses j and k are connected by a line with impedance Z_{jk}. The corresponsing admittances are,

$$Y_{i0} = \frac{1}{Z_{i0}} = G_{i0} + jB_{i0} = |Y_{i0}|\angle\phi_{i0} \tag{4.11}$$

$$Y_{j0} = \frac{1}{Z_{j0}} = G_{j0} + jB_{j0} = |Y_{j0}|\angle\phi_{j0} \tag{4.12}$$

$$Y_{k0} = \frac{1}{Z_{k0}} = G_{k0} + jB_{k0} = |Y_{k0}|\angle\phi_{k0} \tag{4.13}$$

$$Y_{ij} = \frac{1}{Z_{ij}} = G_{ij} + jB_{ij} = |Y_{ij}|\angle\phi_{ij} \tag{4.14}$$

$$Y_{jk} = \frac{1}{Z_{jk}} = G_{jk} + jB_{jk} = |Y_{jk}|\angle\phi_{jk} \tag{4.15}$$

The real power output of SG_i can be written as [100], [101].

$$P_i = P_{ij} + P_{i0} \tag{4.16}$$

$$= G_{ij}(E_i^2 - E_iE_jcos(\delta_{ij})) - B_{ij}E_iE_jsin(\delta_{ij}) + G_{i0}E_i^2 \tag{4.17}$$

$$= G_{ii}E_i^2 - E_iE_j(|Y_{ij}|cos(-\phi_{ij})cos(\delta_{ij}) - |Y_{ij}|sin(-\phi_{ij})sin(\delta_{ij})) \tag{4.18}$$

$$= G_{ii}E_i^2 - |Y_{ij}|E_iE_jcos(\delta_{ij} - \phi_{ij}) \tag{4.19}$$

where, $G_{ii} = G_{ij} + G_{i0}$ and $\delta_{ij} = \delta_i - \delta_j$. Similarly, for IBR_k,

$$P_k = G_{kk}E_k^2 - |Y_{jk}|E_jE_kcos(\delta_{kj} - \phi_{jk}) \tag{4.20}$$

$$= G_{kk}E_k^2 - |Y_{jk}|E_jE_kcos(-\delta_{jk} - \phi_{jk}) \tag{4.21}$$

$$= G_{kk}E_k^2 - |Y_{jk}|E_jE_kcos(\delta_{jk} + \phi_{jk}) \tag{4.22}$$

where, $G_{kk} = G_{jk} + G_{k0}$ and $\delta_{jk} = \delta_j - \delta_k$

It can be seen that $P_i(\delta_{ij})$ is a function of δ_{ij} alone and $P_k(\delta_{jk})$ is a function of δ_{jk} alone, assuming $E_i \approx E_k \approx 1p.u.$. Their expressions can be linearized using first order Taylor series expanison $\mathcal{T}(P_i(\delta_{ij})|\delta_{ij}^0) = P_i(\delta_{ij}^0) + P_i'(\delta_{ij}^0)(\delta_{ij} - \delta_{ij}^0)$, at the operating point $(\delta_{ij}^0, \delta_{jk}^0)$.

$$\mathcal{T}(P_i(\delta_{ij})|\delta_{ij}^0) = G_{ii} - |Y_{ij}|cos(\delta_{ij}^0 - \phi_{ij}) + |Y_{ij}|sin(\delta_{ij}^0 - \phi_{ij}) \times (\delta_{ij} - \delta_{ij}^0) \tag{4.23}$$

$$\mathcal{T}(P_k(\delta_{jk})|\delta_{jk}^0) = G_{kk} - |Y_{jk}|cos(\delta_{jk}^0 + \phi_{jk}) + |Y_{jk}|sin(\delta_{jk}^0 + \phi_{jk}) \times (\delta_{jk} - \delta_{jk}^0) \tag{4.24}$$

The small changes in real power around the operating point $(\delta_{ij}^0, \delta_{jk}^0)$, can be obtained using [100],

$$\Delta P_i = \mathcal{T}(P_i(\delta_{ij})|\delta_{ij}^0) - P_i(\delta_{ij})|\delta_{ij}^0 = -c_1\Delta\delta_{ij} \tag{4.25}$$

$$\Delta P_k = \mathcal{T}(P_k(\delta_{jk})|\delta_{jk}^0) - P_k(\delta_{jk})|\delta_{jk}^0 = -c_3\Delta\delta_{jk} \tag{4.26}$$

where $c_1 = -|Y_{ij}|sin(\delta^0_{ij} - \phi_{ij})$, $c_3 = -|Y_{jk}|sin(\delta^0_{jk} + \phi_{jk})$, $\Delta\delta_{ij} = (\delta_{ij} - \delta^0_{ij})$, $\Delta\delta_{jk} = (\delta_{jk} - \delta^0_{jk})$.

Power flow equation for IBR_j is slightly different as it is connected to both the SG on node i and the IBR on node k. Writing expressions for this IBR is also a more generalized case. The three bus model used here covers all possible IBR connection configurations in any radially operated microgrid. Referring to Fig. 4.1, the real power output of IBR_j can be written as,

$$P_j = P_{ji} + P_{jk} + P_{j0} \tag{4.27}$$

$$= G_{ij}(E_j^2 - E_iE_jcos(\delta_{ji})) - B_{ij}E_iE_jsin(\delta_{ji}) + G_{jk}(E_j^2 - E_jE_kcos(\delta_{jk})) \tag{4.28}$$

$$- B_{jk}E_jE_ksin(\delta_{jk}) + G_{j0}E_j^2 \tag{4.29}$$

$$= (G_{ij} + G_{jk} + G_{j0})E_j^2 - E_iE_j(|Y_{ij}|cos(-\phi_{ij})cos(\delta_{ji}) - |Y_{ij}|sin(-\phi_{ij})sin(\delta_{ji})) \tag{4.30}$$

$$- E_jE_k(|Y_{jk}|cos(-\phi_{jk})cos(\delta_{jk}) - |Y_{jk}|sin(-\phi_{jk})sin(\delta_{jk})) \tag{4.31}$$

$$= G_{jj}E_j^2 - |Y_{ij}|E_iE_jcos(-\delta_{ij} - \phi_{ij}) - |Y_{jk}|E_jE_kcos(\delta_{jk} - \phi_{jk}) \tag{4.32}$$

$$= G_{jj}E_j^2 - |Y_{ij}|E_iE_jcos(\delta_{ij} + \phi_{ij}) - |Y_{jk}|E_jE_kcos(\delta_{jk} - \phi_{jk}) \tag{4.33}$$

$$\tag{4.34}$$

where, $G_{jj} = G_{ij} + G_{jk} + G_{j0}$, $\delta_{ij} = \delta_i - \delta_j$ and $\delta_{jk} = \delta_j - \delta_k$. It can be seen that $P_j(\delta_{ij}, \delta_{jk})$ is a function of δ_{ij} and δ_{jk} alone and can be linearized around the operating point $(\delta^0_{ij}, \delta^0_{jk})$ using Taylor's series expansion as before. The Taylor's series expansion for this bivariate function is $\mathcal{T}(P_j(\delta_{ij}, \delta_{jk})|(\delta^0_{ij}, \delta^0_{jk})) = P_j(\delta^0_{ij}, \delta^0_{jk}) + P'_{j,\delta_{ij}}(\delta^0_{ij}, \delta^0_{jk})(\delta_{ij} - \delta^0_{ij}) + P'_{j,\delta_{jk}}(\delta^0_{ij}, \delta^0_{jk})(\delta_{jk} - \delta^0_{jk})$

$$\begin{aligned}\mathcal{T}(P_j(\delta_{ij}, \delta_{jk})|(\delta^0_{ij}, \delta^0_{jk})) = G_{jj} - |Y_{ij}|cos(\delta^0_{ij} + \phi_{ij}) - |Y_{jk}|cos(\delta^0_{jk} - \phi_{jk}) \\ + |Y_{ij}|sin(\delta^0_{ij} + \phi_{ij}) \times (\delta_{ij} - \delta^0_{ij}) + |Y_{jk}|sin(\delta^0_{jk} - \phi_{jk}) \times (\delta_{jk} - \delta^0_{jk})\end{aligned} \tag{4.35}$$

The small changes in real power around the operating point $(\delta^0_{ij}, \delta^0_{jk})$, can be obtained using

[100],

$$\Delta P_j = \mathcal{T}(P_j(\delta_{ij}, \delta_{jk})|(\delta^0_{ij}, \delta^0_{jk})) - P_j(\delta_{ij}, \delta_{jk})|(\delta^0_{ij}, \delta^0_{jk})$$

$$= |Y_{ij}|sin(\delta^0_{ij} + \phi_{ij}) \times (\delta_{ij} - \delta^0_{ij}) + |Y_{jk}|sin(\delta^0_{jk} - \phi_{jk}) \times (\delta_{jk} - \delta^0_{jk})$$
$$= -c_{21}\Delta\delta_{ij} - c_{22}\Delta\delta_{jk} \quad (4.36)$$

where $c_{21} = -|Y_{ij}|sin(\delta^0_{ij} + \phi_{ij})$ and $c_{22} = -|Y_{jk}|sin(\delta^0_{jk} - \phi_{jk})$.

4.2.2 Estimating Operating Point From Optimal Dispatch

A grid probing based approach is developed here. The power flow equations derived previously are shown below after substituting voltages to be 1.p.u.

$$P_i = G_{ii} - |Y_{ij}|cos(\delta_{ij} - \phi_{ij}) \quad (4.37)$$

$$P_k = G_{kk} - |Y_{jk}|cos(\delta_{jk} + \phi_{jk}) \quad (4.38)$$

$$P_j = G_{jj} - |Y_{ij}|cos(\delta_{ij} + \phi_{ij}) - |Y_{jk}|cos(\delta_{jk} - \phi_{jk}) \quad (4.39)$$

Using P_i as an example, by using a measurement device such as a phasor measurement unit (PMU), we can obtain the voltage and current phasors for all DERs which will be time aligned. Using these PMUs we can get $\delta_{ij} = \delta_i - \delta_j$ and the terminal powers P_i as the optimal DER set points are varied and the microgrid reaches steady state. Thus, $\bar{\delta}_{ij}, \bar{P}_i$ are represented with bars as these are available via PMU measurements. The variables to be

determined are the equivalent impedances $G_{ii}, |Y_{ij}|, \phi_{ij}$.

$$\bar{P}_i = G_{ii} - |Y_{ij}|cos(\bar{\delta}_{ij} - \phi_{ij}) \tag{4.40}$$

$$\bar{P}_i = G_{ii} - |Y_{ij}|cos(\bar{\delta}_{ij})cos(\phi_{ij}) - |Y_{ij}|sin(\bar{\delta}_{ij})sin(\phi_{ij}) \tag{4.41}$$

Let $a_{ij} = |Y_{ij}|cos(\phi_{ij})$ and $b_{ij} = |Y_{ij}|sin(\phi_{ij})$, thus,

$$\bar{P}_i = G_{ii} - cos(\bar{\delta}_{ij})a_{ij} - sin(\bar{\delta}_{ij})b_{ij} \tag{4.42}$$

In this expression the variables are $G_{ii}, a_{ij},$ and b_{ij}. We can obtain multiple $\bar{\delta}_{ij}^k, \bar{P}_i^k$ values by running multiple simulations with different optimal power flow dispatches. The same can be done practically in the field by deployment of PMUs. We can then write expressions for each pair of $\bar{\delta}_{ij}^k, \bar{P}_i^k$, to get,

$$\begin{bmatrix} \bar{P}_i^1 \\ \bar{P}_i^2 \\ . \\ . \\ \bar{P}_i^K \end{bmatrix} = \begin{bmatrix} 1 & -cos(\bar{\delta}_{ij}^1) & -sin(\bar{\delta}_{ij}^1) \\ 1 & -cos(\bar{\delta}_{ij}^2) & -sin(\bar{\delta}_{ij}^2) \\ . & . & . \\ . & . & . \\ 1 & -cos(\bar{\delta}_{ij}^K) & -sin(\bar{\delta}_{ij}^K) \end{bmatrix} \begin{bmatrix} G_{ii} \\ a_{ij} \\ b_{ij} \end{bmatrix} \tag{4.43}$$

In matrix notation,

$$\boldsymbol{p_i}^{K\times 1} = \boldsymbol{C_{ij}}^{K\times 3}\boldsymbol{x_i}^{3\times 1} \tag{4.44}$$

We can now find $\boldsymbol{x_i}$ by taking the pseudoinverse as follows,

$$\boldsymbol{x_i} = (\boldsymbol{C_{ij}}^T\boldsymbol{C_{ij}})^{-1}\boldsymbol{C_{ij}}^T\boldsymbol{p_i} \tag{4.45}$$

Once $\boldsymbol{x_i}$ is estimated we get $G_{ii}, a_{ij},$ and b_{ij}. Now ϕ_{ij} can be obtained using $\phi_{ij} = atan(b_{ij}/a_{ij})$. $|Y_{ij}|$ can now be obtained as $|Y_{ij}| = a_{ij}/cos(\phi_{ij})$.

Similarly for IBR k, $\bar{\delta}_{jk}, \bar{P}_k$ are represented with bars as these are available via PMU measurements. The variables to be determined are the equivalent impedances $G_{kk}, |Y_{jk}|, \phi_{jk}$.

$$P_k = G_{kk} - |Y_{jk}|cos(\delta_{jk} + \phi_{jk}) \tag{4.46}$$

$$\bar{P}_k = G_{kk} - |Y_{jk}|cos(\bar{\delta}_{jk})cos(\phi_{jk}) + |Y_{jk}|sin(\bar{\delta}_{jk})sin(\phi_{jk}) \tag{4.47}$$

Let $a_{jk} = |Y_{jk}|cos(\phi_{jk})$ and $b_{jk} = |Y_{jk}|sin(\phi_{jk})$, thus,

$$\bar{P}_k = G_{kk} - cos(\bar{\delta}_{jk})a_{jk} + sin(\bar{\delta}_{jk})b_{jk} \tag{4.48}$$

In this expression the variables are $G_{kk}, a_{jk},$ and b_{jk}. We can obtain multiple $\bar{\delta}^x_{jk}, \bar{P}^x_k$ values by running multiple simulations with different optimal power flow dispatches. The same can be done practically in the field by deployment of PMUs. We can then write expressions for each pair of $\bar{\delta}^x_{jk}, \bar{P}^x_k$, to get,

$$\begin{bmatrix} \bar{P}^1_k \\ \bar{P}^2_k \\ . \\ . \\ \bar{P}^X_k \end{bmatrix} = \begin{bmatrix} 1 & -cos(\bar{\delta}^1_{jk}) & sin(\bar{\delta}^1_{jk}) \\ 1 & -cos(\bar{\delta}^2_{jk}) & sin(\bar{\delta}^2_{jk}) \\ . & . & . \\ . & . & . \\ 1 & -cos(\bar{\delta}^X_{jk}) & sin(\bar{\delta}^X_{jk}) \end{bmatrix} \begin{bmatrix} G_{kk} \\ a_{jk} \\ b_{jk} \end{bmatrix} \tag{4.49}$$

In matrix notation,

$$\boldsymbol{p_k}^{X\times 1} = \boldsymbol{C_{jk}}^{X\times 3}\boldsymbol{x_k}^{3\times 1} \tag{4.50}$$

We can now find $\boldsymbol{x_k}$ by taking the pseudoinverse as follows,

$$\boldsymbol{x_k} = (\boldsymbol{C_{jk}}^T \boldsymbol{C_{jk}})^{-1} \boldsymbol{C_{jk}}^T \boldsymbol{p_k} \tag{4.51}$$

Once $\boldsymbol{x_k}$ is estimated we get $G_{kk}, a_{jk},$ and b_{jk}. Now ϕ_{jk} can be obtained using $\phi_{jk} = atan(b_{jk}/a_{jk})$. $|Y_{jk}|$ can now be obtained as $|Y_{jk}| = a_{jk}/cos(\phi_{jk})$.

If needed we can obtain G_{jj} using these estimates as $G_{jj} = P_j + |Y_{ij}|cos(\delta_{ij} + \phi_{ij}) + |Y_{jk}|cos(\delta_{jk} - \phi_{jk})$. Once the estimates for $|Y_{ij}|, |Y_{jk}|, \phi_{ij}, \phi_{jk}, G_{ii}$ and G_{kk} are determined, we can evaluate the approximate operating points $(\delta^0_{ij}, \delta^0_{jk})$ for a given optimal dispatch (P^*_i, P^*_j, P^*_k) as,

$$\delta^0_{ij} = acos((G_{ii} - P^*_i)/|Y_{ij}|) + \phi_{ij} \tag{4.52}$$

$$\delta^0_{jk} = acos((G_{kk} - P^*_k)/|Y_{jk}|) - \phi_{jk} \tag{4.53}$$

Once the operating point estimates have been obtained, the power flow coefficients defined above can be obtained using, $c_1 = -|Y_{ij}|sin(\delta^0_{ij} - \phi_{ij})$, $c_{21} = -|Y_{ij}|sin(\delta^0_{ij} + \phi_{ij})$, $c_{22} = -|Y_{jk}|sin(\delta^0_{jk} - \phi_{jk})$, and $c_3 = -|Y_{jk}|sin(\delta^0_{jk} + \phi_{jk})$. These reduced microgrid network parameters will be used in the next section to determine the state space models.

4.3 State Space Modeling

In order to use switched linear systems theory concepts, irrespective of whether the IBRs operate in the grid following (GFL) mode or the grid forming (GFM) mode, the state vector should not change. Also, computationally efficient state space models are needed so that

the switched linear systems controllability matrix and CQLF and MQLF based stability definitions may be applied. Here, state space models which satisfy both of these criterion are developed.

In Fig. 4.1, the IBRs on buses j and k can operate in either GFM or GFL modes. Both IBRs can operate in the GFL mode as the voltage and frequency references can be created by the SG. Thus, the following DER combinations are possible:

- **Case 1:** IBR_j : GFM; IBR_k : GFM
- **Case 2:** IBR_j : GFM; IBR_k : GFL
- **Case 3:** IBR_j : GFL; IBR_k : GFM
- **Case 4:** IBR_j : GFL; IBR_k : GFL

4.3.1 Case 1: SG with Both IBRs in GFM Mode

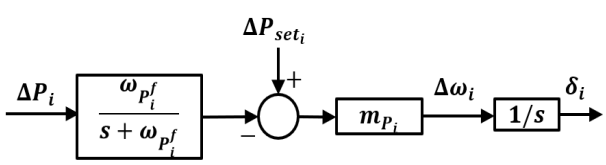

Figure 4.2: GFM Control Mode of an IBR

In this case, both IBRs are operating in the GFM mode. Through a literature review the key parameters which can impact the stability of a microgrid with multiple GFM mode IBRs were determined. It was found that negative damping terms may be introduced due to interactions among two GFM IBRs in islanded microgrids [102]. The virtual inertia term, damping and the line impedance were also found to impact stability in [103]. All of these parameters are included in the state space models derived here.

While several accepted transient equations models exist for SGs, there are no widely accepted transient equation models for GFM or GFL mode IBRs. The most commonly used primary control in IBRs in the GFM mode is droop control [56]. Frequency droop controlled GFM IBRs are typically modeled using a first order equation while neglecting other controls [104]. A first order low pass filter is present in droop controlled GFM IBRs. In fact the equivalence of droop control and virtual synchronous generator (VSG) control of GFM IBRs has also been established [105]. Thus the approach proposed here should work with VSG control as well. The swing equation for GFM mode IBR_k in line with the swing equation for a synchronous generator is derived first [106]. Considering its power low pass filter and assuming the inner loops are perfect as shown in Fig. 4.2, we can write,

$$\frac{1}{m_{P_k}\omega_{P_k^f}} s\Delta\omega_k + \frac{1}{m_{P_k}}\Delta\omega_k = \Delta P_{set_k} - \Delta P_k \tag{4.54}$$

where, m_{P_k} is the droop slope, $\omega_{P_k^f} = \frac{1}{T_{P_k^f}}$ is the bandwidth of the GFM power low pass filter, $T_{P_k^f}$ is the time constant of the GFM power low pass filter, $\Delta\omega_k$ is the angular frequency and ΔP_{set_k} is the input reference. It may be written as,

$$\frac{1}{m_{P_k}\omega_{P_k^f}}\Delta\dot{\omega}_k + \frac{1}{m_{P_k}}\Delta\omega_k = \Delta P_{set_k} - \Delta P_k \tag{4.55}$$

$$H_k\Delta\dot{\omega}_k + D_k\Delta\omega_k = \Delta P_{set_k} + c_3\Delta\delta_{jk} \tag{4.56}$$

$$\Delta\dot{\omega}_k = -\frac{D_k}{H_k}\Delta\omega_k + \frac{1}{H_k}\Delta P_{set_k} + \frac{c_3}{H_k}\Delta\delta_{jk} \tag{4.57}$$

where, $H_k = \frac{1}{m_{P_k}\omega_{P_k^f}} = \frac{T_{P_k^f}}{m_{P_k}}$ is the inertia of the GFM at bus k and $D_k = \frac{1}{m_{P_k}}$ is the damping of the GFM IBR.

The dynamics of the GFM mode IBR_j can similarly be written as,

$$\Delta\dot{\omega}_j = -\frac{D_j}{H_j}\Delta\omega_j + \frac{1}{H_j}\Delta P_{set_j} + \frac{c_{21}}{H_j}\Delta\delta_{ij} + \frac{c_{22}}{H_j}\Delta\delta_{jk} \tag{4.58}$$

The aggregate generator model for a SG as shown in Fig. 4.3 is taken from [107] and

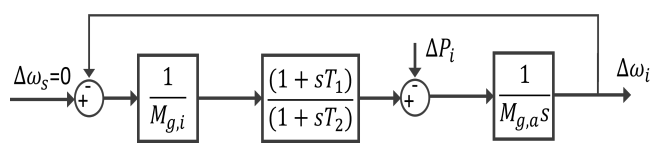

Figure 4.3: SG model for slow frequency dynamics studies

aggregate damping term is assumed to be negligible. Here $M_{g,a}$ is the aggregated inertia, $M_{g,i}$ is the droop coefficient of the governor, T_1 and T_2 are governor's transfer function's parameters, $\Delta\omega_s$ is the frequency reference and $\Delta\omega_i$ is the SG's angular frequency. The dynamics of the SG may thus be represented as,

$$M_{g,a}\Delta\dot{\omega}_i = \frac{1}{M_{g,i}}\frac{T_1}{T_2}(\frac{s+1/T_1}{s+1/T_2})(\Delta\omega_s - \Delta\omega_i) - \Delta P_i \tag{4.59}$$

This can be separated into two states by defining an internal state $\Delta\tau_i$,

$$\Delta\dot{\omega}_i = \frac{c_1}{M_{g,a}}\Delta\delta_{ij} - \frac{1}{M_{g,i}M_{g,a}}\frac{T_1}{T_2}\Delta\omega_i + \frac{1}{M_{g,a}}\Delta\tau_i + \frac{1}{M_{g,i}M_{g,a}}\frac{T_1}{T_2}\Delta\omega_s \tag{4.60}$$

$$\Delta\dot{\tau}_i = -\frac{1-\frac{T_1}{T_2}}{M_{g,i}T_2}\Delta\omega_i - \frac{1}{T_2}\Delta\tau_i + \frac{1-\frac{T_1}{T_2}}{M_{g,i}T_2}\Delta\omega_s \tag{4.61}$$

Thus, the state space model for this system can be written as,

$$\begin{bmatrix} \Delta\dot{\delta}_{ij} \\ \Delta\dot{\delta}_{jk} \\ \Delta\dot{\omega}_i \\ \Delta\dot{\tau}_i \\ \Delta\dot{\omega}_j \\ \Delta\dot{\omega}_k \end{bmatrix} = \begin{bmatrix} 0 & 0 & 1 & 0 & -1 & 0 \\ 0 & 0 & 0 & 0 & 1 & -1 \\ \frac{c_1}{M_{g,a}} & 0 & -\frac{1}{M_{g,i}M_{g,a}}\frac{T_1}{T_2} & \frac{1}{M_{g,a}} & 0 & 0 \\ 0 & 0 & -\frac{1-\frac{T_1}{T_2}}{M_{g,i}T_2} & -\frac{1}{T_2} & 0 & 0 \\ \frac{c_{21}}{H_j} & \frac{c_{22}}{H_j} & 0 & 0 & -\frac{D_j}{H_j} & 0 \\ 0 & \frac{c_3}{H_k} & 0 & 0 & 0 & -\frac{D_k}{H_k} \end{bmatrix} \begin{bmatrix} \Delta\delta_{ij} \\ \Delta\delta_{jk} \\ \Delta\omega_i \\ \Delta\tau_i \\ \Delta\omega_j \\ \Delta\omega_k \end{bmatrix} + \begin{bmatrix} 0 & 0 & 0 \\ 0 & 0 & 0 \\ \frac{1}{M_{g,i}M_{g,a}}\frac{T_1}{T_2} & 0 & 0 \\ \frac{1-\frac{T_1}{T_2}}{M_{g,i}T_2} & 0 & 0 \\ 0 & \frac{1}{H_j} & 0 \\ 0 & 0 & \frac{1}{H_k} \end{bmatrix} \begin{bmatrix} \Delta\omega_s \\ \Delta P_{set_j} \\ \Delta P_{set_k} \end{bmatrix} \quad (4.62)$$

4.3.2 Case 2: SG with IBR_j Operating in the GFM Mode and IBR_k Operating in GFL Mode

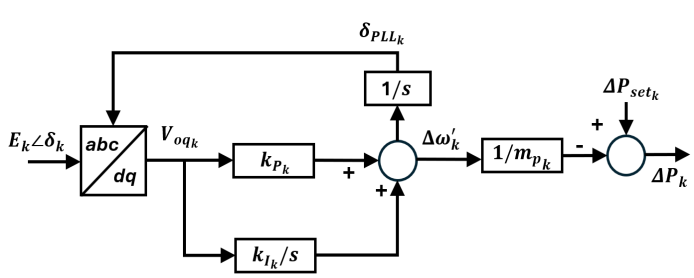

Figure 4.4: GFL control mode of an IBR

The IBR on node k is operating in the GFL mode. The phase locked loop (PLL) and the PLL's proportional and integral gains have been found to be critical parameters for impacting

the stability of a microgrid while operating with other GFM or GFL mode IBRs [103], [108]. Creating a swing equation equivalent for GFL mode of IBRs is challenging [107]. Such an equation was partially derived in [106], however, it was left with some higher order terms since power flow equations were not adequately considered. Efforts have been made to create a second order model of the GFL mode by considering only the PLL dynamics, however, simplified AC microgrid models are used [109]. Recent research utilizing detailed GFL IBR models has shown that the PLL loop has a much bigger influence on transient dynamics compared with the power loops [104]. This is why the second order GFL model consisting of the PLL dynamics has been described as the generalized swing equation model in [110]. A second order GFL IBR model which accurately considers the impact of dynamics of other DERs and the impact of power flow equations has been derived here.

The swing equation for GFL mode IBR_k has been derived by considering its PLL and the grid supportive frequency-watt function by building upon the partially derived model in [106]. The proportional-integral controller of the PLL controls the $q-$axis component of the grid voltage V_{oq_k} [111] to be zero by increasing or decreasing the angular frequency $\Delta\omega'_k$ of the GFL's PLL [56], [112]. The GFL PLL's phase angle δ_{PLL_k} can be obtained by integrating $\Delta\omega'_k$. Assuming the PLL tracks the frequency effectively and $E_k \approx 1p.u.$ we get,

$$V_{oq_k} = E_k sin(\delta_k - \delta_{PLL_k}) \approx (\delta_k - \delta_{PLL_k}) \approx \frac{\Delta\omega_k - \Delta\omega'_k}{s} \tag{4.63}$$

The output of the PLL's PI controller can be expressed as,

$$\Delta\omega'_k = (k_{P_k} + \frac{k_{I_k}}{s})V_{oq_k} = \frac{(k_{P_k}s + k_{I_k})(\Delta\omega_k - \Delta\omega'_k)}{s^2} \tag{4.64}$$

Here, k_{P_k}, k_{I_k} are the proportional and integral terms of the GFL PLL. Upon rearranging

the equation,

$$\Delta\omega'_k = \frac{k_{P_k}s + k_{I_k}}{s^2 + k_{P_k}s + k_{I_k}}\Delta\omega_k \tag{4.65}$$

The droop equation for the GFL IBR is given by,

$$(\Delta P_k - \Delta P_{set_k}) = -\frac{1}{m_{P_k}}\Delta\omega'_k \tag{4.66}$$

Substituting $\Delta\omega'_k$,

$$\Delta P_k - \Delta P_{set_k} = -\frac{1}{m_{P_k}}(\frac{k_{P_k}s + k_{I_k}}{s^2 + k_{P_k}s + k_{I_k}})\Delta\omega_k \tag{4.67}$$

$$\frac{1}{m_{P_k}}(k_{P_k}s + k_{I_k})\Delta\omega_k = -(s^2 + k_{P_k}s + k_{I_k})(\Delta P_k - \Delta P_{set_k}) \tag{4.68}$$

Simplifying by removing the derivatives of the constant term $(s^2\Delta P_{set_k}, k_{P_k}s\Delta P_{set_k})$,

$$\frac{k_{P_k}}{m_{P_k}}\Delta\dot{\omega}_k + \frac{k_{I_k}}{m_{P_k}}\Delta\omega_k = k_{I_k}\Delta P_{set_k} - k_{I_k}\Delta P_k - (s^2 + k_{P_k}s)\Delta P_k \tag{4.69}$$

It can be seen that the swing equation of the PLL and frequency-watt based based GFL IBR is very similar to that of a droop based GFM IBR. However, there are additional derivative terms in the right hand side which influence the dynamics of the GFL IBR and must be considered in the state space model. Replacing $\Delta P_k = -c_3\Delta\delta_{jk}$,

$$\frac{k_{P_k}}{m_{P_k}}\Delta\dot{\omega}_k + \frac{k_{I_k}}{m_{P_k}}\Delta\omega_k = k_{I_k}\Delta P_{set_k} + k_{I_k}c_3\Delta\delta_{jk} + (s^2 + k_{P_k}s)c_3\Delta\delta_{jk} \tag{4.70}$$

$$\frac{k_{P_k}}{m_{P_k}}\Delta\dot{\omega}_k + \frac{k_{I_k}}{m_{P_k}}\Delta\omega_k = k_{I_k}\Delta P_{set_k} + k_{I_k}c_3\Delta\delta_{jk} + c_3\Delta\ddot{\delta}_{jk} + k_{P_k}c_3\Delta\dot{\delta}_{jk} \tag{4.71}$$

This can be simplified by substituting, $\Delta\dot{\delta}_{jk} = \Delta\omega_j - \Delta\omega_k$,

$$\frac{k_{P_k}}{m_{P_k}}\Delta\dot{\omega}_k + \frac{k_{I_k}}{m_{P_k}}\Delta\omega_k = k_{I_k}\Delta P_{set_k} + k_{I_k}c_3\Delta\delta_{jk} + c_3(\Delta\dot{\omega}_j - \Delta\dot{\omega}_k) + k_{P_k}c_3(\Delta\omega_j - \Delta\omega_k) \tag{4.72}$$

Simplifying by collecting terms,

$$(\frac{k_{P_k}}{m_{P_k}} + c_3)\Delta\dot{\omega}_k + (\frac{k_{I_k}}{m_{P_k}} + k_{P_k}c_3)\Delta\omega_k = k_{I_k}\Delta P_{set_k} + k_{I_k}c_3\Delta\delta_{jk} + c_3\Delta\dot{\omega}_j + k_{P_k}c_3\Delta\omega_j \quad (4.73)$$

Substituting for $\Delta\dot{\omega}_j = -\frac{D_j}{H_j}\Delta\omega_j + \frac{1}{H_j}\Delta P_{set_j} + \frac{c_{21}}{H_j}\Delta\delta_{ij} + \frac{c_{22}}{H_j}\Delta\delta_{jk}$,

$$\begin{aligned}(\frac{k_{P_k}}{m_{P_k}} + c_3)\Delta\dot{\omega}_k + (\frac{k_{I_k}}{m_{P_k}} + k_{P_k}c_3)\Delta\omega_k &= k_{I_k}\Delta P_{set_k} + k_{I_k}c_3\Delta\delta_{jk} + \\ c_3(-\frac{D_j}{H_j}\Delta\omega_j + \frac{1}{H_j}\Delta P_{set_j} + \frac{c_{21}}{H_j}\Delta\delta_{ij} + \frac{c_{22}}{H_j}\Delta\delta_{jk}) &+ k_{P_k}c_3\Delta\omega_j \quad (4.74)\end{aligned}$$

Collecting terms and simplifying,

$$\begin{aligned}(\frac{k_{P_k}}{m_{P_k}} + c_3)\Delta\dot{\omega}_k + (\frac{k_{I_k}}{m_{P_k}} + k_{P_k}c_3)\Delta\omega_k &= \frac{c_{21}c_3}{H_j}\Delta\delta_{ij} + (k_{I_k}c_3 + \frac{c_{22}c_3}{H_j})\Delta\delta_{jk} \\ &+ (k_{P_k}c_3 - \frac{c_3D_j}{H_j})\Delta\omega_j + k_{I_k}\Delta P_{set_k} + \frac{c_3}{H_j}\Delta P_{set_j} \quad (4.75)\end{aligned}$$

Let $a_k = \frac{k_{P_k}}{m_{P_k}} + c_3$, this parameter on comparison with the SG swing equation is similar to the inertia parameter. This virtual inertia parameter will be used to validate this proposed model against a detailed model derived in [102] in the case study.

$$\begin{aligned}\Delta\dot{\omega}_k = -(\frac{k_{I_k}}{m_{P_k}a_k} + \frac{k_{P_k}c_3}{a_k})\Delta\omega_k + \frac{c_{21}c_3}{a_kH_j}\Delta\delta_{ij} + (\frac{k_{I_k}c_3}{a_k} + \frac{c_{22}c_3}{H_ja_k})\Delta\delta_{jk} \\ + (\frac{k_{P_k}c_3}{a_k} - \frac{c_3D_j}{H_ja_k})\Delta\omega_j + \frac{k_{I_k}}{a_k}\Delta P_{set_k} + \frac{c_3}{a_kH_j}\Delta P_{set_j} \quad (4.76)\end{aligned}$$

As before the SG equations can be written as,

$$\Delta\dot{\omega}_i = \frac{c_1}{M_{g,a}}\Delta\delta_{ij} - \frac{1}{M_{g,i}M_{g,a}}\frac{T_1}{T_2}\Delta\omega_i + \frac{1}{M_{g,a}}\Delta\tau_i + \frac{1}{M_{g,i}M_{g,a}}\frac{T_1}{T_2}\Delta\omega_s \quad (4.77)$$

$$\dot{\Delta\tau_i} = -\frac{1-\frac{T_1}{T_2}}{M_{g,i}T_2}\Delta\omega_i - \frac{1}{T_2}\Delta\tau_i + \frac{1-\frac{T_1}{T_2}}{M_{g,i}T_2}\Delta\omega_s \tag{4.78}$$

The equations for IBR on node j operating in the GFM mode can be written as,

$$\dot{\Delta\omega_j} = -\frac{D_j}{H_j}\Delta\omega_j + \frac{1}{H_j}\Delta P_{set_j} + \frac{c_{21}}{H_j}\Delta\delta_{ij} + \frac{c_{22}}{H_j}\Delta\delta_{jk} \tag{4.79}$$

Thus, the state space model for this system with a SG, IBR on node j operating in the GFM mode and IBR on node k operating in the GFL mode can be written as,

$$\begin{bmatrix} \dot{\Delta\delta_{ij}} \\ \dot{\Delta\delta_{jk}} \\ \dot{\Delta\omega_i} \\ \dot{\Delta\tau_i} \\ \dot{\Delta\omega_j} \\ \dot{\Delta\omega_k} \end{bmatrix} = \begin{bmatrix} 0 & 0 & 1 & 0 & -1 & 0 \\ 0 & 0 & 0 & 0 & 1 & -1 \\ \frac{c_1}{M_{g,a}} & 0 & -\frac{1}{M_{g,i}M_{g,a}}\frac{T_1}{T_2} & \frac{1}{M_{g,a}} & 0 & 0 \\ 0 & 0 & -\frac{1-\frac{T_1}{T_2}}{M_{g,i}T_2} & -\frac{1}{T_2} & 0 & 0 \\ \frac{c_{21}}{H_j} & \frac{c_{22}}{H_j} & 0 & 0 & -\frac{D_j}{H_j} & 0 \\ \frac{c_{21}c_3}{a_kH_j} & (\frac{k_{I_k}c_3}{a_k} + \frac{c_{22}c_3}{H_ja_k}) & 0 & 0 & (\frac{k_{P_k}c_3}{a_k} - \frac{c_3D_j}{H_ja_k}) & -(\frac{k_{I_k}}{m_{P_k}a_k} + \frac{k_{P_k}c_3}{a_k}) \end{bmatrix}$$

$$\begin{bmatrix} \Delta\delta_{ij} \\ \Delta\delta_{jk} \\ \Delta\omega_i \\ \Delta\tau_i \\ \Delta\omega_j \\ \Delta\omega_k \end{bmatrix} + \begin{bmatrix} 0 & 0 & 0 \\ 0 & 0 & 0 \\ \frac{1}{M_{g,i}M_{g,a}}\frac{T_1}{T_2} & 0 & 0 \\ \frac{1-\frac{T_1}{T_2}}{M_{g,i}T_2} & 0 & 0 \\ 0 & \frac{1}{H_j} & 0 \\ 0 & \frac{c_3}{a_kH_j} & \frac{k_{I_k}}{a_k} \end{bmatrix} \begin{bmatrix} \Delta\omega_s \\ \Delta P_{set_j} \\ \Delta P_{set_k} \end{bmatrix} \tag{4.80}$$

4.3.3 Case 3: SG with IBR_j Operating in the GFL Mode and IBR_k Operating in GFM Mode

Using a similar approach as before the state space model for this system can be written as,

$$\begin{bmatrix} \Delta\dot{\delta}_{ij} \\ \Delta\dot{\delta}_{jk} \\ \Delta\dot{\omega}_i \\ \Delta\dot{\tau}_i \\ \Delta\dot{\omega}_j \\ \Delta\dot{\omega}_k \end{bmatrix} = \begin{bmatrix} 0 & 0 & 1 & 0 & -1 & 0 \\ 0 & 0 & 0 & 0 & 1 & -1 \\ \frac{c_1}{M_{g,a}} & 0 & -\frac{1}{M_{g,i}M_{g,a}}\frac{T_1}{T_2} & \frac{1}{M_{g,a}} & 0 & 0 \\ 0 & 0 & -\frac{1-\frac{T_1}{T_2}}{M_{g,i}T_2} & -\frac{1}{T_2} & 0 & 0 \\ a_{j5} & a_{j6} & a_{j3} & \frac{c_{21}}{M_{g,a}} & a_{j3} & a_{j4} \\ 0 & \frac{c_3}{H_k} & 0 & 0 & 0 & -\frac{D_k}{H_k} \end{bmatrix} \begin{bmatrix} \Delta\delta_{ij} \\ \Delta\delta_{jk} \\ \Delta\omega_i \\ \Delta\tau_i \\ \Delta\omega_j \\ \Delta\omega_k \end{bmatrix} + \begin{bmatrix} 0 & 0 & 0 \\ 0 & 0 & 0 \\ \frac{1}{M_{g,i}M_{g,a}}\frac{T_1}{T_2} & 0 & 0 \\ \frac{1-\frac{T_1}{T_2}}{M_{g,i}T_2} & 0 & 0 \\ \frac{c_{21}}{M_{g,i}M_{g,a}}\frac{T_1}{T_2} & k_{I_j} & -\frac{c_{22}}{H_k} \\ 0 & 0 & \frac{1}{H_k} \end{bmatrix} \begin{bmatrix} \Delta\omega_s \\ \Delta P_{set_j} \\ \Delta P_{set_k} \end{bmatrix} \quad (4.81)$$

where $a_{j1} = (\frac{k_{P_j}}{m_{P_j}} + c_{21} - c_{22})$, $a_{j2} = -\frac{1}{a_{j1}}(\frac{k_{I_j}}{m_{P_j}} + c_{21}k_{P_j} - c_{22}k_{P_j})$, $a_{j3} = \frac{1}{a_{j1}}(c_{21}k_{P_j} - \frac{c_{21}}{M_{g,i}M_{g,a}}\frac{T_1}{T_2})$, $a_{j4} = \frac{1}{a_{j1}}(\frac{c_{22}D_k}{H_k} - c_{22}k_{P_j})$, $a_{j5} = \frac{1}{a_{j1}}(k_{I_j}c_{21} + \frac{c_1c_{21}}{M_{g,a}})$, $a_{j6} = \frac{1}{a_{j1}}(k_{I_j}c_{22} - \frac{c_{22}c_3}{H_k})$.

4.3.4 Case 4: SG with Both IBR_j and IBR_k Operating in GFL Mode

In this fourth case, the IBRs on buses j and k are operating in the GFL mode. Using a similar approach as shown in cases 1 and 2, the state space model for this system is,

$$\begin{bmatrix} \Delta\dot{\delta}_{ij} \\ \Delta\dot{\delta}_{jk} \\ \Delta\dot{\omega}_i \\ \Delta\dot{\tau}_i \\ \Delta\dot{\omega}_j \\ \Delta\dot{\omega}_k \end{bmatrix} = \begin{bmatrix} 0 & 0 & 1 & 0 & -1 & 0 \\ 0 & 0 & 0 & 0 & 1 & -1 \\ \frac{c_1}{M_{g,a}} & 0 & -\frac{1}{M_{g,i}M_{g,a}}\frac{T_1}{T_2} & \frac{1}{M_{g,a}} & 0 & 0 \\ 0 & 0 & -\frac{1-\frac{T_1}{T_2}}{M_{g,i}T_2} & -\frac{1}{T_2} & 0 & 0 \\ a'_{j4} & a'_{j5} & a'_{j2} & a'_{j8} & a'_{j1} & a'_{j3} \\ a_{k5} & a_{k6} & a_{k3} & a_{k8} & a_{k4} & a_{k2} \end{bmatrix} \begin{bmatrix} \Delta\delta_{ij} \\ \Delta\delta_{jk} \\ \Delta\omega_i \\ \Delta\tau_i \\ \Delta\omega_j \\ \Delta\omega_k \end{bmatrix} + \begin{bmatrix} 0 & 0 & 0 \\ 0 & 0 & 0 \\ \frac{1}{M_{g,i}M_{g,a}}\frac{T_1}{T_2} & 0 & 0 \\ \frac{1-\frac{T_1}{T_2}}{M_{g,i}T_2} & 0 & 0 \\ a'_{j9} & a'_{j7} & a'_{j6} \\ a_{k9} & a_{k7} & a_{k10} \end{bmatrix} \begin{bmatrix} \Delta\omega_s \\ \Delta P_{set_j} \\ \Delta P_{set_k} \end{bmatrix} \quad (4.82)$$

where, $a_{j1} = (\frac{k_{P_j}}{m_{P_j}} + c_{21} - c_{22})$; $a_{j2} = -\frac{1}{a_{j1}}(\frac{k_{I_j}}{m_{P_j}} + c_{21}k_{P_j} - c_{22}k_{P_j})$; $a_{j3} = \frac{1}{a_{j1}}(c_{21}k_{P_j} - \frac{c_{21}}{M_{g,i}M_{g,a}}\frac{T_1}{T_2})$; $a_{j4} = \frac{-c_{22}k_{P_j}}{a_{j1}}$; $a_{j5} = -\frac{c_{22}}{a_{j1}}$; $a_{j6} = \frac{1}{a_{j1}}(k_{I_j}c_{21} + \frac{c_1c_{21}}{M_{g,a}})$; $a_{j7} = \frac{k_{I_j}c_{22}}{a_{j1}}$; $a_{j8} = \frac{k_{I_j}}{a_{j1}}$; $a_{j9} = \frac{c_{21}}{M_{g,a}a_{j1}}$; $a_{j10} = \frac{c_{21}}{a_{j1}M_{g,i}M_{g,a}}\frac{T_1}{T_2}$; $a_{k1} = (\frac{k_{P_k}}{m_{P_k}} + c_3 + c_3a_{j5})$, $a_{k2} = -\frac{1}{a_{k1}}(\frac{k_{I_k}}{m_{P_k}} + c_3k_{P_k} + c_3a_{j4})$, $a_{k3} = \frac{c_3a_{j3}}{a_{k1}}$, $a_{k4} = \frac{1}{a_{k1}}(c_3k_{P_k} + c_3a_{j2})$, $a_{k5} = \frac{c_3a_{j6}}{a_{k1}}$, $a_{k6} = \frac{1}{a_{k1}}(k_{I_k}c_3 + c_3a_{j7})$, $a_{k7} = \frac{c_3a_{j8}}{a_{k1}}$, $a_{k8} = \frac{c_3a_{j9}}{a_{k1}}$, $a_{k9} = \frac{c_3a_{j10}}{a_{k1}}$; $a_{k10} = \frac{k_{I_k}}{a_{k1}}$; $a'_{j1} = (a_{j2} + a_{j5}a_{k4})$, $a'_{j2} = (a_{j3} + a_{j5}a_{k3})$, $a'_{j3} = (a_{j4} + a_{j5}a_{k2})$, $a'_{j4} = (a_{j6} + a_{k5}a_{j5})$, $a'_{j5} = (a_{j7} + a_{j5}a_{k6})$, $a'_{j6} = a_{j5}a_{k10}$, $a'_{j7} = (a_{j8} + a_{j5}a_{k7})$, $a'_{j8} = (a_{j9} + a_{j5}a_{k8})$, $a'_{j9} = (a_{j10} + a_{j5}a_{k9})$.

4.4 Case Study

In this case study, the proposed approach of using switched linear systems concepts to maintain the stability and controllability of microgrids as summarized in Fig. 4.5 is validated.

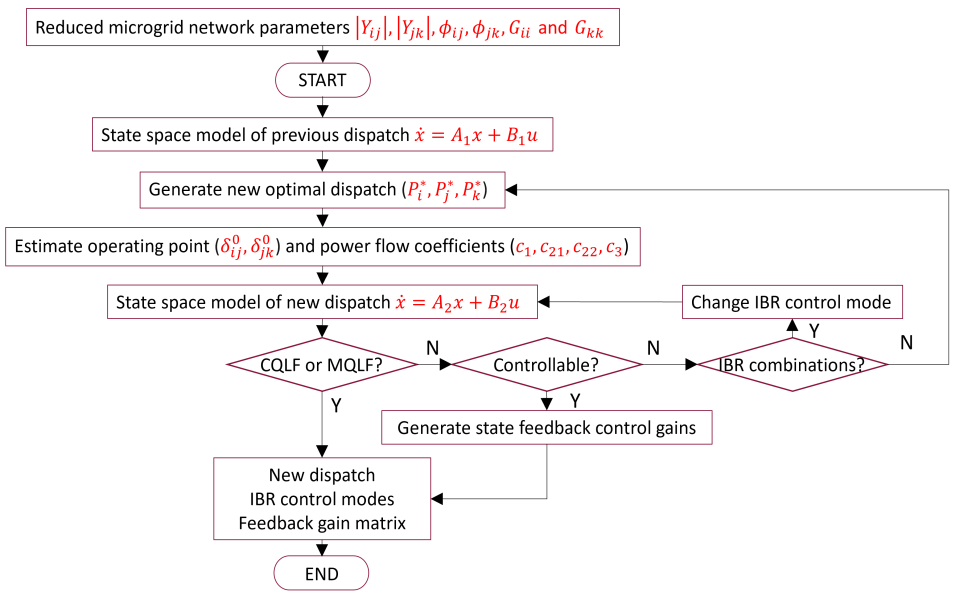

Figure 4.5: Flow chart summarizing proposed approach for ensuring microgrid stability and controllability

4.4.1 Validation of Proposed GFM and GFL IBR Models

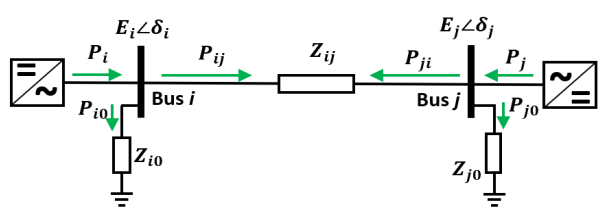

Figure 4.6: 2-bus system for validation of proposed GFL and GFM models

While the SG and first order GFM mode IBR models exist for some time now, widely accepted GFL models do not. A second order GFL model has been derived here. It is

thus essential to validate this model against detailed GFL models proposed before. The interactions between GFM and GFL IBRs using a two-bus system and higher order IBR models has been presented in [102]. For the 2-bus system shown in Fig. 4.6, a state space model is thus created using the proposed approach. The IBR on node i is operating in the GFM mode and the IBR on node j is operating in the GFL mode.

GFM-GFL model:

$$\begin{bmatrix} \Delta\dot{\delta}_{ij} \\ \Delta\dot{\omega}_i \\ \Delta\dot{\omega}_j \end{bmatrix} = \begin{bmatrix} 0 & 1 & -1 \\ \frac{c_1}{H_i} & -\frac{D_i}{H_i} & 0 \\ \frac{1}{a_j}(k_{I_j}c_2 + \frac{c_1 c_2}{H_i}) & \frac{1}{a_j}(k_{P_j}c_2 - \frac{c_2 D_i}{H_i}) & -\frac{1}{a_j}(\frac{k_{I_j}}{m_{P_j}} + k_{P_j}c_2) \end{bmatrix} \begin{bmatrix} \Delta\delta_{ij} \\ \Delta\omega_i \\ \Delta\omega_j \end{bmatrix} + \begin{bmatrix} 0 & 0 \\ \frac{1}{H_i} & 0 \\ \frac{1}{a_j}\frac{c_2}{H_i} & \frac{k_{I_j}}{a_j} \end{bmatrix} \begin{bmatrix} \Delta P_{set_i} \\ \Delta P_{set_j} \end{bmatrix} \quad (4.83)$$

Here, $c_1 = -|Y_{ij}|sin(\delta_{ij}^0 - \phi_{ij})$, $c_2 = -Y_{ij}|sin(\delta_{ij}^0 + \phi_{ij})$, and the virtual inertia term is $a_j = \frac{k_{P_j}}{m_{P_j}} + c_2(Y_{ij}, \delta_{ij}^0)$. A similar virtual inertia term $M = 1 - K_p i_d^* L_l$ was also determined in [102] and a Hamiltonian based stability criterion was proposed which requires $M > 0$. Comparing a_j and M it can be seen that both are a function of K_p, the PLL's proportional gain, system impedance (Y_{ij}, L_l), and the GFL penetration based on provided references (i_d^*, δ_{ij}^0) since δ_{ij}^0 is determined based on optimal real power references as described previously. Grid supportive frequency-watt function is not used in [102], thus m_{P_j} does not appear in M. To validate this, simulations were run for different K_p and K_I values by increasing the GFL penetration level and the system stability using the eigenvalues and controllability using controllability matrix were evaluated as shown in Fig. 4.7. It can be seen that this system becomes unstable as soon as $a_j \leq 0$ similar to the $M > 0$ requirement obtained from detailed models in [102]. It can also be seen that even when the system becomes unstable it

stays controllable. A control input can thus be designed to stabilize this 2-bus system. This suggests that evaluating controllability in addition to stability is also essential.

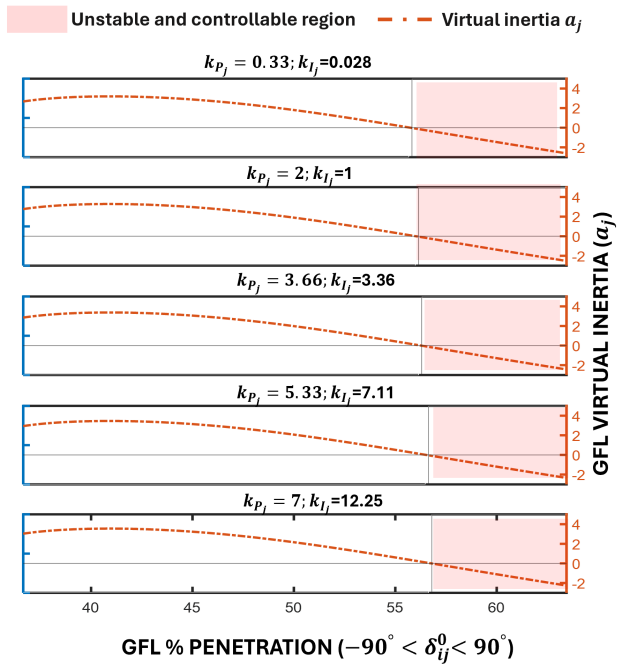

Figure 4.7: Simulation to validate proposed GFM and GFL models

4.4.2 Validation of Proposed approach on Detailed Microgrid Model

After validating the proposed reduced order IBR models against higher order IBR models, the proposed switched linear systems stability approach to ensure stability of the microgrid during planned transitions to new optimal dispatches is validated. The unbalanced 13-node feeder model as a microgrid as shown in Fig. 4.1 has been used here. The microgrid is operated in the islanded mode throughout the case study. The 3 MW SG has been modeled using the detailed 7th order generator model with standard primary controllers such as the steam turbine governor (TGOV1) and simplified excitation system (SEXS) models [113]. Detailed GFM and GFL mode IBR models as presented in [56] have been used for the 2

MW IBRs. This model was developed in Simulink and optimal power flow was solved in Python using the optimization package PYOMO and the GLPK solver. The optimal power flow output was sent to Simulink to determine the impact on microgrid dynamics.

First the reduced order model is required. In order to get this model, 5 optimal power flow solutions were obtained while constraining generation of IBR_k from 20% to 100% of its rated capacity in a 20% step size. The generated set points, and the measured steady state terminal real power and angle values for the 20% simulation case are shown in Table 4.1 as an example. It can be seen that the set points generated through linearized optimal power flow described in chapter 2 results in steady state terminal powers and voltages which are very close to the set points. This validates its accuracy. Secondly, all terminal voltages are close to 1p.u. or 2.4kV which validates the second assumption made while deriving the power flow equations and state space models.

Table 4.1: Optimal set points and terminal measurements for 20% simulation

Parameter	SG_i	IBR_j	IBR_k
OPF P set point (MW)	2.25	0.639	0.399
OPF Q set point (MVar)	0	1.24	0.655
OPF V set point (kV)	2.37	2.37	2.35
Time aligned terminal P measured	2.28	0.666	0.426
Time aligned terminal V measured	2.38	2.38	2.36
Time aligned terminal V angles of phase a (δ^{ϕ_a})	$-46.88°$	$-48.95°$	$-49.17°$

These 5 simulations only need to be performed once. Using these measured terminal powers and angles, we get estimates for $|Y_{ij}|, |Y_{jk}|, \phi_{ij}, \phi_{jk}, G_{ii}$ and G_{kk} as described before. The approximate operating point $(\delta^0_{ij}, \delta^0_{jk})$ for any given optimal dispatch (P^*_i, P^*_j, P^*_k) can now be evaluated using,

$$\delta^0_{ij} = acos((G_{ii} - P^*_i)/|Y_{ij}|) + \phi_{ij} \tag{4.84}$$

$$\delta_{jk}^0 = acos((G_{kk} - P_k^*)/|Y_{jk}|) - \phi_{jk} \tag{4.85}$$

Once the operating point estimates have been obtained, the power flow coefficients defined above can be obtained using, $c_1 = -|Y_{ij}|sin(\delta_{ij}^0 - \phi_{ij})$, $c_{21} = -|Y_{ij}|sin(\delta_{ij}^0 + \phi_{ij})$, $c_{22} = -|Y_{jk}|sin(\delta_{jk}^0 - \phi_{jk})$, and $c_3 = -|Y_{jk}|sin(\delta_{jk}^0 + \phi_{jk})$. These reduced microgrid network parameters will be used for populating the state space models.

With the reduced network available the proposed theoretical switched systems based approach can be validated. It is well known that switching IBRs from the GFL mode to GFM mode generally increases small-signal system stability [99]. However, instability between GFM IBRs has also been reported [102]. Thus a worst case scenario had to be created which can show instability even with both IBRs in the GFM mode. Since, the proposed approach allows determination of state space models for any optimal DER dispatch automatically, an iterative approach is adopted to find DER parameters and dispatch set points which satisfy the following conditions:

- The two subsystems formed by previous and new optimal dispatches are stable using both eigenvalues and the Lyapunov theorem definitions.
- The switched system formed by the two subsystems, which includes the state space models with the previous and new optimal dispatch, is unstable using both CQLF and MQLF approaches.
- The switched system is controllable using the switched controllability definition discussed before.

If such parameters and optimal dispatches can be obtained then these can be implemented in the Simulink model with the detailed higher order DER models and the complete 13-node

model. Similar results from the Simulink model as obtained from the theoretical approach will validate its effectiveness.

The optimal dispatches which satisfy these conditions are shown in Table 4.2. It can be seen that the transition from the old to new optimal dispatch represents a significant increase in IBR penetration from 45% to 65%. Thus, the previous dispatch will be referred to as the low IBR scenario and the new dispatch will be referred to as the high IBR scenario. The operating points and c_1, c_{21}, c_{22}, c_3 parameters corresponding with these operating points were determined as described above. The IBR parameters which satisfy these conditions are $T_{P_k^f} = T_{P_j^f} = 0.04sec$, and $m_{P_k} = m_{P_j} = 0.06\omega_s/p.u.$. The SG parameters are $T_1 = 0.335sec, T_2 = 0.1sec, M_{g,i} = 0.065\omega_s/p.u., H_{g,a} = 2.6s/p.u., M_{g,a} = 2H_{g,a}/\omega_s$.

Table 4.2: Optimal set points for previous and new dispatches

Parameter	SG_i	IBR_j	IBR_k
Previous OPF P set point (MW)	1.8	0.49	0.999
Previous OPF Q set point (MVar)	1.2	0.704	0
Previous OPF V set point (kV)	2.39	2.34	2.34
New OPF P set point (MW)	1.2	0.187	1.903
New OPF Q set point (MVar)	1.87	0.996	-0.969
New OPF V set point (kV)	2.4	2.34	2.34

The subsystems corresponding to low and high IBR dispatches are denoted as $\dot{x} = A_1x + B_1u$ and $\dot{x} = A_2x + B_2u$ respectively. The state space models developed in case 1 were used here. The eigenvalue with the largest real part was -1.03 for A_1 and -0.5 for A_2. Thus the individual systems are stable. The Lyapunov definition was also applied by solving the LMIs $A_1^T L_1 + L_1 A_1 < 0$ and $A_2^T L_2 + L_2 A_2 < 0$. While solving these LMIs using YALMIP and SeDuMi, a constraint $trace(L) == 1$ is added to avoid having a positive definite matrix L with values close to zero [91]. Positive definite L_1 and L_2 matrices could be found. Thus the individual systems for low and high IBR penetration with both GFM IBRs are stable using

the theoretical approach. The same parameters and DER dispatches were then implemented in the Simulink model. All other network and DER parameters which are not a part of the state space models stay constant for all simulations. It can be seen in Figures 4.8 and 4.9 that the microgrid frequency stays at 60 Hz and all DERs reach the desired set points as shown in Table 4.2 for individual subsystem corresponding to low and high IBR penetration levels.

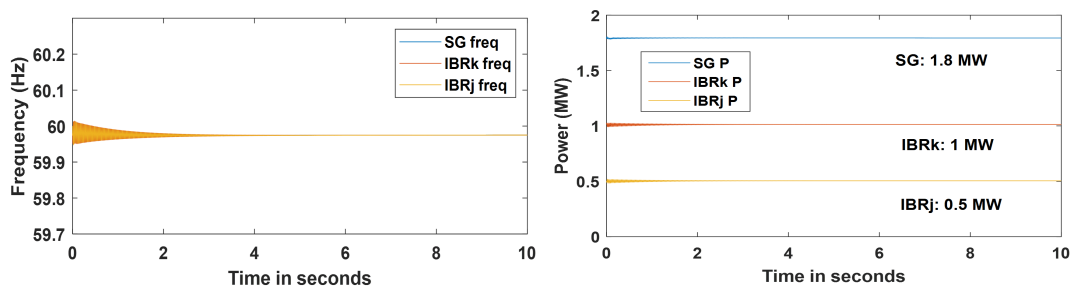

Figure 4.8: Detailed Simulink simulation results show low IBR scenario is stable.

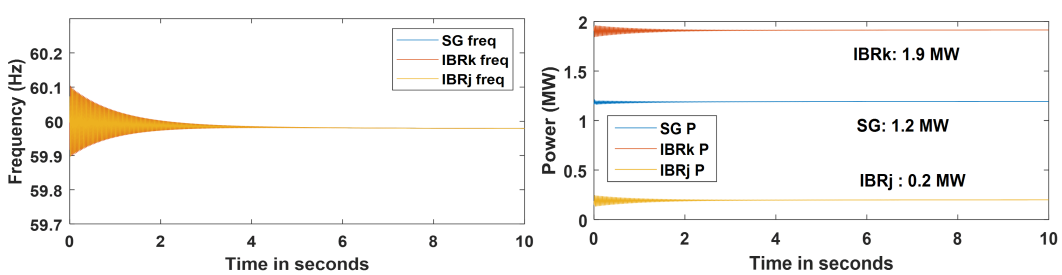

Figure 4.9: Detailed Simulink simulation results show high IBR scenario is stable.

Next CQLF was evaluated for this 2 subsystem switched microgrid. The LMIs solved for calculating CQLF were $A_1^T L + LA_1 < 0$ and $A_2^T L + LA_2 < 0$. However, a positive definite L matrix could not be found and SeDuMi ran into numerical problems. However, as mentioned before the CQLF can be conservtaive. So, MQLF was also determined by solving the following LMIs with a dwell time $T_d = 20sec$. However, positive definite L_1 and L_2 matrices could not be found and SeDuMi ran into numerical problems. Simulink simulation was then run which starts with the low IBR dispatches applied from the start as shown in Fig. 4.10.

The systems remains stable. Then at $t = 10sec$, the high IBR penetration dispatches are applied. It can be seen that the system becomes unstable and cannot switch or transition to this high IBR scenario as suggested by the theoretical approach.

$$A_1^T L_1 + L_1 A_1 < 0 \tag{4.86}$$

$$A_2^T L_2 + L_2 A_2 < 0 \tag{4.87}$$

$$e^{A_1^T T_d} L_2 e^{A_1 T_d} - L_1 < 0 \tag{4.88}$$

$$e^{A_2^T T_d} L_1 e^{A_2 T_d} - L_2 < 0 \tag{4.89}$$

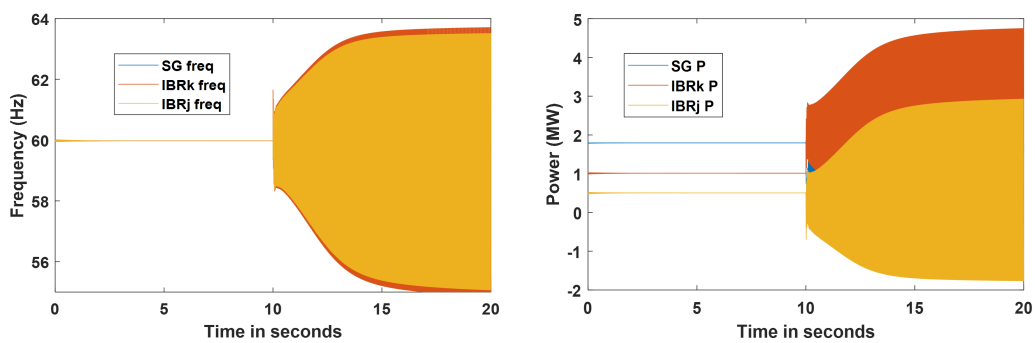

Figure 4.10: Detailed Simulink simulation results show transtion from low to high IBR scenario is unstable.

However, even if the system is unstable, it can be stabilized using a control signal as long as it is controllable. Thus, controllability of the two subsystem switched system was determined. This was done by determining the cyclic invariant susbpaces as mentioned before. The first subspace was determined as shown below. This switched system will be controllable if $rank(U_6) = 6$ or $dim(U_6) = 6$ and $U_1 \subset U_2 \subset ... \subset U_6$. Thus if $rank(U_1) = 6$, then $rank(U_6) = 6$. In this case $rank(U_1) = 6$, as 6 linearly independent vectors could be found

in the span of vectors shown below. Thus the switched system is controllable and only the first subspace had to be evaluated, thereby, significantly reducing the computational burden.

$$U_1 = \sum_{i=1}^{2} \langle A_i | B_i \rangle = \langle A_1 | B_1 \rangle + \langle A_2 | B_2 \rangle \tag{4.90}$$

$$rank(U_1) = rank(\langle A_1 | B_1 \rangle + \langle A_2 | B_2 \rangle) \tag{4.91}$$

$$rank(U_1) = span(B_1, A_1B_1, A_1^2B_1, A_1^3B_1, A_1^4B_1, A_1^5B_1, B_2, A_2B_2, A_2^2B_2, A_2^3B_2, A_2^4B_2, A_2^5B_2) \tag{4.92}$$

To validate this feedback control gain matrix was created using the approach presented in [100]. It can be seen in Fig. 4.11 that using this control signal the transition to the higher IBR scenario is stabilized. The results from the unstable case without any feedback control are also shown in this figure for comparison. This validates the proposed approach of stabilizing the switched microgrid system using control input signals after determining its controllability.

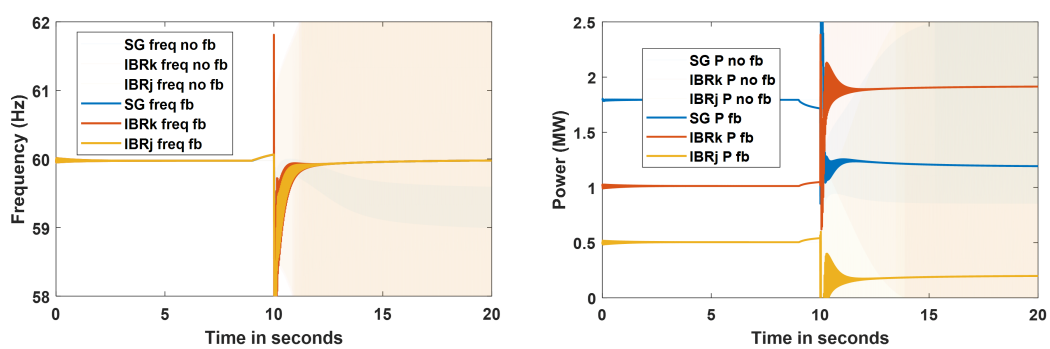

Figure 4.11: Detailed Simulink simulation results show transtion from low to high IBR scenario can be stabilized using state feedback control signals if it is controllable.

However, designing feedback control can increase cost due to the need for low latency communication requirements. An alternative approach can be to switch the control mode of

one of the IBRs. Thus while the first subsystem was kept the same as before, the second subsystem is now updated using the state space model developed in case 2 where IBR_k is switched from GFM to the GFL mode and the parameters are determined using the new OPF dispatch. This new subsystem was found to stable using eigenvalues and Lyapunov definitions. At the same time positive definite matrices could be found for both CQLF and MQLF for the switched microgrid system. For the Simulik simulation for this use case, the GFL IBR model and parameters as given in [56] were used for IBR_k. The same PLL parameters were used in the state space model. Feedback control has not been used. It can be seen in Fig. 4.12 that the microgrid can easily transition from low to high IBR dispatches after switching IBR_k to GFL mode as suggested by the theoretical approach. The results from the unstable case with both GFM IBRs are also shown in this figure for comparison. This validates the effectiveness of the proposed theoretical approach in maintaining the stability and controllability of microgrids during restoration and optimal dispatch.

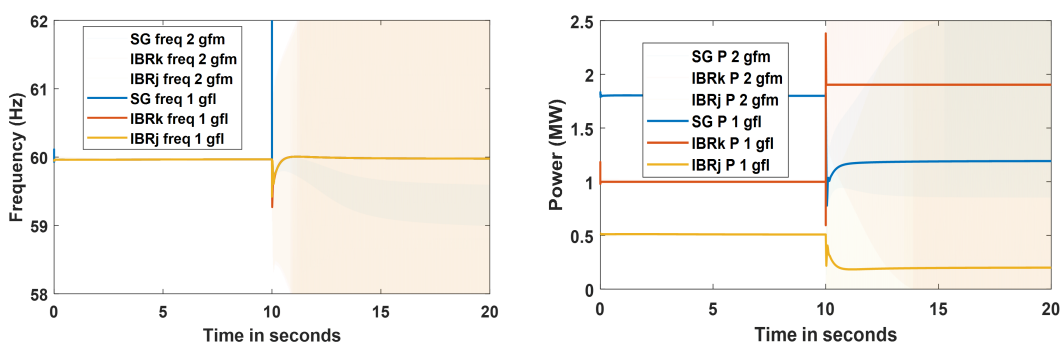

Figure 4.12: Detailed Simulink simulation results show stable transtion from low to high IBR scenario after switching control mode of IBR_k to GFL.

Chapter 5

Conclusions and Future Work

The research presented in this dissertation is focused on resilience enhancement of the electric grid by enabling time and cost effective deployment of microgrids. This has been achieved through the development of a novel methodology which allows reliable and secure integration of the various dynamical systems and dispatch and control algorithms required for the operation of a microgrid in both the grid-connected and islanded modes of operation.

5.1 Conclusions

A microgrid is a non-linear controlled dynamical system. Managing the interactions among inverter based resources (IBRs) with low inertia and conventional generators with slower rates of response, especially in the islanded mode of operation is a challenging task. Current research on primary IBR controllers typically include an infinite bus while evaluating stability. In the limited research where an it is not considered, small microgrids which do not adequately consider power flow equations and the impact of network parameters are used.
A comprehensive approach is thus needed which can determine the non-linear controllability

of microgrids. Controllability refers to the ability to steer the microgrid from any initial state to any final state within finite time. The research presented in this dissertation is a significant step forward in this direction where the microgrid is modeled as a nonlinear system while including network parameters and power flow equations. This nonlinear model consists of the linearized state space models and the discrete switching between these models during optimal dispatch and sequential microgrid restoration.

Cybersecurity is ensured by determining attack models that may be used to falsify control commands on a three-phase unbalanced optimal power flow based distributed energy resource management system. Cyber layer based centralized, and inverter based de-centralized intrusion detection techniques are also developed. Case studies using detailed cyber-physical system models show that these cyberattacks have the potential to impact and damage all the nodes in the microgrid. This study also highlights that, unlike currently used strategies which may allow power systems layer to be impacted, the proposed techniques could mitigate these attacks within the cyber layer.

An approach to reducing time and cost of deployment of microgrids is to not depend on communications and remote control capabilities. The integrated approach proposed in this dissertation mitigates the need for adding such capabilities in unmonitored automatic voltage regulation devices and net-metered (NM) loads by incorporating their time dependent behavior in a sequential optimal microgrid restoration algorithm. This approach allows coordinated optimal control of dispatchable distributed energy resources with non-remote control capable voltage regulation devices. The proposed disaggregated NM load demand model is shown to accurately forecast NM load demand during all time steps of the microgrid restoration process.

Algorithms for controlling microgrid dynamics such as state feedback control have been proposed. However, these algorithms can stabilize the microgrid only if it is controllable. These algorithms may also not work satisfactorily if the operating point changes significantly such

as when a new optimal dispatch is applied. To adddress this critical issue, an approach leveraging switched linear systems theory is developed which can determine the stability and controllability of the microgrid as it transitions to the new optimal dispatch. The developed reduced order models validated against higher order models, reduce computational burden and enable real time operation. This approach also provides the correct control mode, grid forming or following, of inverter based resources during the transition to the new optimal dispatch. This increases the number of options available for ensuring stable microgrid operation, without the need for deploying additional control and communications infrastructure.

5.2 Future Work

In the proposed approach, after the cyberattacks have been detected, they are mitigated by dropping the malicious data packets and operating the inverters in localized control mode. This, however, is not desirable as localized control may be sub-optimal. Future work would thus look at methods to recover the legitimate control command data packets and securely communicate them to the inverters.

In the proposed microgrid service restoration approach, voltage drops across voltage regulators are ignored and simplified power flow relations are used to reduce computation time. This, however, can reduce accuracy which can be further improved by using power flow formulations that consider coupling among phases. While the proposed approach can determine the stability and controllability of the microgrid during planned transitions, future work would also include integration of optimization and control algorithms for managing dynamics that arise due to unplanned transitions. This integrated approach should be validated using real-time simulations to further validate its effectiveness.

Bibliography

[1] K. Li, J. Yan, L. Hu, F. Wang, and N. Zhang, "Two-Stage Decoupled Estimation Approach of Aggregated Baseline Load Under High Penetration of Behind-the-Meter PV System," *IEEE Transactions on Smart Grid*, vol. 12, no. 6, pp. 4876–4885, 2021.

[2] C.-C. Liu *et al.*, "Microgrid building blocks: Concept and feasibility," *IEEE Open Access Journal of Power and Energy*, vol. 10, pp. 463–476, 2023.

[3] S. Cai, Y. Xie, Q. Wu, M. Zhang, X. Jin, and Z. Xiang, "Distributionally Robust Microgrid Formation Approach for Service Restoration Under Random Contingency," *IEEE Transactions on Smart Grid*, vol. 12, no. 6, pp. 4926–4937, 2021.

[4] Y. Yao, F. Ding, K. Horowitz, and A. Jain, "Coordinated inverter control to increase dynamic PV hosting capacity: A real-time optimal power flow approach," *IEEE Systems Journal*, pp. 1–12, 2021.

[5] E. Dall'Anese, S. V. Dhople, and G. B. Giannakis, "Optimal dispatch of photovoltaic inverters in residential distribution systems," *IEEE Transactions on Sustainable Energy*, vol. 5, no. 2, pp. 487–497, 2014.

[6] A. Teymouri, A. Mehrizi-Sani, and C. C. Liu, "Cyber security risk assessment of solar PV units with reactive power capability," in *IECON 2018-44th Annual Conference of the IEEE Industrial Electronics Society*. IEEE, 2018, pp. 2872–2877.

[7] J. Johnson, J. Quiroz, R. Concepcion, F. Wilches-Bernal, and M. J. Reno, "Power system effects and mitigation recommendations for DER cyberattacks," *IET Cyber-Physical Systems: Theory & Applications*, vol. 4, no. 3, pp. 240–249, 2019.

[8] Y. Isozaki, S. Yoshizawa, Y. Fujimoto, H. Ishii, I. Ono, T. Onoda, and Y. Hayashi, "Detection of cyber attacks against voltage control in distribution power grids with PVs," *IEEE Transactions on Smart Grid*, vol. 7, no. 4, pp. 1824–1835, 2015.

[9] W. H. Kersting, *Distribution System Modeling and Analysis*. Third Edition, 2012.

[10] J. Appiah-Kubi and C. C. Liu, "Decentralized intrusion prevention (DIP) against co-ordinated cyberattacks on distribution automation systems," *IEEE Open Access Journal of Power and Energy*, vol. 7, pp. 389–402, 2020.

[11] Q. Dai, L. Shi, and Y. Ni, "Risk assessment for cyberattack in active distribution systems considering the role of feeder automation," *IEEE Transactions on Power Systems*, vol. 34, no. 4, pp. 3230–3240, 2019.

[12] M. Chlela, D. Mascarella, G. Joos, and M. Kassouf, "Fallback control for isochronous energy storage systems in autonomous microgrids under denial-of-service cyber-attacks," *IEEE Transactions on Smart Grid*, vol. 9, no. 5, pp. 4702–4711, 2017.

[13] D. Jafarigiv, K. Sheshyekani, M. Kassouf, Y. Seyedi, H. Karimi, and J. Mahseredjian, "Countering FDI attacks on DERs coordinated control system using FMI-compatible cosimulation," *IEEE Transactions on Smart Grid*, vol. 12, no. 2, pp. 1640–1650, 2021.

[14] D. Wang, X. Wang, Y. Zhang, and L. Jin, "Detection of power grid disturbances and cyber-attacks based on machine learning," *Journal of Information Security and Applications*, vol. 46, pp. 42–52, 2019.

[15] Q. Li, F. Li, J. Zhang, J. Ye, W. Song, and A. Mantooth, "Data-driven cyberattack detection for photovoltaic (PV) systems through analyzing micro-PMU data," in *2020 IEEE Energy Conversion Congress and Exposition (ECCE)*. IEEE, 2020, pp. 431–436.

[16] C. B. Jones, A. R. Chavez, R. Darbali-Zamora, and S. Hossain-McKenzie, "Implementation of intrusion detection methods for distributed photovoltaic inverters at the grid-edge," in *2020 IEEE Power Energy Society Innovative Smart Grid Technologies Conference (ISGT)*, 2020, pp. 1–5.

[17] C. B. Jones, A. Chavez, S. Hossain-McKenzie, N. Jacobs, A. Summers, and B. Wright, "Unsupervised online anomaly detection to identify cyber-attacks on internet connected photovoltaic system inverters," in *2021 IEEE Power and Energy Conference at Illinois (PECI)*, 2021, pp. 1–7.

[18] M. J. Assante and R. M. Lee, "The industrial control system cyber kill chain," *SANS Institute InfoSec Reading Room*, vol. 1, 2015.

[19] A. Stefanov, C. C. Liu, M. Govindarasu, and S.-S. Wu, "SCADA modeling for performance and vulnerability assessment of integrated cyber–physical systems," *International Transactions on Electrical Energy Systems*, vol. 25, no. 3, pp. 498–519, 2015.

[20] B. Palmintier, D. Krishnamurthy, P. Top, S. Smith, J. Daily, and J. Fuller, "Design of the HELICS high-performance transmission-distribution-communication-market co-simulation framework," in *2017 Workshop on Modeling and Simulation of Cyber-Physical Energy Systems (MSCPES)*. IEEE, 2017, pp. 1–6.

[21] M. Bellare, J. Kilian, and P. Rogaway, "The security of the cipher block chaining message authentication code," *Journal of Computer and System Sciences*, vol. 61, no. 3, pp. 362–399, 2000.

[22] T. J. Sargent and J. Stachurski, "Linear regression in python," 2020.

[23] X. Yang, C. Xu, J. Wen, Y. Zhang, Q. Wu, W. Zuo, and S. Cheng, "Cooperative Repair Scheduling and Service Restoration for Distribution Systems with Soft Open Points," *IEEE Transactions on Smart Grid*, vol. 14, no. 3, pp. 1827–1842, 2023.

[24] S. Poudel and A. Dubey, "Critical Load Restoration Using Distributed Energy Resources for Resilient Power Distribution System," *IEEE Transactions on Power Systems*, vol. 34, no. 1, pp. 52–63, 2019.

[25] A. S. Alahmed and L. Tong, "On Net Energy Metering X: Optimal Prosumer Decisions, Social Welfare, and Cross-Subsidies," *IEEE Transactions on Smart Grid*, vol. 14, no. 2, pp. 1652–1663, 2023.

[26] M. Farrokhabadi *et al.*, "Microgrid Stability Definitions, Analysis, and Examples," *IEEE Transactions on Power Systems*, vol. 35, no. 1, pp. 13–29, 2020.

[27] M. J. Reno, S. Brahma, A. Bidram, and M. E. Ropp, "Influence of Inverter-Based Resources on Microgrid Protection: Part 1: Microgrids in Radial Distribution Systems," *IEEE Power and Energy Magazine*, vol. 19, no. 3, pp. 36–46, 2021.

[28] W. H. Kersting, *Distribution System Modeling and Analysis*. Fourth Edition, CRC Press, 2017.

[29] T. Stetz, K. Diwold, M. Kraiczy, D. Geibel, S. Schmidt, and M. Braun, "Techno-Economic Assessment of Voltage Control Strategies in Low Voltage Grids," *IEEE Transactions on Smart Grid*, vol. 5, no. 4, pp. 2125–2132, 2014.

[30] M. Lave, M. J. Reno, and R. J. Broderick, "Characterizing Local High-Frequency Solar Variability and its Impact to Distribution Studies," *Solar Energy*, vol. 118, pp. 327–337, 2015.

[31] M. J. Reno, M. Lave, J. E. Quiroz, and R. J. Broderick, "PV Ramp Rate Smoothing Using Energy Storage to Mitigate Increased Voltage Regulator Tapping," in *2016 IEEE 43rd Photovoltaic Specialists Conference (PVSC)*, 2016, pp. 2015–2020.

[32] H. M. Maruf and B. H. Chowdhury, "Impact of Smart Inverter Functions on Dynamic Step Voltage Regulator Settings for Distribution Voltage Control," in *2019 IEEE Milan PowerTech*, 2019, pp. 1–6.

[33] S. Maharjan, D. Sampath Kumar, and A. M. Khambadkone, "Enhancing the Voltage Stability of Distribution Network during PV Ramping Conditions with Variable Speed Drive Loads," *Applied Energy*, vol. 264, p. 114733, 2020.

[34] H. Sekhavatmanesh and R. Cherkaoui, "Analytical Approach for Active Distribution Network Restoration Including Optimal Voltage Regulation," *IEEE Transactions on Power Systems*, vol. 34, no. 3, pp. 1716–1728, 2019.

[35] R. Sadnan, S. Poudel, A. Dubey, and K. P. Schneider, "Layered Coordination Architecture for Resilient Restoration of Power Distribution Systems," *IEEE Transactions on Industrial Informatics*, pp. 1–1, 2022.

[36] A. Bedawy, N. Yorino, K. Mahmoud, Y. Zoka, and Y. Sasaki, "Optimal Voltage Control Strategy for Voltage Regulators in Active Unbalanced Distribution Systems Using Multi-Agents," *IEEE Transactions on Power Systems*, vol. 35, no. 2, pp. 1023–1035, 2020.

[37] K. Horowitz, "2019 Distribution System Upgrade Unit Cost Database Current Version." [Online]. Available: https://www.osti.gov/biblio/1491263

[38] S. Cai, Y. Xie, Y. Zhang, M. Zhang, Q. Wu, and J. Guo, "A Simulation-Assisted Proactive Scheduling Method for Secure Microgrid Formation Under Static and Tran-

sient Islanding Constraints," *IEEE Transactions on Smart Grid*, vol. 15, no. 1, pp. 272–285, 2024.

[39] Y. Wen, C. Y. Chung, X. Liu, and L. Che, "Microgrid Dispatch with Frequency-Aware Islanding Constraints," *IEEE Transactions on Power Systems*, vol. 34, no. 3, pp. 2465–2468, 2019.

[40] A. M. Nakiganda, S. Dehghan, U. Markovic, G. Hug, and P. Aristidou, "A Stochastic-Robust Approach for Resilient Microgrid Investment Planning under Static and Transient Islanding Security Constraints," *IEEE Transactions on Smart Grid*, vol. 13, no. 3, pp. 1774–1788, 2022.

[41] M. Javadi, Y. Gong, and C. Y. Chung, "Frequency Stability Constrained Microgrid Scheduling Considering Seamless Islanding," *IEEE Transactions on Power Systems*, vol. 37, no. 1, pp. 306–316, 2022.

[42] Y. Zhang, C. Chen, G. Liu, T. Hong, and F. Qiu, "Approximating Trajectory Constraints with Machine Learning – Microgrid Islanding with Frequency Constraints," *IEEE Transactions on Power Systems*, vol. 36, no. 2, pp. 1239–1249, 2021.

[43] Q. Zhang, Z. Ma, Y. Zhu, and Z. Wang, "A Two-Level Simulation-Assisted Sequential Distribution System Restoration Model with Frequency Dynamics Constraints," *IEEE Transactions on Smart Grid*, vol. 12, no. 5, pp. 3835–3846, 2021.

[44] California distributed generation statistics. accessed Jan 2023. [Online]. Available: https://www.californiadgstats.ca.gov/charts/

[45] Y. Yao, F. Ding, K. Horowitz, and A. Jain, "Coordinated Inverter Control to Increase Dynamic PV Hosting Capacity: A Real-Time Optimal Power Flow Approach," *IEEE Systems Journal*, vol. 16, no. 2, pp. 1933–1944, 2022.

[46] F. Kabir, N. Yu, W. Yao, R. Yang, and Y. Zhang, "Joint Estimation of Behind-the-Meter Solar Generation in a Community," *IEEE Transactions on Sustainable Energy*, vol. 12, no. 1, pp. 682–694, 2021.

[47] "IEEE Standard for Interconnection and Interoperability of Distributed Energy Resources with Associated Electric Power Systems Interfaces," *IEEE Std 1547-2018 (Revision of IEEE Std 1547-2003)*, pp. 1–138, 2018.

[48] K. P. Schneider, E. Sortomme, S. S. Venkata, M. T. Miller, and L. Ponder, "Evaluating the Magnitude and Duration of Cold Load Pick-up on Residential Distribution using Multi-State Load Models," *IEEE Transactions on Power Systems*, vol. 31, no. 5, pp. 3765–3774, 2016.

[49] B. Chen, C. Chen, J. Wang, and K. L. Butler-Purry, "Multi-Time Step Service Restoration for Advanced Distribution Systems and Microgrids," *IEEE Transactions on Smart Grid*, vol. 9, no. 6, pp. 6793–6805, 2018.

[50] M. Song, R. R. Nejad, and W. Sun, "Robust Distribution System Load Restoration with Time-Dependent Cold Load Pickup," *IEEE Transactions on Power Systems*, vol. 36, no. 4, pp. 3204–3215, 2021.

[51] K. Li, Y. Wang, N. Zhang, and F. Wang, "Precision and Accuracy Co-Optimization-Based Demand Response Baseline Load Estimation Using Bidirectional Data," *IEEE Transactions on Smart Grid*, vol. 14, no. 1, pp. 266–276, 2023.

[52] K. Li, F. Wang, Z. Mi, M. Fotuhi-Firuzabad, N. Duić, and T. Wang, "Capacity and Output Power Estimation Approach of Individual Behind-the-Meter Distributed Photovoltaic System for Demand Response Baseline Estimation," *Applied Energy*, vol. 253, p. 113595, 2019.

[53] T. Ding, Z. Wang, M. Qu, Z. Wang, and M. Shahidehpour, "A Sequential Black-Start Restoration Model for Resilient Active Distribution Networks," *IEEE Transactions on Power Systems*, vol. 37, no. 4, pp. 3133–3136, 2022.

[54] K. Mongird *et al.*, *Energy Storage Technology and Cost Characterization Report*. PNNL-28866. Richland, WA: Pacific Northwest National Laboratory, 2019.

[55] F. Vivas, F. Segura, J. Andújar, and J. Caparrós, "A Suitable State-space Model for Renewable Source-based Microgrids with Hydrogen as Backup for the Design of Energy Management Systems," *Energy Conversion and Management*, vol. 219, 2020.

[56] W. Du, F. K. Tuffner, K. P. Schneider, R. H. Lasseter, J. Xie, Z. Chen, and B. Bhattarai, "Modeling of grid-forming and grid-following inverters for dynamic simulation of large-scale distribution systems," *IEEE Transactions on Power Delivery*, vol. 36, no. 4, pp. 2035–2045, 2021.

[57] F. Sadeque, D. Sharma, and B. Mirafzal, "Seamless grid-following to grid-forming transition of inverters supplying a microgrid," in *2023 IEEE Applied Power Electronics Conference and Exposition (APEC)*, 2023, pp. 594–599.

[58] X. Gao, D. Zhou, A. Anvari-Moghaddam, and F. Blaabjerg, "Seamless transitions between grid-following and grid-forming control: A novel switching method," in *2023 11th International Conference on Power Electronics and ECCE Asia (ICPE 2023 - ECCE Asia)*, 2023, pp. 1154–1160.

[59] R. Decarlo, M. Branicky, S. Pettersson, and B. Lennartson, "Perspectives and results on the stability and stabilizability of hybrid systems," *Proceedings of the IEEE*, vol. 88, no. 7, pp. 1069–1082, 2000.

[60] D. Liberzon, J. P. Hespanha, and A. Morse, "Stability of switched systems:

a lie-algebraic condition," *Systems Control Letters*, vol. 37, no. 3, pp. 117–122, 1999. [Online]. Available: https://www.sciencedirect.com/science/article/pii/S0167691199000122

[61] G. Zhang, P. Zheng, S. Yu, H. Trinh, and P. Shi, "Controllability analysis and verification for high-order dc–dc converters using switched linear systems theory," *IEEE Transactions on Power Electronics*, vol. 36, no. 8, pp. 9678–9688, 2021.

[62] H. Lin and P. J. Antsaklis, "Stability and stabilizability of switched linear systems: A survey of recent results," *IEEE Transactions on Automatic Control*, vol. 54, no. 2, pp. 308–322, 2009.

[63] Opendssdirect.py. accessed Oct 2020. [Online]. Available: https://github.com/dss-extensions/OpenDSSDirect.py

[64] M. Baran and F. F. Wu, "Network reconfiguration in distribution systems for loss reduction and load balancing," *IEEE Transactions on Power Delivery*, vol. 4, no. 2, pp. 1401–1407, 1989.

[65] M. Baran and F. Wu, "Optimal sizing of capacitors placed on a radial distribution system," *IEEE Transactions on power Delivery*, vol. 4, no. 1, pp. 735–743, 1989.

[66] G. Cavraro, V. Kekatos, and S. Veeramachaneni, "Voltage analytics for power distribution network topology verification," *IEEE Transactions on Smart Grid*, vol. 10, no. 1, pp. 1058–1067, 2017.

[67] F. Tamp and P. Ciufo, "A sensitivity analysis toolkit for the simplification of MV distribution network voltage management," *IEEE Transactions on Smart Grid*, vol. 5, no. 2, pp. 559–568, 2014.

[68] ANSIStandard, "ANSI standard: Electric power systems and equipment - voltage ratings (60 Hz)," C84.1-2016.

[69] A. Gandluru, S. Poudel, and A. Dubey, "Joint estimation of operational topology and outages for unbalanced power distribution systems," *IEEE Transactions on Power Systems*, vol. 35, no. 1, pp. 605–617, 2020.

[70] X. Zhang and K. K. Parhi, "Implementation approaches for the advanced encryption standard algorithm," *IEEE Circuits and systems Magazine*, vol. 2, no. 4, pp. 24–46, 2002.

[71] R. B. J. Watt and A. K. Katsaggelos, "Machine learning refined: Foundations, algorithms, and applications," *Cambridge, U.K., Cambridge Univ. Press*, vol. 2, 2020.

[72] A. K. Jain, K. Horowitz, F. Ding, N. Gensollen, B. Mather, and B. Palmintier, "Quasi-static time-series PV hosting capacity methodology and metrics," in *2019 IEEE Power & Energy Society Innovative Smart Grid Technologies Conference (ISGT)*. IEEE, 2019, pp. 1–5.

[73] IEEEStandard, "IEEE standard for interconnection and interoperability of distributed energy resources with associated electric power systems interfaces - amendment 1," 2018.

[74] "Information technology industry council's AC voltage boundary curve for IT equipment." [Online]. Available: https://voltage-disturbance.com/voltage-quality/itic-curve/

[75] Opendssdirect.py. accessed Jan 2023. [Online]. Available: https://github.com/dss-extensions/OpenDSSDirect.py

[76] M. Baran and F. Wu, "Network Reconfiguration in Distribution Systems for Loss Reduction and Load Balancing," *IEEE Transactions on Power Delivery*, vol. 4, no. 2, pp. 1401–1407, 1989.

[77] W. Wu, Z. Tian, and B. Zhang, "An Exact Linearization Method for OLTC of Transformer in Branch Flow Model," *IEEE Transactions on Power Systems*, vol. 32, no. 3, pp. 2475–2476, 2016.

[78] H. Nagarajan, M. Lu, E. Yamangil, and R. Bent, "Tightening McCormick Relaxations for Nonlinear Programs via Dynamic Multivariate Partitioning," in *Principles and Practice of Constraint Programming*. Springer International Publishing, 2016.

[79] S. H. Low, "Convex Relaxation of Optimal Power Flow—Part i: Formulations and Equivalence," *IEEE Transactions on Control of Network Systems*, vol. 1, no. 1, pp. 15–27, 2014.

[80] J. Li, Y. Xu, Y. Wang, M. Li, J. He, C.-C. Liu, and K. P. Schneider, "Resilience-Motivated Distribution System Restoration Considering Electricity-Water-Gas Interdependency," *IEEE Transactions on Smart Grid*, vol. 12, no. 6, pp. 4799–4812, 2021.

[81] V. Kekatos, L. Zhang, G. B. Giannakis, and R. Baldick, "Voltage Regulation Algorithms for Multiphase Power Distribution Grids," *IEEE Transactions on Power Systems*, vol. 31, no. 5, pp. 3913–3923, 2016.

[82] M. K. Singh, V. Kekatos, and C.-C. Liu, "Optimal Distribution System Restoration with Microgrids and Distributed Generators," in *2019 IEEE Power Energy Society General Meeting (PESGM)*, 2019, pp. 1–5.

[83] A. Gandluru, S. Poudel, and A. Dubey, "Joint Estimation of Operational Topology and

Outages for Unbalanced Power Distribution Systems," *IEEE Transactions on Power Systems*, vol. 35, no. 1, pp. 605–617, 2020.

[84] A. K. Jain, C.-C. Liu, K. P. Schneider, F. K. Tuffner, and D. Ton, "Demand Estimation of Net Metered Loads for Microgrid Restoration," in *2023 IEEE Power Energy Society Innovative Smart Grid Technologies Conference (ISGT)*, 2023, pp. 1–5.

[85] B. Chen, C. Chen, J. Wang, and K. L. Butler-Purry, "Sequential Service Restoration for Unbalanced Distribution Systems and Microgrids," *IEEE Transactions on Power Systems*, vol. 33, no. 2, pp. 1507–1520, 2018.

[86] M.-Y. Huang *et al.*, "MILP Acceleration: A Survey from Perspectives of Simplex Initialization and Learning-Based Branch and Bound," *Journal of the Operations Research Society of China*, 2023.

[87] G. Morales-España, J. M. Latorre, and A. Ramos, "Tight and Compact MILP Formulation for the Thermal Unit Commitment Problem," *IEEE Transactions on Power Systems*, vol. 28, no. 4, pp. 4897–4908, 2013.

[88] M. Carrion and J. Arroyo, "A Computationally Efficient Mixed-Integer Linear Formulation for the Thermal Unit Commitment Problem," *IEEE Transactions on Power Systems*, vol. 21, no. 3, pp. 1371–1378, 2006.

[89] A. K. Jain, N. Sahani, and C.-C. Liu, "Detection of Falsified Commands on a DER Management System," *IEEE Transactions on Smart Grid*, vol. 13, no. 2, pp. 1322–1334, 2022.

[90] Pecan street dataport. accessed Jan 2023. [Online]. Available: https://www.pecanstreet.org/dataport/

[91] An introduction to switched systems. accessed Mar 2024. [Online]. Available: https://edisciplinas.usp.br/pluginfile.php/5357232/mod_folder/content/0/aula1_introdu%C3%A7%C3%A3o_sistemas_chaveados_2020.pdf?forcedownload=1

[92] D. Liberzon, *Switching in systems and control*. Springer, 2003, vol. 190.

[93] S. Boyd, L. El Ghaoui, E. Feron, and V. Balakrishnan, *Linear matrix inequalities in system and control theory*. SIAM, 1994.

[94] J. C. Geromel and P. Colaneri, "Stability and stabilization of continuous-time switched linear systems," *SIAM Journal on Control and Optimization*, vol. 45, no. 5, pp. 1915–1930, 2006.

[95] V. Montagner, V. Leite, R. Oliveira, and P. Peres, "State feedback control of switched linear systems: An lmi approach," *Journal of computational and applied mathematics*, vol. 194, no. 2, pp. 192–206, 2006.

[96] J. Klamka and M. Niezabitowski, "Controllability of switched linear dynamical systems," in *2013 18th International Conference on Methods Models in Automation Robotics (MMAR)*, 2013, pp. 464–467.

[97] Z. Sun, S. S. Ge, and T. H. Lee, "Controllability and reachability criteria for switched linear systems," *Automatica*, vol. 38, no. 5, pp. 775–786, 2002.

[98] W. Hu, Z. Ding, X. Chen, and X. Long, "Controllability analysis of flyback converter with constant power load based on switched linear systems," *Energy Reports*, vol. 8, pp. 747–754, 2022.

[99] C. Yang, L. Huang, H. Xin, and P. Ju, "Placing grid-forming converters to enhance small signal stability of pll-integrated power systems," *IEEE Transactions on Power Systems*, vol. 36, no. 4, pp. 3563–3573, 2021.

[100] L.-A. Lee, "Microgrid as a cyber-physical system: Dynamics and control," 2023.

[101] H. Cheng, Z. Shuai, C. Shen, X. Liu, Z. Li, and Z. J. Shen, "Transient angle stability of paralleled synchronous and virtual synchronous generators in islanded microgrids," *IEEE Transactions on Power Electronics*, vol. 35, no. 8, pp. 8751–8765, 2020.

[102] Z. Tian, X. Li, X. Zha, Y. Tang, P. Sun, M. Huang, and P. Yu, "Transient synchronization stability of an islanded ac microgrid considering interactions between grid-forming and grid-following converters," *IEEE Journal of Emerging and Selected Topics in Power Electronics*, vol. 11, no. 4, pp. 4463–4476, 2023.

[103] Z. Zou, J. Tang, X. Wang, Z. Wang, W. Chen, G. Buticchi, and M. Liserre, "Modeling and control of a two-bus system with grid-forming and grid-following converters," *IEEE Journal of Emerging and Selected Topics in Power Electronics*, vol. 10, no. 6, pp. 7133–7149, 2022.

[104] R. Ma, Y. Zhang, M. Zhan, K. Cao, D. Liu, K. Jiang, and S. Cheng, "Dominant transient equations of grid-following and grid-forming converters by controlling-unstable-equilibrium-point-based participation factor analysis," *IEEE Transactions on Power Systems*, 2023.

[105] S. D'Arco and J. A. Suul, "Equivalence of virtual synchronous machines and frequency-droops for converter-based microgrids," *IEEE Transactions on Smart Grid*, vol. 5, no. 1, pp. 394–395, 2014.

[106] E. A. S. Ducoin, Y. Gu, B. Chaudhuri, and T. C. Green, "Swing equation modelling of gfl inverter and comparison of its damping and inertia with gfm inverter," in *19th International Conference on AC and DC Power Transmission (ACDC 2023)*, vol. 2023, 2023, pp. 108–114.

[107] R. H. Lasseter, Z. Chen, and D. Pattabiraman, "Grid-forming inverters: A critical asset for the power grid," *IEEE Journal of Emerging and Selected Topics in Power Electronics*, vol. 8, no. 2, pp. 925–935, 2020.

[108] Z.-X. Zou, B. D. Besheli, R. Rosso, and M. Liserre, "Interactions between phase-locked loop synchronized grid converters with different bandwidths and power ratings," in *2019 IEEE Energy Conversion Congress and Exposition (ECCE)*, 2019, pp. 5430–5437.

[109] Q. Hu, L. Fu, F. Ma, and F. Ji, "Large signal synchronizing instability of pll-based vsc connected to weak ac grid," *IEEE Transactions on Power Systems*, vol. 34, no. 4, pp. 3220–3229, 2019.

[110] R. Ma, J. Li, J. Kurths, S. Cheng, and M. Zhan, "Generalized swing equation and transient synchronous stability with pll-based vsc," *IEEE Transactions on Energy Conversion*, vol. 37, no. 2, pp. 1428–1441, 2022.

[111] P. Roos, "A comparison of grid-forming and grid-following control of vscs," 2020.

[112] M. Surprenant, I. Hiskens, and G. Venkataramanan, "Phase locked loop control of inverters in a microgrid," in *2011 IEEE Energy Conversion Congress and Exposition*, 2011, pp. 667–672.

[113] P. Kundur, "Power system stability," *Power system stability and control*, vol. 10, pp. 7–1, 2007.

[114] M. Bazaraa, H. D. Sherali, and C. Shetty, *Nonlinear Programming Theory and Algorithms*. New York: Third Edition, Wiley, 2006.

[115] H. Ahmadi and J. R. Martı´, "Linear Current Flow Equations with Application to Distribution Systems Reconfiguration," *IEEE Transactions on Power Systems*, vol. 30, no. 4, pp. 2073–2080, 2015.

Appendices

Appendix A

First Appendix

A.1 Proving Convexity of the OPF Formulation Proposed in Chapter 2

Proof:

- A problem is a convex problem if the objective function and constraints are convex functions and decisions variables belong to convex sets.

- A function $f : \mathbb{R}^N \rightarrow \mathbb{R}$, of the vector of variables $(x_1, \ldots, x_N)$ is said to be convex if the following inequality holds for any two vectors $\boldsymbol{x}_1$ and $\boldsymbol{x}_2$:

$$f(\lambda \boldsymbol{x}_1 + (1-\lambda)\boldsymbol{x}_2) \leq \lambda f(\boldsymbol{x}_1) + (1-\lambda) f(\boldsymbol{x}_2), \ \forall \ \lambda \in [0,1] \tag{A.1}$$

Part 1: To show functions (2.4)-(2.8), (2.11)-(2.13) and (2.16) are convex affine functions. Taking function (2.13) as an example,

$$\text{Let, } f(\boldsymbol{v}^t) = diag(\boldsymbol{a}^t)\boldsymbol{v}^t - \boldsymbol{v}_h = \boldsymbol{A}^t\boldsymbol{v}^t - \boldsymbol{v}_h \tag{A.2}$$

The decision variable $\boldsymbol{v}^t \in \mathbb{R}^{3N+}$, where the $3N$ dimensional positive Euclidean space $\mathbb{R}^{3N+}$ is a convex set since given any two points $\boldsymbol{v}_1^t, \boldsymbol{v}_2^t \in \mathbb{R}^{3N+}$, their convex combination $\lambda\boldsymbol{v}_1^t + (1-\lambda)\boldsymbol{v}_2^t, \forall\lambda \in [0,1]$ is also in $\mathbb{R}^{3N+}$. Therefore,

$$f(\boldsymbol{v}_1^t) = \boldsymbol{A}^t\boldsymbol{v}_1^t - \boldsymbol{v}_h \tag{A.3}$$

$$f(\boldsymbol{v}_2^t) = \boldsymbol{A}^t\boldsymbol{v}_2^t - \boldsymbol{v}_h \tag{A.4}$$

Thus, for f to be convex, any convex combination $\lambda\boldsymbol{v}_1^t + (1-\lambda)\boldsymbol{v}_2^t$ of $\boldsymbol{v}_1^t, \boldsymbol{v}_2^t$ should satisfy (A.1),

$$f(\lambda\boldsymbol{v}_1^t + (1-\lambda)\boldsymbol{v}_2^t) \leq \lambda f(\boldsymbol{v}_1^t) + (1-\lambda)f(\boldsymbol{v}_2^t),\ \forall\ \lambda \in [0,1] \tag{A.5}$$

Starting from the left hand side of (A.5),

$$\begin{aligned} f(\lambda\boldsymbol{v}_1^t + (1-\lambda)\boldsymbol{v}_2^t) &= \boldsymbol{A}^t(\lambda\boldsymbol{v}_1^t + (1-\lambda)\boldsymbol{v}_2^t) - \boldsymbol{v}_h \\ &= \lambda(\boldsymbol{A}^t\boldsymbol{v}_1^t) + (1-\lambda)(\boldsymbol{A}^t\boldsymbol{v}_2^t) - \lambda\boldsymbol{v}_h - (1-\lambda)\boldsymbol{v}_h, \\ &\qquad\qquad \text{as } \lambda \text{ is scalar} \\ &= \lambda(\boldsymbol{A}^t\boldsymbol{v}_1^t - \boldsymbol{v}_h) + (1-\lambda)(\boldsymbol{A}^t\boldsymbol{v}_2^t - \boldsymbol{v}_h) \\ &= \lambda f(\boldsymbol{v}_1^t) + (1-\lambda)f(\boldsymbol{v}_2^t) \end{aligned} \tag{A.6}$$

Thus, Jensen's inequality is satisfied at equality and hence constraint (2.13) is a convex function and the decision variable $\boldsymbol{v}^t \in \mathbb{R}^{3N+}$ belongs to a convex set. The same extends to

functions (2.4)-(2.8), (2.11), (2.12) and (2.16) and their corresponding decision variables.

Part 2: To show (2.14), (2.15) are convex quadratic functions. Taking (2.14) as an example and for any $i = \{1, ..., n_G\}$,

$$h(p^t_{G,i}, q^t_{G,i}) = (p^t_{G,i})^2 + (q^t_{G,i})^2 - s^2_{G,i} \tag{A.7}$$

$p^t_{G,i}, q^t_{G,i} \in \mathbb{R}$ and thus using theorem 3.3.7 [114] which states, "Let S be a nonempty open convex set in $\mathbb{R}^N$, and let $h : S \to \mathbb{R}$ be twice differentiable on S. Then h is convex if and only if the Hessian matrix $H(\bar{\boldsymbol{x}})$ is positive semidefinite at each point $\bar{\boldsymbol{x}} \in S$," the convexity of (A.7) can be proved.

$$\nabla h(p^t_{G,i}, q^t_{G,i}) = \begin{bmatrix} 2p^t_{G,i} \\ 2q^t_{G,i} \end{bmatrix} \tag{A.8}$$

Hessian is given by,

$$\nabla^2 h(p^t_{G,i}, q^t_{G,i}) = \begin{bmatrix} 2 & 0 \\ 0 & 2 \end{bmatrix} \tag{A.9}$$

Using Lemma 3.3.11 [114] which states that, "Consider a symmetric matrix $H = \begin{bmatrix} a & b \\ b & c \end{bmatrix}$. Then H is positive semidefinite if and only if $a \geq 0, c \geq 0$, and $ac–b^2 \geq 0$, and is positive definite if and only if the foregoing inequalities are all strict," it can be seen that (A.9) is positive definite and constraint (2.14) is a convex function. The same extends to constraint (2.15).

Thus, the proposed OPF formulation is convex and local minima will also be a global minimum. To verify this proof, simulations were run using two different optimization platforms, Matlab using Yalmip and Python using PYOMO and IPOPT. Both these solvers generated the exact same optimal values for DER dispatch for about 2400 simulated time points which

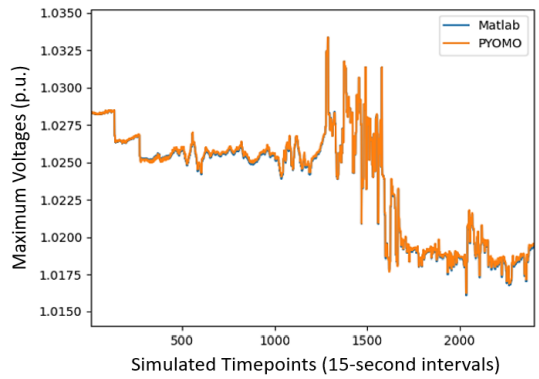

Figure A.1: Same maximum OpenDSS voltages observed using Matlab and PYOMO

resulted in the same maximum feeder voltages as shown in Fig. A.1.

A.2 Unity Correlation Coefficient and Linearity

Proof: Assuming that any two NM random variables p_i^n, p_j^n are linearly related $p_i^n = a_i p_j^n$, $a_i \in \mathbb{R}^1$, the covariance $c_{i,j}$ between them is defined as the expected value of the outer product of $(p_i^n - \mathbb{E}[p_i^n])$ and $(p_j^n - \mathbb{E}[p_j^n])$. Given the NM time series, the expected values of these two variables will be their arithmetic means, $\mathbb{E}[p_i^n] = \tilde{p}_i^n$ and $\mathbb{E}[p_j^n] = \tilde{p}_j^n$.

$$c_{i,j} = \mathbb{E}[(p_i^n - \tilde{p}_i^n)(p_j^n - \tilde{p}_j^n)] \tag{A.10}$$

$$= \mathbb{E}[p_i^n p_j^n] - \tilde{p}_j^n\,\mathbb{E}[p_i^n] - \tilde{p}_i^n\,\mathbb{E}[p_j^n] + \tilde{p}_i^n \tilde{p}_j^n \tag{A.11}$$

$$= \mathbb{E}[p_i^n p_j^n] - \tilde{p}_i^n \tilde{p}_j^n = \mathbb{E}[p_i^n p_j^n] - \mathbb{E}[p_i^n]\,\mathbb{E}[p_j^n] \tag{A.12}$$

Squaring the correlation coefficient defined in (3.22),

$$(\eta_{i,j})^2 = \frac{(c_{i,j})^2}{(s_i)^2 (s_j)^2} = \frac{(\mathbb{E}[p_i^n p_j^n] - \mathbb{E}[p_i^n]\,\mathbb{E}[p_j^n])^2}{(s_i)^2 (s_j)^2} \tag{A.13}$$

Substituting, $p_i^n = a_i p_j^n$ in the numerator,

$$(\eta_{i,j})^2 = \frac{(a_i\,\mathbb{E}[(p_j^n)^2] - a_i(\mathbb{E}[p_j^n])^2)^2}{(s_i)^2(s_j)^2} \tag{A.14}$$

The variance $(s_j)^2$ is defined as,

$$(s_j)^2 = \mathbb{E}[p_j^n - \tilde{p}_j^n]^2 = \mathbb{E}[(p_j^n)^2] - 2\tilde{p}_j^n\,\mathbb{E}[(p_j^n)] + \mathbb{E}[(\tilde{p}_j^n)^2] \tag{A.15}$$

$$= \mathbb{E}[(p_j^n)^2] - 2(\tilde{p}_j^n)^2 + (\tilde{p}_j^n)^2 = \mathbb{E}[(p_j^n)^2] - (\tilde{p}_j^n)^2 \tag{A.16}$$

$$= \mathbb{E}[(p_j^n)^2] - (\mathbb{E}[p_j^n])^2 \tag{A.17}$$

Substituting (A.17) in the numerator of (A.14),

$$(\eta_{i,j})^2 = \frac{a_i^2((s_j)^2)^2}{(s_i)^2(s_j)^2} \tag{A.18}$$

Also, the variance $(s_i)^2 = a_i^2(s_j)^2$ since $p_i^n = a_i p_j^n$, hence,

$$(\eta_{i,j})^2 = \frac{a_i^2((s_j)^2)^2}{a_i^2(s_j)^2(s_j)^2} = 1 \tag{A.19}$$

Thus, if $\eta_{i,j} = 1$, one can express $p_i^n = a_i p_j^n,\ a_i \in \mathbb{R}^1$. In practice however, $\eta_{i,j}$ will be less than 1 primarily due to the low correlation in the actual demand time series of NM loads. The solar generation profiles of NM loads in a geographically small load section with similar cloud patterns will be more correlated. This was validated by evaluating the correlation in actual demand time series of 18 residential customers from the Pecan Street database which is found to be 0.306 whereas the correlation in their solar generation time series is 0.921 [84]. The a_i factors obtained using (3.24) for all 18 customers were used to estimate their respective solar generation using $a_i p_j^g$. Fig. A.2 shows a comparison of the estimated and

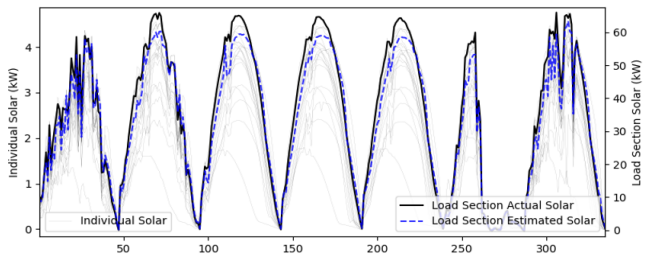

Figure A.2: Comparison of solar generation estimates obtained using proposed disaggregation based approach with actual solar generation.

actual aggregated solar generation for all 18 customers for a week. It can be seen that the proposed approach is able to accurately estimate the solar generation of all customers. This is why solar generation is expressed as a linear function of the representative solar profile in section 3.2.

A.3 Additional Constraints Used in Section 3.3

Generator Constraints: Generator injections are constrained to be within their real and reactive power and kVA limits. The real power limits can be a constant such as for a synchronous generator or be a function of time. For a PV generator these will be based on irradiance forecasts and for a battery energy storage system these are based on state of charge, minimum reserve and maximum kWh capacity limits.

$$\delta^N_{i,k}\bar{P}^{min,\theta}_{i,k} \leq P^{G,\theta}_{i,k} \leq \delta^N_{i,k}\bar{P}^{max,\theta}_{i,k} \tag{A.20}$$

$$\delta^N_{i,k}\bar{Q}^{min,\theta}_{i} \leq Q^{G,\theta}_{i,k} \leq \delta^N_{i,k}\bar{Q}^{max,\theta}_{i} \tag{A.21}$$

The real and reactive power injections must be constrained to be within the kVA limits of the generator $(Q^{G,\theta}_{i,k})^2 + (P^{G,\theta}_{i,k})^2 \leq (\bar{S}^{max,\theta}_{i})^2$. This quadratic constraint has been linearized

using a regular convex polygon approximation [115], where $\bar{S}_i^{\theta} = 1.0996\bar{S}_i^{max,\theta}$.

$$
\begin{aligned}
-\sqrt{3}(Q_{i,k}^{G,\theta} + \bar{S}_i^{\theta}) \leq P_{i,k}^{G,\theta} \leq -\sqrt{3}(Q_{i,k}^{G,\theta} - \bar{S}_i^{\theta}) \\
-\frac{\sqrt{3}}{2}\bar{S}_i^{\theta} \leq P_{i,k}^{G,\theta} \leq \frac{\sqrt{3}}{2}\bar{S}_i^{\theta} \\
\sqrt{3}(Q_{i,k}^{G,\theta} - \bar{S}_i^{\theta}) \leq P_{i,k}^{G,\theta} \leq \sqrt{3}(Q_{i,k}^{G,\theta} + \bar{S}_i^{\theta})
\end{aligned} \tag{A.22}
$$

Nodal voltage and line loading constraints: The voltages are constrained to be within an upper and lower bound.

$$\delta_{i,k}^{N}\bar{V}^{l} \leq V_{i,k}^{\theta} \leq \delta_{i,k}^{N}\bar{V}^{u} \tag{A.23}$$

The real and reactive power flows through the edges are also constrained to be within their kVA ratings.

$$-\delta_{ij,k}^{E}\bar{S}_{ij}^{max,\theta} \leq P_{ij,k}^{\theta} \leq \delta_{ij,k}^{E}\bar{S}_{ij}^{max,\theta} \tag{A.24}$$

$$-\delta_{ij,k}^{E}\bar{S}_{ij}^{max,\theta} \leq Q_{ij,k}^{\theta} \leq \delta_{ij,k}^{E}\bar{S}_{ij}^{max,\theta} \tag{A.25}$$

$$
\begin{aligned}
-\sqrt{3}(Q_{ij,k}^{\theta} + \bar{S}_{ij}^{\theta}) \leq P_{ij,k}^{\theta} \leq -\sqrt{3}(Q_{ij,k}^{\theta} - \bar{S}_{ij}^{\theta}) \\
-\frac{\sqrt{3}}{2}\bar{S}_{ij}^{\theta} \leq P_{ij,k}^{\theta} \leq \frac{\sqrt{3}}{2}\bar{S}_{ij}^{\theta} \\
\sqrt{3}(Q_{ij,k}^{\theta} - \bar{S}_{ij}^{\theta}) \leq P_{ij,k}^{\theta} \leq \sqrt{3}(Q_{ij,k}^{\theta} + \bar{S}_{ij}^{\theta})
\end{aligned} \tag{A.26}
$$

where $\bar{S}_{ij}^{\theta} = 1.0996\bar{S}_{ij}^{max,\theta}$.

Connectivity and Sequencing Constraints: All the larger black start capable DERs are started from the beginning to reduce the overall restoration time. The state of all remotely operable switches $\mathcal{E}_O$ is set to zero, $\delta_{ij,1}^{E} = 0,\ \forall ij \in \mathcal{E}_O$. Energization of remotely operable switches ensures energization of both of their end nodes, while all other edges are energized

as soon as either one of their end nodes becomes energized.

$$\delta^E_{ij,k} \leq \delta^N_{i,k},\ \delta^E_{ij,k} \leq \delta^N_{j,k},\ \forall ij \in \mathcal{E}_O \tag{A.27}$$

$$\delta^E_{ij,k} = \delta^N_{i,k},\ \delta^E_{ij,k} = \delta^N_{j,k},\ \forall ij \in \mathcal{E} \backslash \mathcal{E}_O \tag{A.28}$$

All edges and nodes are not connected by remotely operable switches. Thus, to reduce system complexity, all buses and edges between two remotely operable switches can be grouped into a 'load section' [83],[85]. Let $\mathcal{S}$ be the set of all load sections and $\mathcal{E}_O$ be the set of remotely operable switches between these load sections. Let $\delta^S_{s,k},\ s \in \mathcal{S}$ represent the energization status of each load section. Thus, if a load section is energized then all nodes within it are also energized.

$$\delta^N_{i,k} = \delta^S_{s,k},\ s \in \mathcal{S} \tag{A.29}$$

To ensure radial operation, a switch is not allowed to close if the load sections on both ends are already energized at the previous time step (A.30). Similarly, a de-energized load section is only allowed to be energized by at most one switch (A.31) to avoid forming loops [85].

$$\delta^E_{ab,k} - \delta^E_{ab,k-1} \leq (\delta^S_{a,k} - \delta^S_{a,k-1}) + (\delta^S_{b,k} - \delta^S_{b,k-1}) \qquad \forall a, b \in \mathcal{S},\ k > 1 \tag{A.30}$$

$$\sum_{i:i \leftrightarrow s} (\delta^E_{is,k} - \delta^E_{is,k-1}) \leq 1 + M\delta^S_{s,k-1},\quad k > 1.\quad s \in \mathcal{S} \tag{A.31}$$

To ensure that a feasible switching sequence is obtained, constraint (A.32) ensures that a load section can only be energized by a closed switch and constraint (A.33) ensures that a

switch can only be closed when at least one of its end load sections were previously energized.

$$\delta^S_{s,k} \leq \sum_{i:i\leftrightarrow s} \delta^E_{is,k},\ \forall s \in \mathcal{S} \tag{A.32}$$

$$\delta^E_{ab,k} \leq \delta^S_{a,k-1} + \delta^S_{b,k-1},\ \forall a,b \in \mathcal{S},\ k > 1 \tag{A.33}$$

NO tie switches are present in microgrid for enhanced resilience. These may however form cycles, disrupting the desired radial operation of the microgrid and leading to circulating currents. This is avoided by adding constraint (A.34) for each simple cycle c formed from the cycle basis $\mathcal{C}_\mathcal{B}$ of the reduced network of load sections.

$$\sum_{ij\in c} \delta^E_{ij,k} \leq N_s(c) - 1,\ \forall k \in \mathcal{K},\ \forall c \in \mathcal{C}_\mathcal{B} \tag{A.34}$$

where $N_s(c)$ is the total number of edges in $c \in \mathcal{C}_\mathcal{B}$.

A.4 IEEE Article Reuse Policy

As per IEEE guidelines available at $https://journals.ieeeauthorcenter.ieee.org/choose-a-publishing-agreement/avoid-infringement-upon-ieee-copyright/$ (at the time of submission of this dissertation), when full text article is used, the following should be included in the references: "© 20XX IEEE. Reprinted, with permission, from [full citation of original published article]." To comply with it full citations are added as footnotes at the beginning of chapters 2 and 3 and I am the main author of both of those papers. When posting the thesis on university website, the following message must be included:

"In reference to IEEE copyrighted material which is used with permission in this thesis, the IEEE does not endorse any of Virginia Tech's products or services. Internal or personal use of

this material is permitted. If interested in reprinting/republishing IEEE copyrighted material for advertising or promotional purposes or for creating new collective works for resale or redistribution, please go to *http://www.ieee.org/publications_standards/publications/rights/rights_link.html* to learn how to obtain a License from RightsLink. If applicable, University Microfilms and/or ProQuest Library, or the Archives of Canada may supply single copies of the dissertation."